Geochemistry, Stable Isotopes and Fluid Inclusion Studies of the Otjikoto Gold Deposit, Central Namibia

By

Lisias Negonga

Dissertation submitted for the degree of Master of Science in Geology

Department of Geological Science

University of Cape Town

South Africa

February 2018

Supervised by Dr. Lynnette Greyling and Prof. Chris Harris

Plagiarism Declaration

I know that plagiarism is wrong. Plagiarism is to use another's work and pretend that it is one's own.

I have used the Havard convention for citation and referencing. Each contribution to, and quotation in, this thesis from the work(s) of other people has been attributed, and has been cited and referenced.

This thesis is my own work.

I have not allowed, and will not allow, anyone to copy my work with the intention of passing it off as his or her own work.

Acknowledgement

I would like to sincerely express my heartfelt gratitude to my supervisors, Prof. Chris Harris and Dr Lynnette Greyling, for making this project possible. To Prof. Chris Harris, thank you for believing in my abilities, for guiding me to completion and for the great supervision. To Dr Lynnette Greyling, thank you for assisting with the fluid inclusion experiment, the tireless editing and for making this project possible. Thank you both for helping me to grow in maturity, strength and character. I would also humbly like to thank Prof. Steve Richardson for his support and guidance.

I would greatly like to thank Nicholas, David, Jonathan, Rene and Dr. Phil for their assistance with the analytical work. I would also like to thank Riana, and the rest of the CAF team from the University of Stellenbosch, for assisting with the ICP-MS results.

My sincere appreciation goes to Bruce Fletcher, Steve Robinson and the rest of B2 Gold Namibia's team for providing access to the mine, availing literature and for their great support during this project.

I would greatly like to thank my parents, family and friends for providing the emotional support I needed throughout this project. I especially want to thank Josia, Dixon, Diecu and Jason for their great input.

I would like to thank Namibia Student Financial Assistance Fund (NSFAF) and the Julian Baring Scholarship fund for co-funding this project. The Society of Economic Geologists (SEG) is greatly thanked for the research grant.

I thank the Almighty God for the endless blessings, for giving me strength and for guiding me throughout this journey.

Abstract

The Otjikoto gold deposit is located within the Damara Orogenic Belt which is part of the system of Pan-African mobile belts. The Damara Belt is a northwest trending orogenic belt which formed through sequences of spreading, rifting, subduction and from continental collision between the Congo, Kalahari and Rio Delta Plata Cratons between 900 Ma and 450 Ma. Mineralisation at Otjikoto is hosted by a group of metamorphic rocks which consist of biotite schists from the Okonguarri Formation, albitites from the Oberwasser member and marble units from the Okawayo member. The gold mineralization occurs in a sheeted vein network system with veins which are positioned parallel towards the foliation of the albitites and hornfels of the Oberwasser Member. The vein types include both quartz and carbonate hosted vein types. The vein mineralogy includes magnetite, pyrite and pyrrhotite which are associated with amphibole, quartz, almandine garnets, and free gold. A fluid inclusion study carried out on the vein quartz showed the co-existence of the aqueous, carbonic and aqueous-carbonic fluid inclusions within the Okonguarri Formation. The aqueous inclusions have moderate to high salinities with salinities ranging from 30.0 to 44.5 wt. % NaCl eq. in aqueous inclusions with halite crystals and from 0.9 to 22.9 wt. % NaCl eq. in inclusions without halite crystals. The total homogenisation temperatures, Th tot (L), ranged from 151 to 488 °C in the aqueous-carbonic inclusions and from 156 to 444 °C in the aqueous inclusions. The melting temperature of CO_2 ($TmCO_2$) ranged from -60.3 to -57.5 °C in carbonic inclusions and from -60.2 to -57.2 °C in aqueous-carbonic inclusions. It is proposed that the aqueous and carbonic inclusions (CO_2-CH_4) from the Okonguarri Formation are the end members of fluid immiscibility. The presence of CO_2 and CH_4 is indicated by the low $TmCO_2$ values and may be justified by the decomposition of the carbonaceous metasediments which are found in the stratigraphy at Otjikoto. The $\delta^{18}O$ values range from of 8.35 ‰ to 8.75 ‰ for the magnetite and 17.51 ‰ to 18.47 ‰ for the vein quartz samples. Analysis of the microprobe data on the amphiboles shows that the analysed grains are made up of anthophyllites. Microprobe data of the chlorites showed that the majority of the chlorites are made up of ripidolites. Temperatures of chlorite formation were calculated to be in the range of 221°C to 358 °C by using chlorite geothermometric equations. Major element variation diagrams show a strong negative correlation of TiO_2, Al_2O_3, MgO, Na_2O and FeOt vs SiO_2. Variation diagrams were also plotted for the trace elements vs Zr. The Sr, Y, La and Ce vs Zr plots show a strong positive correlation.

Table of Contents

List of Figures

List of Tables

1 Introduction

1.1 Locality

The study area is located in Central Namibia, at the Otjikoto Gold Mine. The deposit is located approximately 310 km from Windhoek (17°6'0.67"E, 19°58'35.13"S), between the towns of Otavi and Otjiwarongo in Namibia (Figure 1-1). The Otjikoto gold deposit is located within the Damara Orogenic Belt which is part of the Pan-African mobile belt systems (Kisters, 2008).

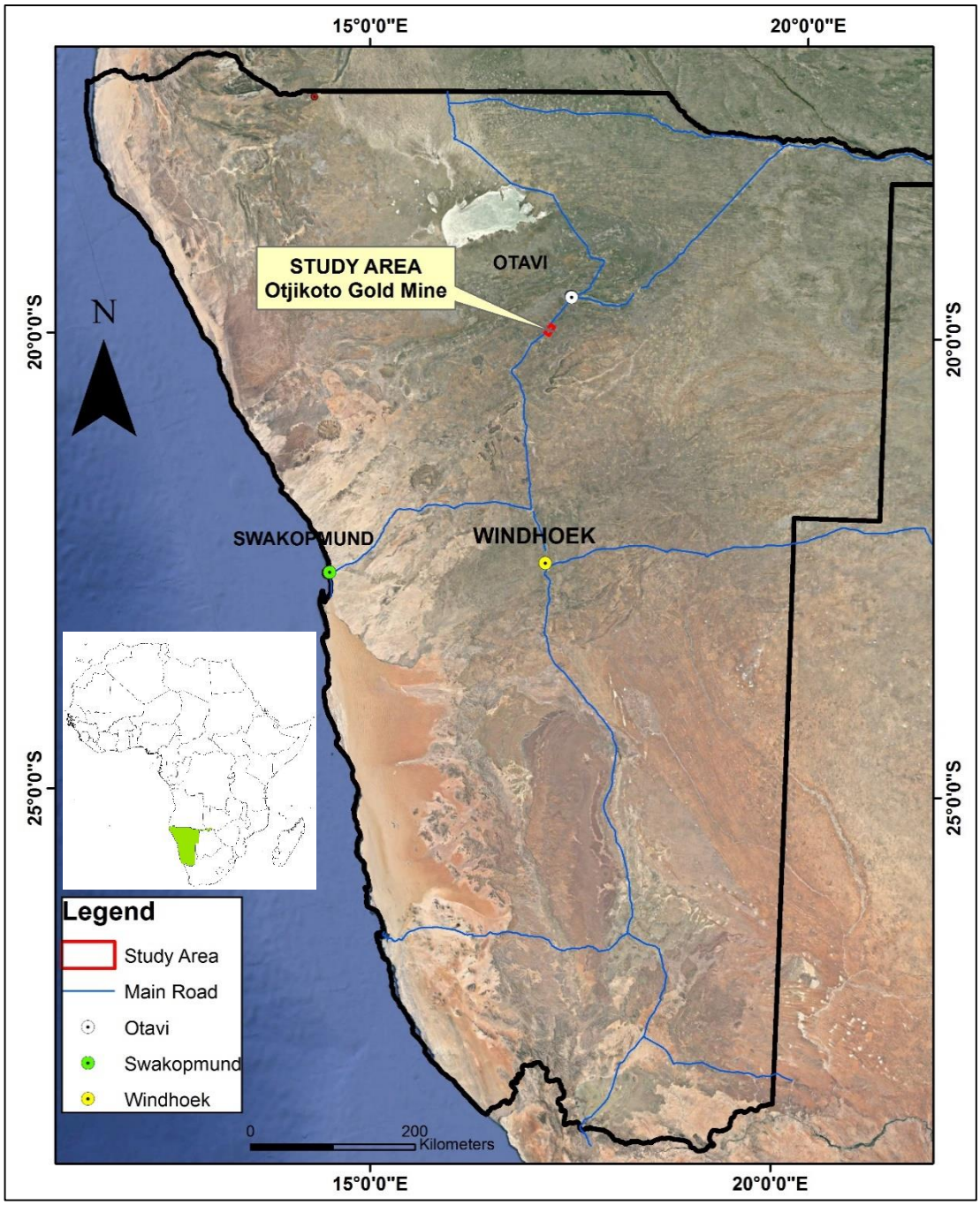

Figure 1-1 Google earth image of Namibia showing the locality of the Otjikoto Gold Mine in relation to Windhoek. The red square denotes the location of the study area.

Gold mineralisation at the Otjikoto Deposit is found within sheeted veins which are hosted by albitites, hornfels, marbles and biotite schists of the Okonguarri Formation. The vein types include both quartz and carbonate hosted vein types. The veins contain pyrrhotite, pyrite and chalcopyrite (McDonald et al., 2011).

1.2 Aims of the Study

The development of the Otjikoto Gold Deposit is important for the Namibian mining industry as well as the country's economy. This is because the mining industry is one of Namibia's main contributor to employment and one of the biggest contributors to the country's gross domestic product (GDP) (Dladla, 2015). The Otjikoto gold mine has a current reserve of 25.9 Mt (1.28 g/t Au), with an indicated resource of 33 Mt (1.37 g/t Au) and a lifespan of 10 years (Johnson & MacLean, 2016). There has been limited academic research done on the Otjikoto gold deposit.

This study therefore aims to understand the geochemistry of the host rocks, the nature of the trace elements, and the petrographic relationships of the host rocks. The study further aims to gain an understanding of the gold mineralising fluids at Otjikoto and using stable isotopes to understand the sources of these fluids. The study also aims to gain a better understanding into the tectonic setting and mineralization model of Otjikoto. This may in-turn contribute to the limited academic literature available and therefore contribute to the context of economic geology as a whole.

1.3 Project Objectives

The main objective of this research project is to undertake a detailed study on the geochemistry, petrography, fluid inclusions and stable isotopes of the rock samples collected from Otjikoto. The objectives of the research project were:

- To determine the tectonic setting of Otjikoto by interpreting the major and trace element data.
- To determine the temperature of ore formation by interpreting the temperature of chlorite formation.
- To determine the types of fluids related to gold mineralisation at Otjikoto.
- To estimate the temperature and pressure at which the mineralising fluids were trapped.
- To determine the petrographic relationships and mineral paragenesis at Otjikoto.
- To determine the temperature of ore formation by interpreting oxygen isotope fractionation data of quartz and magnetite grains.

1.4 Orogenic Gold Overview

Orogenic gold deposits are important exploration targets in mobile orogenic belts. Orogenic gold deposits are found in metamorphic complexes of various ages and display different episodes of deformation (Goldfarb et al., 2000). These deposits are also referred to as metamorphic gold, structurally-controlled deposits, lode gold deposit, mesothermal gold deposits and shear-zone hosted gold (Groves et al., 1998). Orogenic gold deposits all have similar characteristics such as being hosted by altered and metamorphosed rocks, exhibiting a complex geological evolution and being extensively deformed (Goldfarb et al., 2000). Orogenic deposits are commonly found in close proximity to crustal deformation zones and have undergone brittle-ductile deformation (Goldfarb et al., 2000). Geological structures displayed in these deposits provide evidence of localised extensions. Hodgson (1989) and Robert (1996) have characterised the strong structural control of these deposits and their ore bodies. The common structural features associated with orogenic gold deposits are fold hinges, brittle faults, ductile shear zones and extensional fractures (Hodgson, 1989). The deposits are commonly hosted by altered rocks with quartz veins and/or disseminated mineralization (Goldfarb et al., 2000). Orogenic deposits usually have a long vertical extent (> 1 km) with some, such as India's Kolar gold field, exceeding 3 km (Groves et al., 1998). Veining is dominated by quartz with carbonate and sulphide minerals. Chlorite, mica, scheelite, albite and tourmaline may also be found in the veins, although they are less common. Gold, which is found within the veins and wall rock, is commonly associated with pyrite, chalcopyrite, pyrrhotite, sphalerite, galena and arsenopyrite (Groves et al., 1998).

1.4.1 Overview of Albitite Host Rocks

Although albitites are uncommon rock types associated with metasomatism, they do occur in various localities around the world. Albitites are more commonly associated with plutonic rocks and less commonly associated with low-grade metamorphism (Bodart, 1966). The albitite nomenclature was described by Brögger (1875) as a rock that contains a major percentage of the albite mineral. Not all albitites are majority made up of albite (Bodart, 1966). In some instances, the feldspar contained in the albitite is oligoclase instead of albite (Bodart, 1966). Albitites exhibit a well-developed granular texture and a homogeneous composition of albite (Bamba et al., 1996). Albitites act as a carrier for H_2O, CO_2, As, S and Au bearing-fluids due to their brittleness and relatively high viscosity (Bamba et al., 1996). Albitites are a less common type of host rock for gold mineralisation. Albitite-hosted ore bodies can extend to

over hundreds of metres in length (Bamba et al., 1996). An example of a large albitite-hosted gold deposit is the Loraboué deposit in Burkina Faso, which has a width of 1.8km and a length of 8km, with a thickness of about 300m (Bamba et al., 1996). Quartz veining is commonly observed in albitite hosted gold deposits. Most albitite-hosted gold deposits contain disseminated mineralisation associated with quartz veins (Bamba et al., 1996). In addition to albite and quartz, albitite rocks also contain rutile, chlorite, zircon and apatite (Bamba et al., 1996). In some orogenic gold deposits, albitites have exhibited well-developed alteration halos in the veins (Bamba et al., 1996). These alteration halos may range from a few cm to tens of centimetres in thickness (Bamba et al., 1996). When albitites are found within mafic-intermediate series, the composition of the carbonate will be mostly ankeritic (Bamba et al., 1996). When albitites are found within felsic meta-sedimentary series, the carbonate composition will be pure calcite (Bamba et al., 1996). No obvious cleavage is visible in albitites. Albitite rock units usually have a high Al_2O_3 and Na_2O content and are low in K_2O, Fe_2O_3, Ba and Rb (Palomba, 2001). The interpretation for this enrichment and depletion is that K-Feldspar, biotite and plagioclase underwent a chemical to structural change during recrystallization and dissolution (Palomba, 2001). Some albitites (e.g. from Central Sardinia) show a redistribution of elements caused by the mobilization of rare earth elements during the time of formation (Palomba, 2001). Macroscopic characteristics of albitites differ from one area to another (Palomba, 2001). Magmatic textures are not visible in albitites (Palomba, 2001). The most common colour of albitites is white while some units have a yellow-greenish colour when chlorite is concentrated within the rock unit (Palomba, 2001).

1.5 Discovery and Development of the Otjikoto Deposit

The Otjikoto deposit was discovered in 1999 by Avdale Namibia after drilling on magnetic anomalies from Otjikoto's grid (Fletcher et al., 2013). Avdale carried out a follow up drilling program in 2001 to examine the oxidised mineralization of the amphibole hornfels-albitite zone (Fletcher et al., 2013). In 2003, African Rainbow Minerals (ARM) acquired Avdale and carried out another drilling program with the intention of defining a resource for the Otjikoto Deposit (Fletcher et al., 2013). In 2004, ARM defined an inferred mineral resource of 26 million tons at a grade of 1.06 g/t gold, equivalent to 872 000 ounces gold, for the Otjikoto project (Van der Merwe et al., 2005).

In 2005, ARM transferred the project to Teal (Fletcher et al., 2013). Teal carried out further work which upgraded the resource at Otjikoto to 28.420 million tonnes at a grade 1.34 g/t gold (1.2 million ounces gold) (Wanless et al., 2009). In 2010, Teal transferred the Otjikoto gold

project to a company called Tova, which later formed Auryx Gold and became part of B2Gold Corp (Fletcher et al., 2013). B2 Gold Corp developed the Otjikoto gold project and opened the mine in 2014 (Fletcher et al., 2013). During the year 2015, the gold mine produced 145,723 ounces of gold (Johnson & MacLean, 2016). The current reserve of the mine is 25.9 Mt (1.28 g/t Au), with an indicated resource of 33 Mt (1.37 g/t Au) and a lifespan of 10 years (Johnson & MacLean, 2016).

1.6 Previous Work

Stable oxygen and hydrogen values from a previous study show that metamorphic fluids are implicated during gold mineralization with no magmatic input (Curtis, 2006). The $\delta^{18}O$ values (whole rock) for the lithologies at Otjikoto were in the range of 16.9 ‰ to 25.0 ‰. The oxygen isotope values of the quartz vein were found to be greater than those of the whole rocks (Curtis, 2006).

Previous fluid inclusion studies were conducted by Scheepers (2000). Four different types of fluid inclusions were identified, namely 1) H_2O + salt, 2) H_2O + CO_2, H_2O + CO_2 + NaCl and 3) CO_2 + CH_4 + N_2 inclusions. The final melting temperatures of CO_2 rich inclusions in the main ore zone were found to be between -61°C to -62.5°C. The total homogenisation temperatures of fluids within the main ore zone were found to be between 270 °C and 425 °C (Scheepers, 2000). Trace element analysis of samples from Otjikoto by Scheepers (2000) showed that the elements Ba and Rb are enriched within the quartzofeldspathite and peraluminius intermediate gneiss and depleted in the alkali-quartzofeldspathite rocks (Scheepers, 2000).

Probework conducted on amphibole and garnet minerals showed that the garnets from Otjikoto are primarily almandine rich with minor occurrences of grossular, pyrope and spessertine garnets (Scheepers, 2000). The results on the garnet probe also showed that the garnets found below the marble unit are mainly the grossular type (Scheepers, 2000). A classification based on recalculated microprobe values showed that the calcium rich amphiboles are made up of tschermakite and magnesio-hornblende (Scheepers, 2000). The iron-magnesium rich amphiboles consist of anthophyllite and cummingtonite-granerite type of amphiboles (Scheepers, 2000). The microprobe results also showed that the carbonate grains within the samples predominantly consist of ferroan dolomite ($Ca_3Fe_2Mg_2[CO_3]_7$) (Scheepers, 2000).

2 Literature Review

2.1 Regional Geology of the Damara Orogen

The Neoproterozoic Damara Orogen extends into Central Namibia, Botswana and northwards into Angola and the DRC (Miller, 1983; Miller, 2008; Ashworth, 2014). The Damara Orogen contains two branches, namely the Damara Belt (Inland Branch) and the Kaoko Belt (Coastal Branch) (Miller, 1983; Miller, 2008; Longridge, 2012). The position of the Damara Belt is shown in figure 2-1 below. The Kaoko Belt is correlated with the Gariep Orogen and trends towards the northwest into Angola and DRC where it is referred to as the West Congo Orogen (Alkmim et al., 2006; Longridge, 2012).

The Damara Belt (Inland Branch) is the northeast trending orogenic belt which formed from the collision of the Congo Craton and Kalahari Craton (Miller, 2008; Longridge, 2012). The Damara Belt meets with the Gariep Belt and Kaoko Belt at a triple junction which is centered close to Swakopmund (Miller, 2008; Ashworth, 2014). The Damara Belt continues to strike into the DRC and Zambia where it is referred to as the Zambezi Belt (Longridge, 2012). The Damara Belt formed through sequences of spreading, rifting, subduction and continental collision between the Congo, Kalahari and Rio Delta Plata Cratons between 900 Ma and 450 Ma (Miller, 1983; Miller, 2008; Ashworth, 2014).

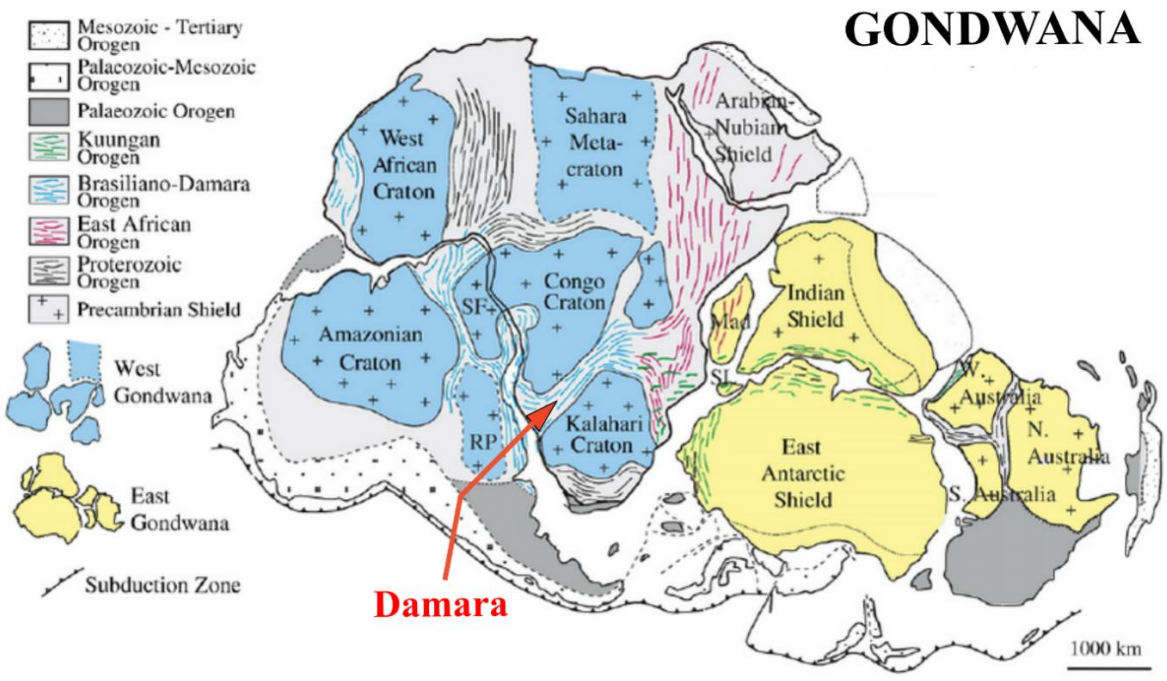

Figure 2-1 Map displaying the reconstruction of Gondwana. The various cratons are separated by the Neoproterozoic and younger orogenic belts. The position of the Damara Belt is shown by the red arrow (modified after Gray et al., 2008; Rankin, 2015).

The Damara Belt has been subdivided into tectonostratigraphic zones according to the metamorphic grades, magmatic histories, large-scale lineaments, and facies, structural and lithological variations (Miller, 1983; Miller, 2008; Ashworth, 2014). The Belt has an orogenic core with voluminous granitoids and high-grade metamorphic rocks (Miller, 1983; Miller, 2008; Longridge, 2012). The tectono-stratigraphic zones, as shown in Figure 2-2, arranged from South to North, are the Southern Platform (SP), Southern Margin Zone (SMZ), Southern Zone (SZ), Central Zone (CZ is subdivided into southern central zone (sCZ) and northern central zone (nCZ)), Northern Zone (NZ), Northern Margin Zone (NMZ) and Northern Platform (NP) (Miller, 1983; Hoffmann, 1987; Miller, 2008; Ashworth, 2014).

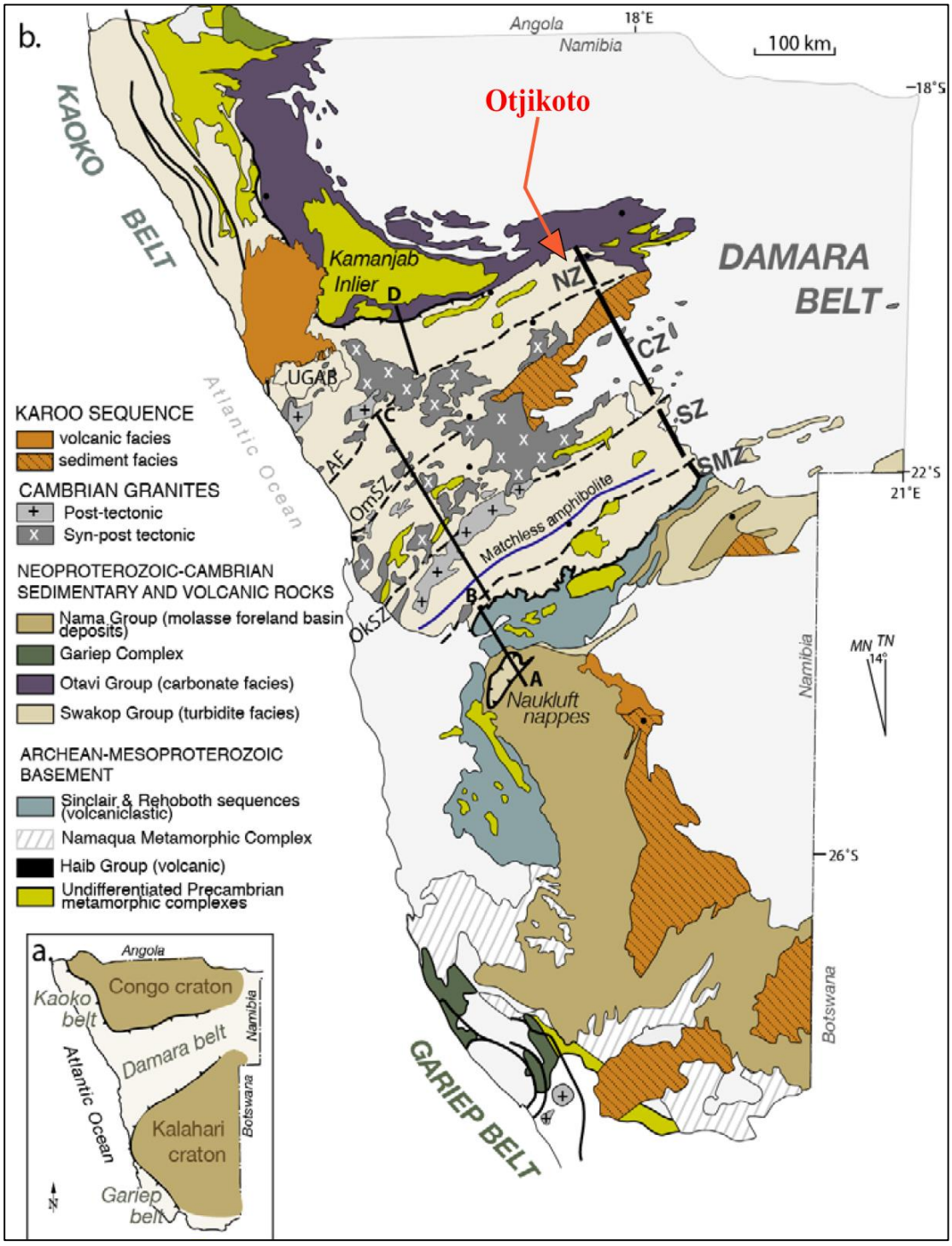

Figure 2-2 Tectonostratigraphic map of the Damara Orogen showing the distribution of the Swakop Group turbidites and plutonic rocks. The position of the Otjikoto Deposit is indicated by the red arrow. Inset (a) displays the relative position of the Damara Belt, in relation to the Congo and Kalahari cratons. **OkSZ**, Okahandja Shear Zone; **OmSZ**, Omaruru Shear Zone; **AF**, Autseib Fault; **SMZ**, Southern Margin Zone; **SZ**, Southern Zone; **CZ**, Central Zone; **NZ**, Northern Zone (Modified after Gray et al., 2008; Foster et al., 2013).

Depositional history of the Damara Orogen

The Damara Belt contains metasedimentary rocks of the Damara Supergroup which were unconformably deposited on the Pre-Damaran Abbabis Metamorphic Complex (Miller, 2008; Ashworth, 2014; Rankin, 2015). These metasedimentary rocks are subdivided into 7 major units which represent passive margins, continental rifting, shelf environments and deep water

(Gray et al., 2008; Rankin, 2015). The stratigraphy of the Damara Supergroup is illustrated in Figure 2-3 below and is correlated with the tectonostratigraphic zones.

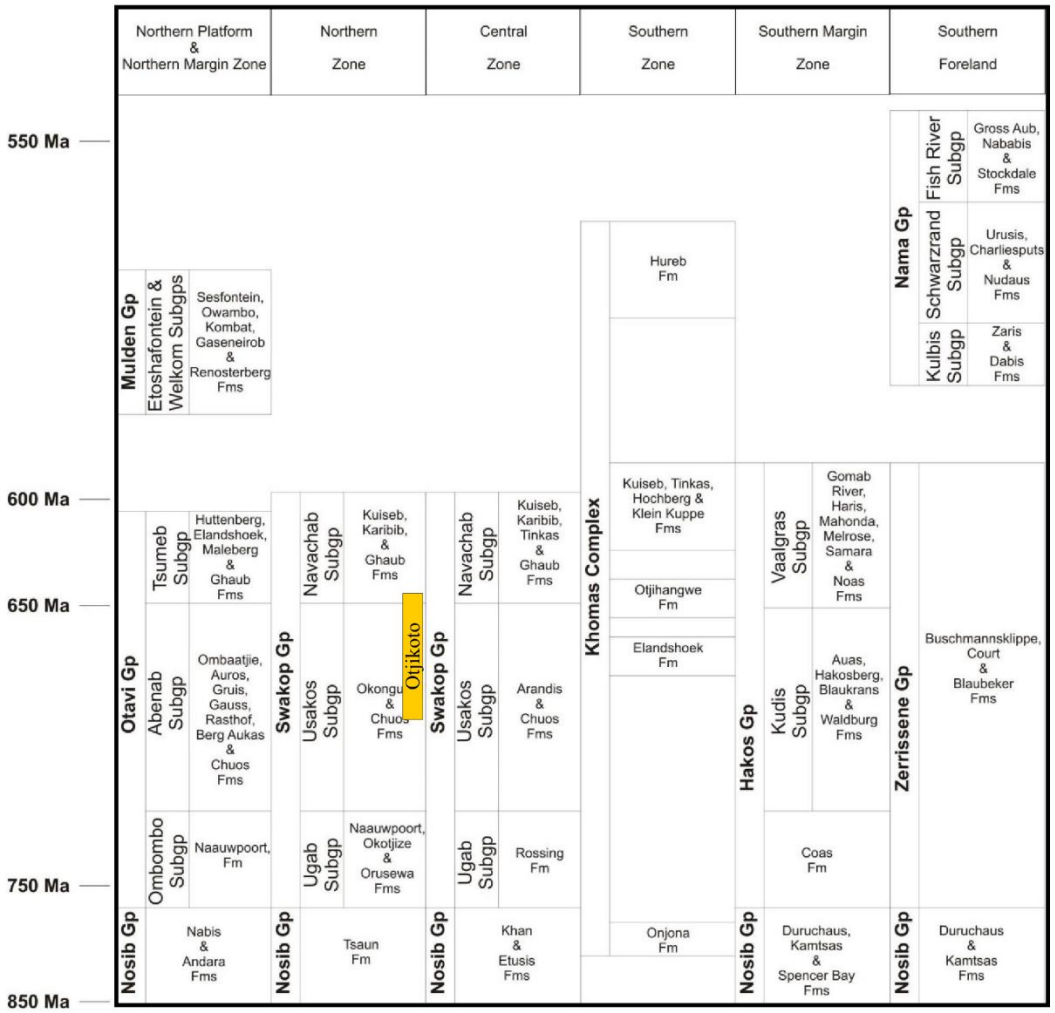

Figure 2-3 Stratigraphic and lithostratigraphic columns of the Damara Belt. The approximate age of the groups and formations are between 550Ma and 850Ma. The tectonostratigraphic zones are shown at the top. Thicknesses are not to scale. The relative age of the Nama and Mulden groups correspond to the initiation of the collision between the Congo and Kalahari Craton. (Modified after De Kock, 2001; Miller, 2008; Rankin, 2015).

The break-up of the Rodinia Supercontinent and the opening of Adamaster Ocean (800-900 Ma) led to sedimentation (Gray et al., 2008; Miller, 2008; Ashwurth, 2014). The sediments were deposited into two parallel northeast-trending grabens, the northern graben (failed rift) and the southern graben (merged with Khomas Ocean) (Frimmel et al., 2011).

The Nosib Group forms the basal unit and is comprised of quartzites, conglomerates and metagreywackes. Deposition of the Nosib Group was followed by the Otavi (carbonates), Swakop (carbonates and siliciclastics), Hakos (siliciclastics) and Witvlei (siliciclastics and carbonates) Groups (Gray et al., 2008; Frimmel et al., 2011; Rankin, 2015). Diamictites, combined with quartzites and iron formations, were preserved (Hoffman et al., 1996; Miller, 2008; Rankin, 2015). The glaciomarine rocks are characteristic of the Neoproterozoic

“Snowball Earth” event which took place in between 760 Ma -710 Ma (Hoffmann & Prave, 1996).

At 630 Ma, a second major glaciation occurred whereby post-glacial cap carbonates and shelf carbonates were deposited over a 100 Ma period (Frimmel et al., 2011; Rankin, 2015). This led to a significant drop in seal level and subsequent deposition of the Ghaub (diamictites) and Noas formations (Miller, 1983; Miller, 2008). Large-scale subsidence between the Southern Zone and Northern Zone subsequently took place and led to the accumulation of thick turbiditic greywackes (Kuiseb Formation) (Miller, 2008).

Extensive deepening and continental rupturing in the northern graben (Outjo Sea) took place, although limited evidence supports this (Frimmel et al., 2011). Minor evidence of these processes is observed in the southern graben (Khomas Sea) rocks which contains the 350 km Beshi-type Matchless Amphibolite copper belt (Killick, 2000; Miller, 2008; Ashworth, 2014). The mid-ocean ridge was covered by greywackes of the Kuiseb Formation (Killick, 2000). The presence of pyrite deposits and pillow lavas in the matchless belt shows that volcanogenic massive sulphide deposit formation took place (Killick, 2000; Miller, 2008).

Between 580 Ma and 545 Ma, subduction of the Kalahari Craton beneath the Congo Craton took place as a result of plate motion as shown in Figure 2-4 (Image C) (Miller, 2008; Frimmel et al., 2011). Uplift and erosion of the continental margin led to the formation of molasse successions (greywackes, shales, carbonates and sandstones) of the Mulden and Nama groups which were subsequently deposited into the Khomas Sea (Miller, 2008; Frimmel et al., 2011).

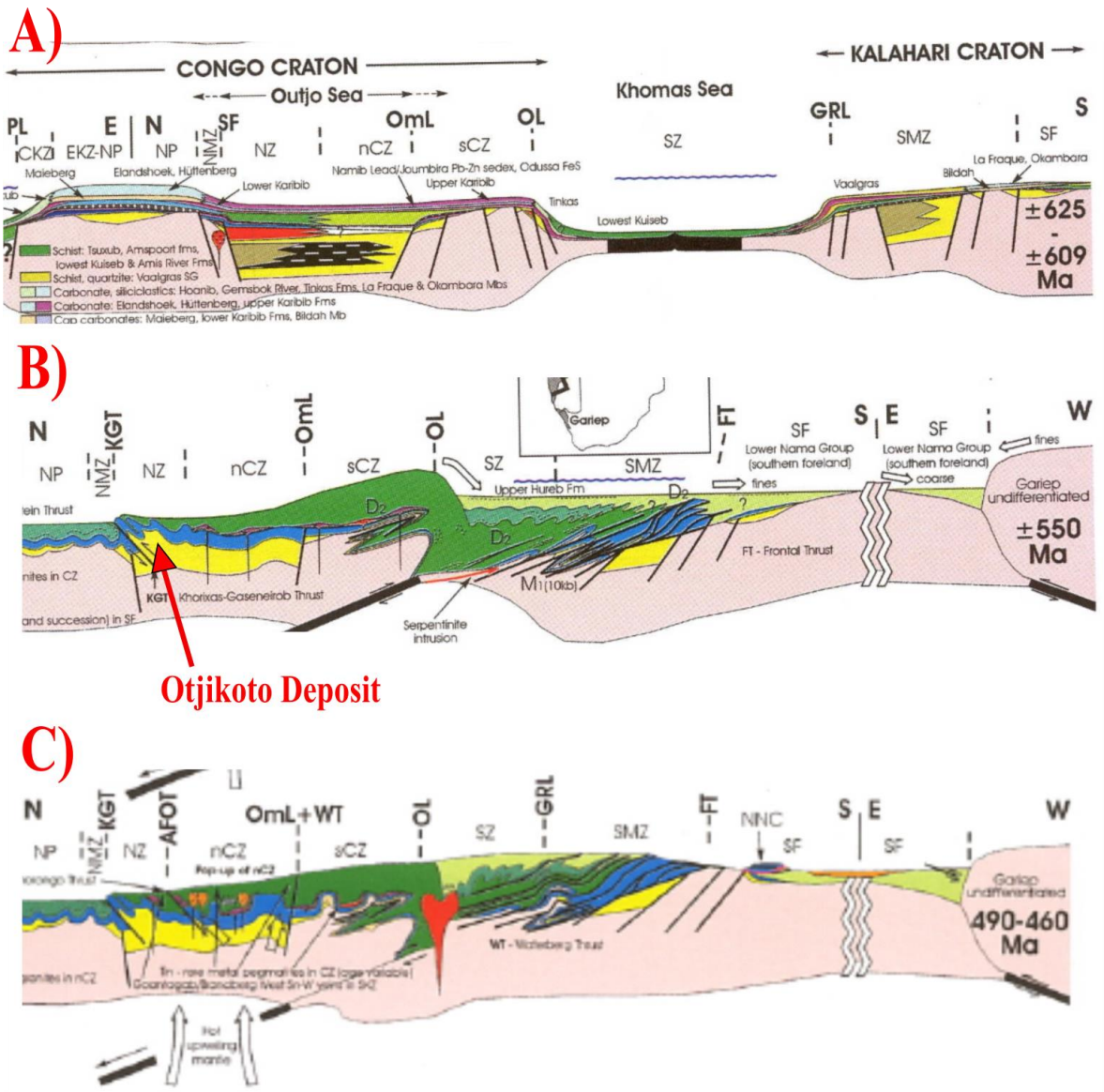

Figure 2-4 Models that show the evolution of the Damara Orogen. A) Shows the arrangement of diverging plate boundaries with continental rupture and formation of the oceanic crust (625-609 Ma). B) Shows the converging plate boundaries which led to thrusting, subduction and an increase in the metamorphic grade (550 Ma). C) Shows that further collision led to the generation and intrusion of magma. This also led to a further increase in metamorphic grade. The position of the Otjikoto deposit is shown. (Modified after Miller, 2008; Petzel, 2010).

2.2 Local Geology

The project area is mostly covered by hardpan calcrete. The geology the Otjikoto host rocks was unknown until recent years when extensive exploration was carried out by TEAL (McDonald et al., 2011). With minor occurrences of outcrops in the study area, the local geology has been interpreted by using a combination of geophysical interpretations, photo geological studies and borehole data (McDonald et al., 2011). Mineralisation at Otjikoto is hosted by a group of metamorphic rocks which consist of biotite schists from the Okonguarri Formation, albitites from the Oberwasser member and marble units from the Okawayo member (Wanless et al., 2010). A stratigraphic column and a geological map of the area are shown in Figure 2-6 and Figure 2-6 below.

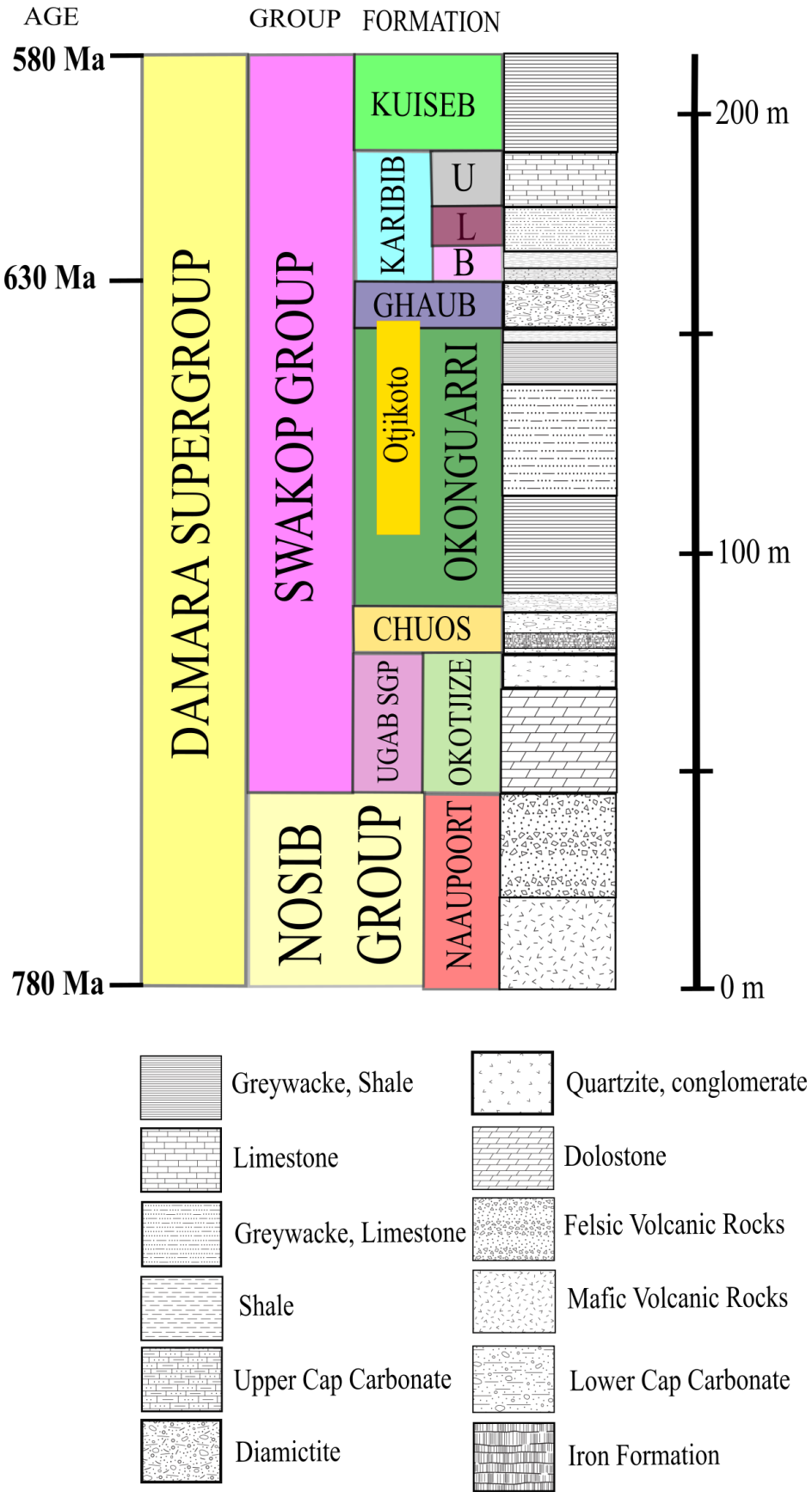

Figure 2-5 Stratigraphic column representing the position of the Otjikoto deposit, relative to the Northern Damaran Sequence after Lytle et al., (2012) and Hoffmann et al., (2004)

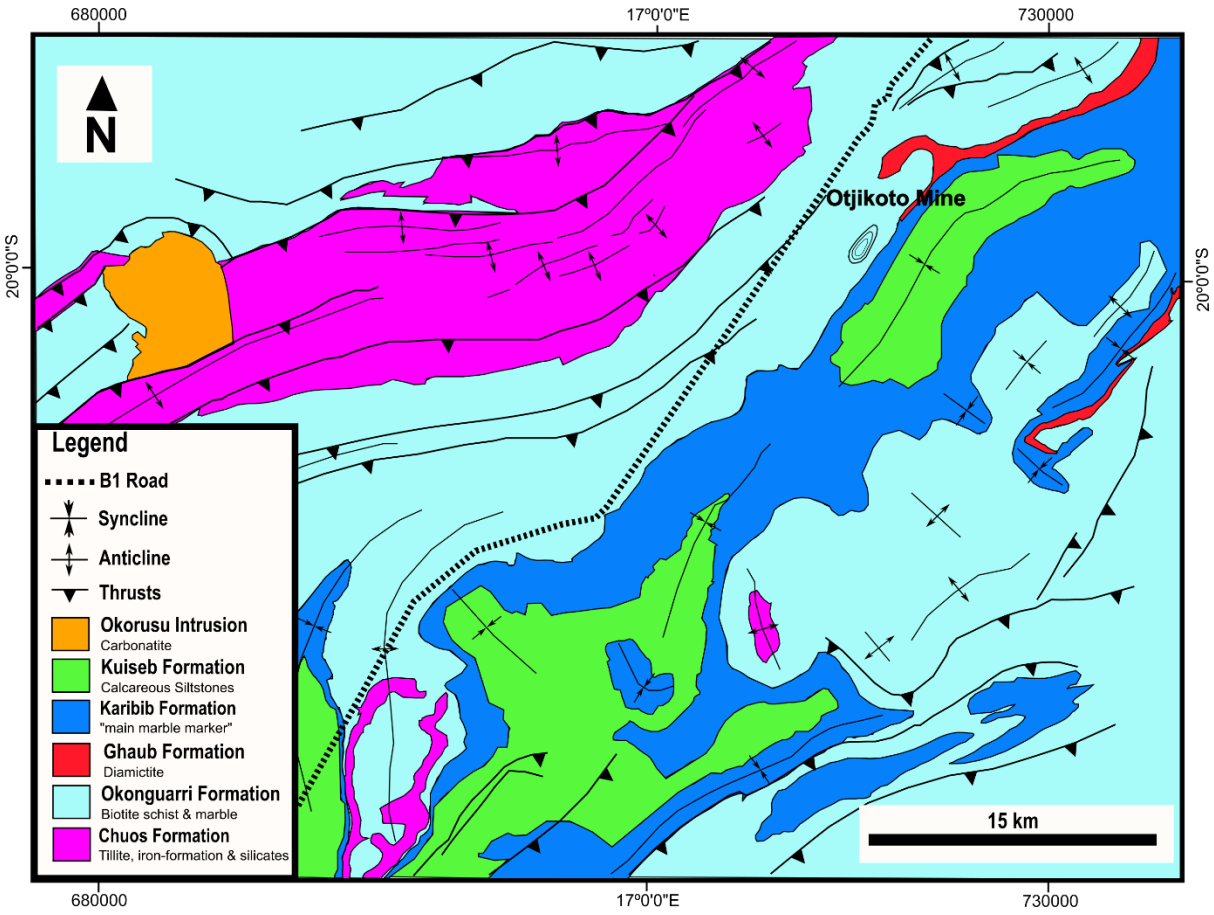

Figure 2-6 Geological map of the study area showing the different formations, members, thrusts and the position of the Otjikoto ine. (Modified after Knupp, 2012).

Chuos Formation

The Chuos Formation represents thick diamictite units which are found in many parts of the Damara Orogenic Belt (Miller, 2008). The Ghaub and Chuos Formations are separated by a 400m section, the Okonguarri antiform (Hoffmann et al., 2004). In the Northern Zone, the Chuos Formation is associated with iron formations and is relatively thin with a thickness of less than 50 m (Miller, 2008). To the west of Otjiwarongo, the Okonguarri Formation overlies the Chuos Formation (Hoffmann et al., 2004). The Chuos Formation, with its associated iron formations, is best exposed in the Okotjize fold area (Miller, 1983). The Ghaub Formation overlies the Chuos Formation within this area (Miller, 2008). The Chuos Formation attains a thickness of 200 m (Miller, 2008). The Chuos diamictite is brown in colour and contains dolomite-rich matrix with white dolomite pebbles (2-3 cm in size) in the layer (Miller, 2008).

Okonguarri Formation

The Okonguarri Formation attains a thickness of 4000 metres within the Northern Zone (Miller, 2008). It is made up of clastic turbidites and carbonates which underlay the Ghaub Formation and overly the Chuos Formation (Miller, 2008). The turbidites are largely made up of quartzites

(Miller, 1983). The mica content of the turbidites increases as they fine upwards from coarse grained bases to fine grained pelitic tops (Miller, 2008). The calcareous turbidites are found within nine zones that are interbedded with quartzitic turbidites (Miller, 2008). The interbedded turbiditic rock types consist of calcareous biotite schists, calcareous quartzites and dolomites (Miller, 2008). The dolomite layers are relatively thin with a maximum thickness of 80 cm.

Ghaub Formation

Within the Northern Zone, the Ghaub Formation overlies the Oberwasser member and underlies the Karibib Formation. The Formation is part of the Swakop Group and conformably overlies the Okonguarri Formation as shown in Figure 2-5. Within the zone, the diamictite makes up the main and lower part of the Formation. These diamictites achieve thicknesses in the range of tens of metres (Miller, 2008). The diamictite is then followed by thin shales and siltstones, of a few metres in thickness, which occur parallel to the bedding and contain dropstones (Miller, 2008). The overlying cap carbonate is a fine-grained silty dolomite with a thickness of 1-3 metres (Miller, 2008). The above sequence is thought to have been deposited in a proximal basin setting (Hoffmann et al., 2004). The clasts of the diamictites are dominated by granite and quartzites (Creus, 2011). The Ghaub Formation has an age of about 630 Ma (Hoffmann et al., 2004).

Karibib Formation

The Karibib Formation extends from the Southern Central Zone to the Northern Zone. In the thicker parts, the Karibib Formation consists of blue-grey bedded limestones and bedded conglomerates with granite pebbles. The blue-grey limestones are overlain by massive dolomite units. In the vicinity of the Okonguarri Antiform, the formation has blue-grey dolomitic limestones with bedded white marble and dolomite (Miller, 2008). The carbonates contain minor amounts of pyrite, tremolite and scapolite. Within the northern zone, the Formation is originally detrital to turbiditic as evidently shown by cross bedding, graded bedding, ripple marks and deep channel structures (Miller, 2008). The Karibib Formation is underlain by the Ghaub Formation as shown in Figure 2-5 and Figure 2-6. In the Okotjize fold area, the Formation consists of grey carbonates with thin white layers (Miller, 1983). Dolomite dominates the lower half of the Formation. The upper half of the Formation is dominated by limestone and marble layers (Miller, 2008). In the lower parts of the Formation, thin layers of chert are also present (Miller, 2008). The only occurrence of outcrops in the study area is that of the Karibib marble unit which signifies a marker horizon (McDonald et al., 2011). The Karibib marble is identified as a significant marker horizon as it forms ridges with good

outcrops that can be traced out in photo geology across the area (Van der Merwe & Jones, 2005). Rocks of the Karibib Formation forms the hanging wall at Otjikoto.

Kuiseb Formation

Stratigraphically, the Kuiseb Formation is the highest unit of the Swakop Group (Miller, 2008). It has no overlying Formation that can define it (Miller, 2008). The Formation covers a vast area and conformably overlies the marbles of the Karibib Formation (Miller, 2008). In the central part of the Northern Zone, the Kuiseb schists attains a thickness of 9800 m (Miller, 1983). Kuiseb Formation rock units are poorly exposed within the study area.

The Kuiseb Formation is characterised by quartz-albite-chlorite-biotite schists whereby the chlorite is mostly magnesium rich (Miller, 2008). The lowest unit of the Kuiseb Formation is made up of graded metagreywackes and the middle part is made up of graded metapelites (Miller, 2008 and Miller, 1983). The metapelite layer is more susceptible to weathering than the metagreywacke layer. The upper layer of the Formation is made up of graded coarse grained metagreywackes which are interlayered with orthoquartzites (Miller, 2008). Thin layers of bedded quartz, epidote, and tourmalinites are present at the base of the Formation (Miller, 2008). Other units of the Kuiseb Formation include garnet gneisses, migmatites, minor marble, graphitic schists and amphibole schists. Within the Northern Zone, the Kuiseb Formation schists have a single axial planar cleavage which is well developed (Miller, 2008 and Miller, 1983). The Formation forms synclinal structures within the central part of the Northern Zone (Miller, 2008). The fold mullions exhibit thin fold limbs and thick fold closures.

2.3 Structures

The Otjikoto deposit is hosted by structures such as shear zones, faults and thrust planes. Some of the major shears and thrust planes are shown in Figure 2-7. The structures are stratigraphically discordant and are commonly parallel to the bedding and fold hinges.

The rock units from the hanging wall to the footwall are generally dipping at 25° towards the southeast and have a strike close to 045°, northeast to southwest (Waldeck & Terbrugge, 2008). Parallel bedding, (S_o), and metamorphic banding, S_1, are the dominant foliations at Otjikoto (Lytle et al., 2013). The S_2 and S_3 foliations are less common at Otjikoto (Lytle et al., 2013). The primary sedimentary bedding (S_o) is well preserved in rocks at Otjikoto (Lytle et al., 2013). The rock units at Otjikoto have undergone more than three phases of deformation that has produced open and tight folding features. After the initial metamorphic event, the rocks

underwent metasomatism and then prograde regional metamorphism within the lower amphibolite facies (Lytle et al., 2013).

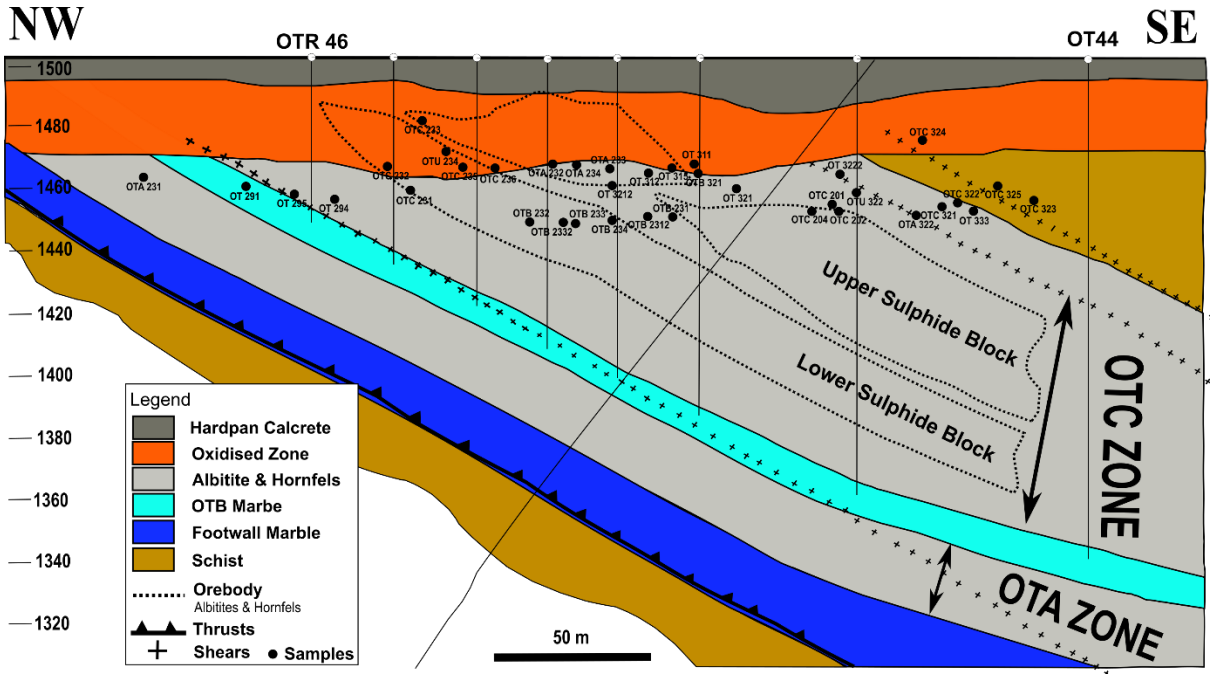

Figure 2-7 Northwest to southeast schematic cross-section of the Otjikoto Deposit showing the main mineralization zones, host rocks, thrusts and shear zone. The sample localities are also added to the cross section. Modified after Wanless et al. (2010)

Structural and veining features in the host rocks at Otjikoto signifies reverse to oblique thrust movements along the faults and shear zones (Tomkinson, 1999). Three metre and twenty metre thick shear zones were identified in boreholes OT26 and OT36 respectively (Waldeck & Terbrugge, 2008). The shear zones were persistent (1m in length), irregular on a macro-scale and undulating on a micro-scale, with joints (Waldeck & Terbrugge, 2008). The joints were generally soft-sheared (Waldeck & Terbrugge, 2008).

2.4 Mineralisation

The gold mineralization is related to a fabric-parallel sheeted vein network system (Figure 2-8) whereby the widths of the veins normally fluctuate (1 to 10 cm), with a positive correlation between the grade and the density of the veins (Waldeck & Terbrugge, 2008). The sheeted veins are positioned parallel towards the foliation (S_1) of the albitites and hornfels of the Okonguarri Formation. The sheeted veins strike towards the north east. (Van Der Merwe & Wanless, 2007). Petzel (2010) points out that the gold mineralisation is hosted in thin (<10 cm) quartz vein which lie parallel to the foliation of the schists and hornfels. The vein types include both quartz and carbonate hosted vein types. The veins are made up of magnetite, pyrite and

pyrrhotite which are associated with amphibole, almandine garnets, and free gold (Waldeck & Terbrugge, 2008). The gold deposition style is a little different from the Navachab mineralization style where the vein types are very variable (Van Der Merwe & Wanless, 2007).

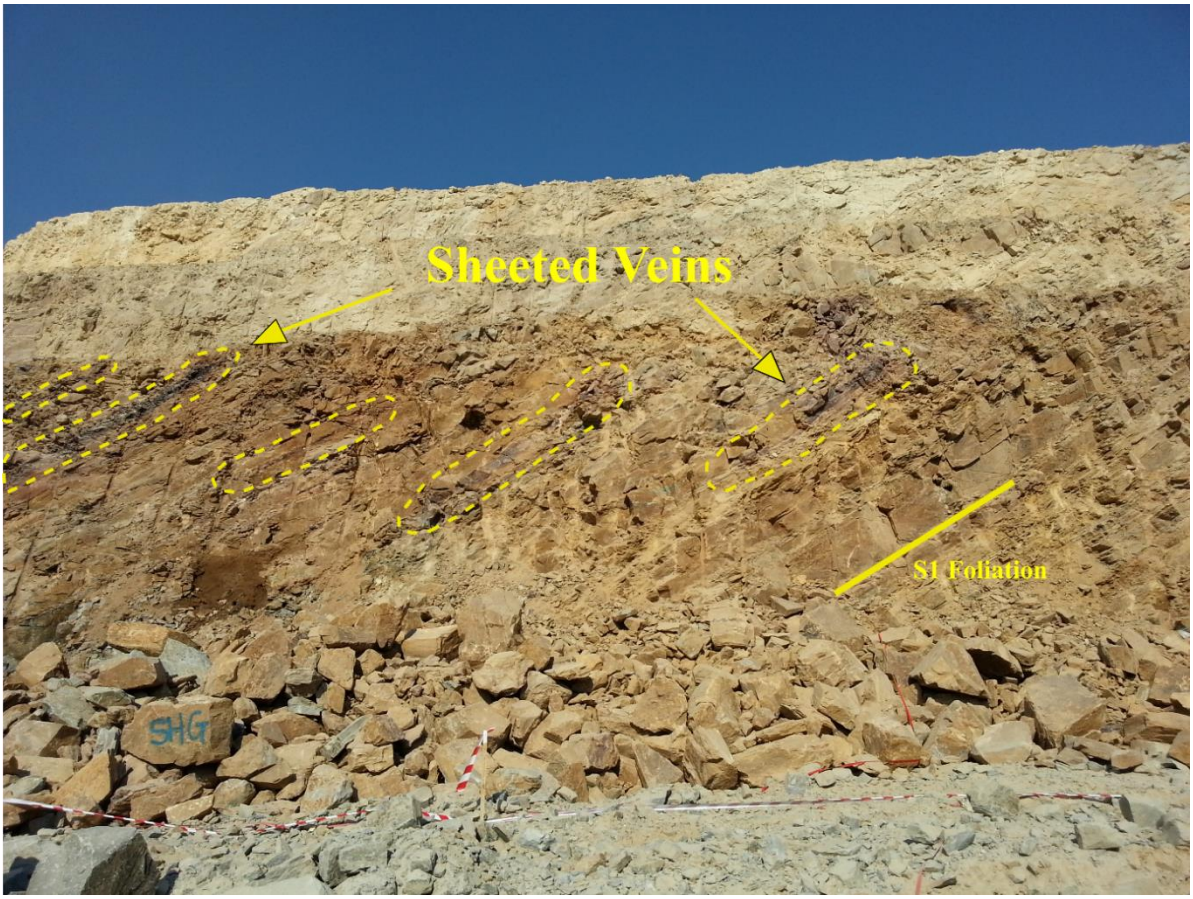

Figure 2-8 A photograph (east-west) taken from the pit at Otjikoto that shows the arrangement of the sheeted veins.

The sheeted vein system that hosts the gold mineralisation, occurs over a strike length of about 2 km to a depth of about 478 metres below the surface (Fletcher et al., 2013). The ore shoots with a higher gold grade are found in a series of northeast trending zones that are plunging at about 10-15° to the southwest (Fletcher et al., 2013). Although native gold is common at Otjikoto, the gold is associated with the veins (Fletcher et al., 2013).

The rock units intersected during a drilling campaign at Otjikoto were subdivided into lithostratigraphic units (Fletcher et al., 2013). The intersected units were dipping at an angle of about 25° towards the east and striking northeast (Fletcher et al., 2013). The subdivided rock units are made up of an upper magnetite zone which overlies a garnet-biotite schist zone and a lower OT (stands for Otjikoto) unit package (Fletcher et al., 2013). The lower OT unit package is further subdivided into the OTC zone, OTB marble zone, the OTA zone and a footwall marble as shown in Figure 2-7 (Fletcher et al., 2013). The OTC zone contains the main gold mineralisation and is made up of albitites and amphibole-albite hornfels (Fletcher et al., 2013).

The 10 metre thick OTB marble zone underlies the OTC zone. The footwall marble and OTB marble zone act as marker horizons within the stratigraphy (Fletcher et al., 2013). The petrographic studies led to naming the main rock types as biotite schist, albite hornfels and amphibole-albite hornfels (Fletcher et al., 2013). The albite hornfels was further subdivided into biotite albite, which is albite with visible biotite, and albitite, which is an equi-granular albite rich rock unit (Fletcher et al., 2013). The OTA zone and magnetite zone are dominantly made up of Albitite (Fletcher et al., 2013). The OTB and footwall marble units are recrystallized coarse grained marble units which contain variable amounts of ankerite and dolomite content (Fletcher et al., 2013). Gold mineralisation is hosted by the albitite and amphibole-albite hornfels of the OTC zone (Fletcher et al., 2013). The pyrite, magnetite and pyrrhotite minerals occur in epigenetic veins within the OTC zone (Fletcher et al., 2013).

3 Analytical Methods

This section reviews the methodology and analytical techniques carried out to achieve the aims and objectives of this study. Figure 3-1 illustrates the sequences and procedures followed during this study. The analytical methods employed are electron microprobe analysis, XRF analysis, ICP-MS analysis, stable oxygen isotopes, petrography and fluid inclusion studies. Detailed descriptions for each method are presented below.

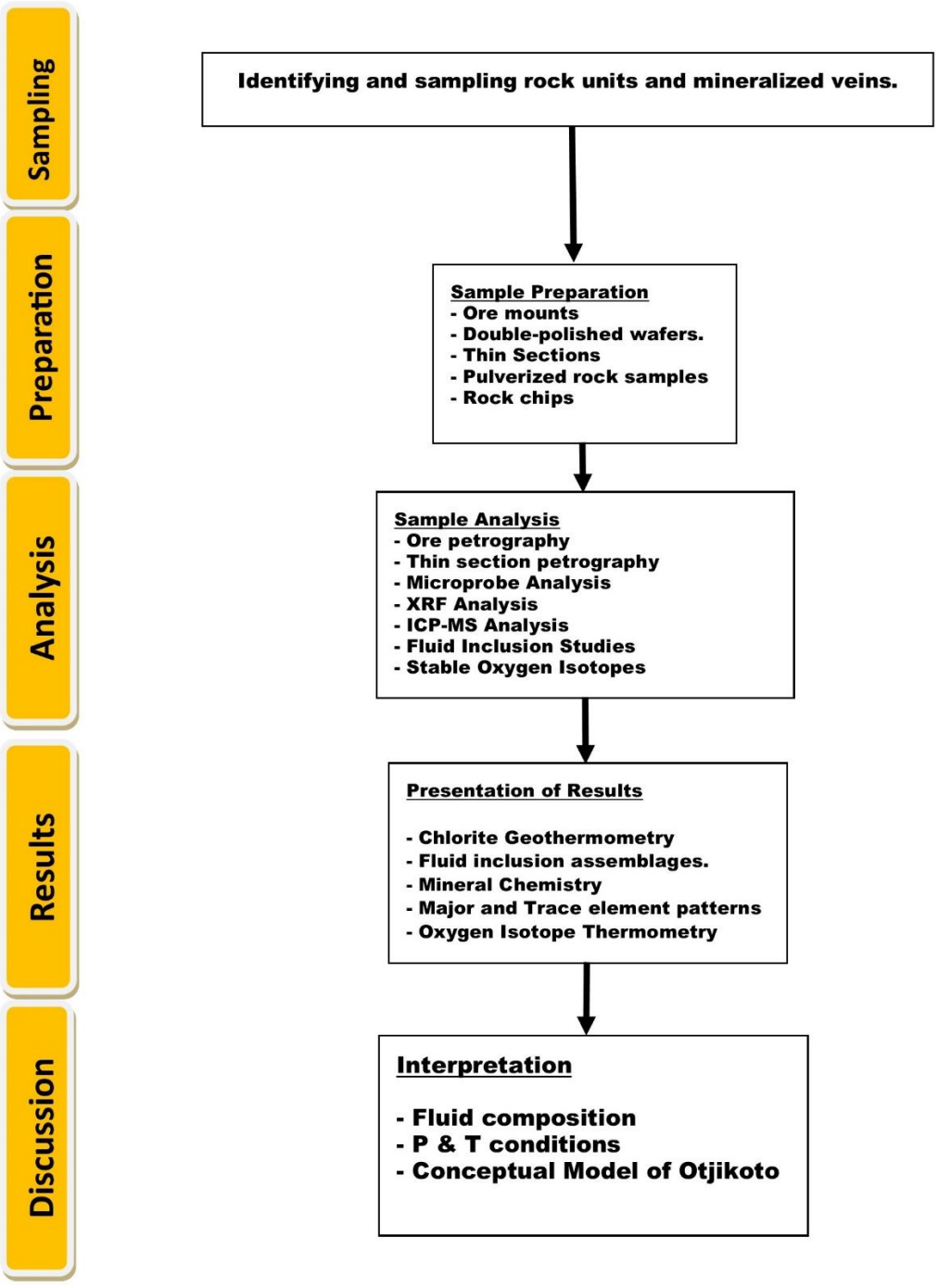

Figure 3-1 A process flowchart that shows the methods applied during this study

3.1 Sampling

Grab samples of 54 samples (about 5 kg) were collected by the author from the footwall to the hanging wall of the Otjikoto Deposit, within the open pit area of the gold mine. The sampling procedure took place over a 3 months period. Two to six representative samples of each rock type were collected with a greater number of samples for the albitite unit, which is the main host rock. The rock types, block numbers and coordinates of the samples collected from the Otjikoto gold mine are summarised in Table 10 within the appendix.

The sample collection technique was relatively consistent for every rock type that was sampled. 50 in-situ samples were collected from exposures in the mining pit. A few of the samples were washed with water to remove visible weathering grains and dust from the mine's blasting activity. The samples were collected from mining blocks and immediately placed into a sample bag. Maps were drawn along east-west (Figure 3-3) and north-south (Figure 3-2) directions along exposure lengths ranging between 10 to 30 metres.

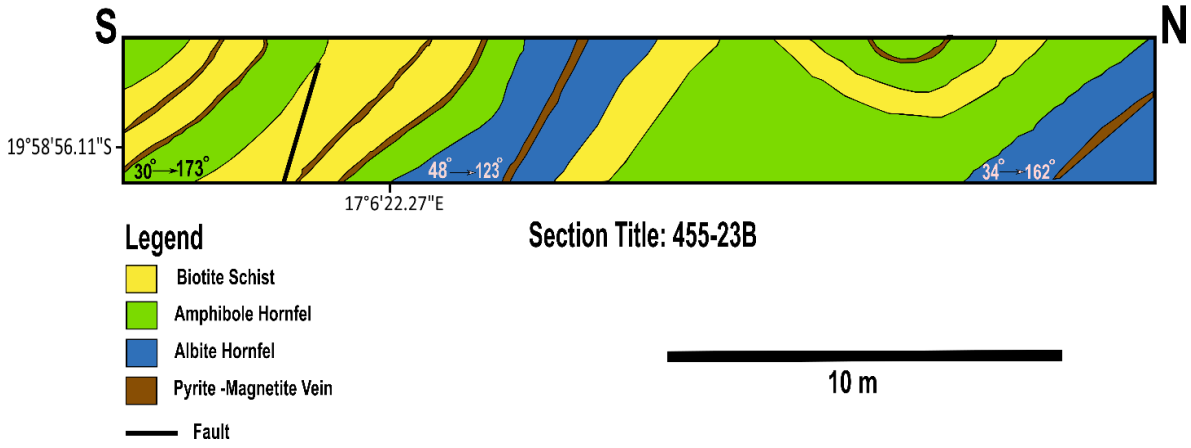

Figure 3-2 Section of block 23B

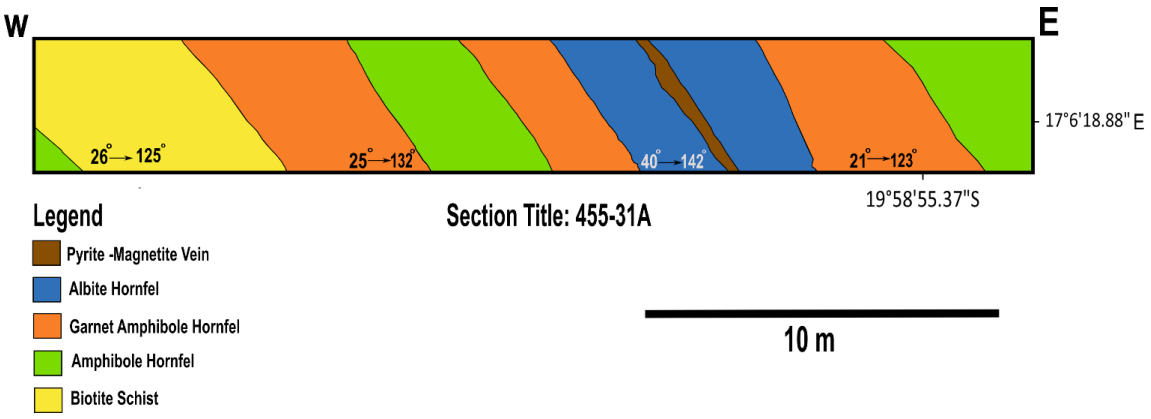

Figure 3-3 Map section of block 31A

The purpose of the face section maps were to capture the arrangement of the rocks surrounding the sample collection sites, before the samples were collected. The bagged samples were then transported to the mine's sample farm for temporary storage. A map showing sampling localities is shown in Figure 3-4 below.

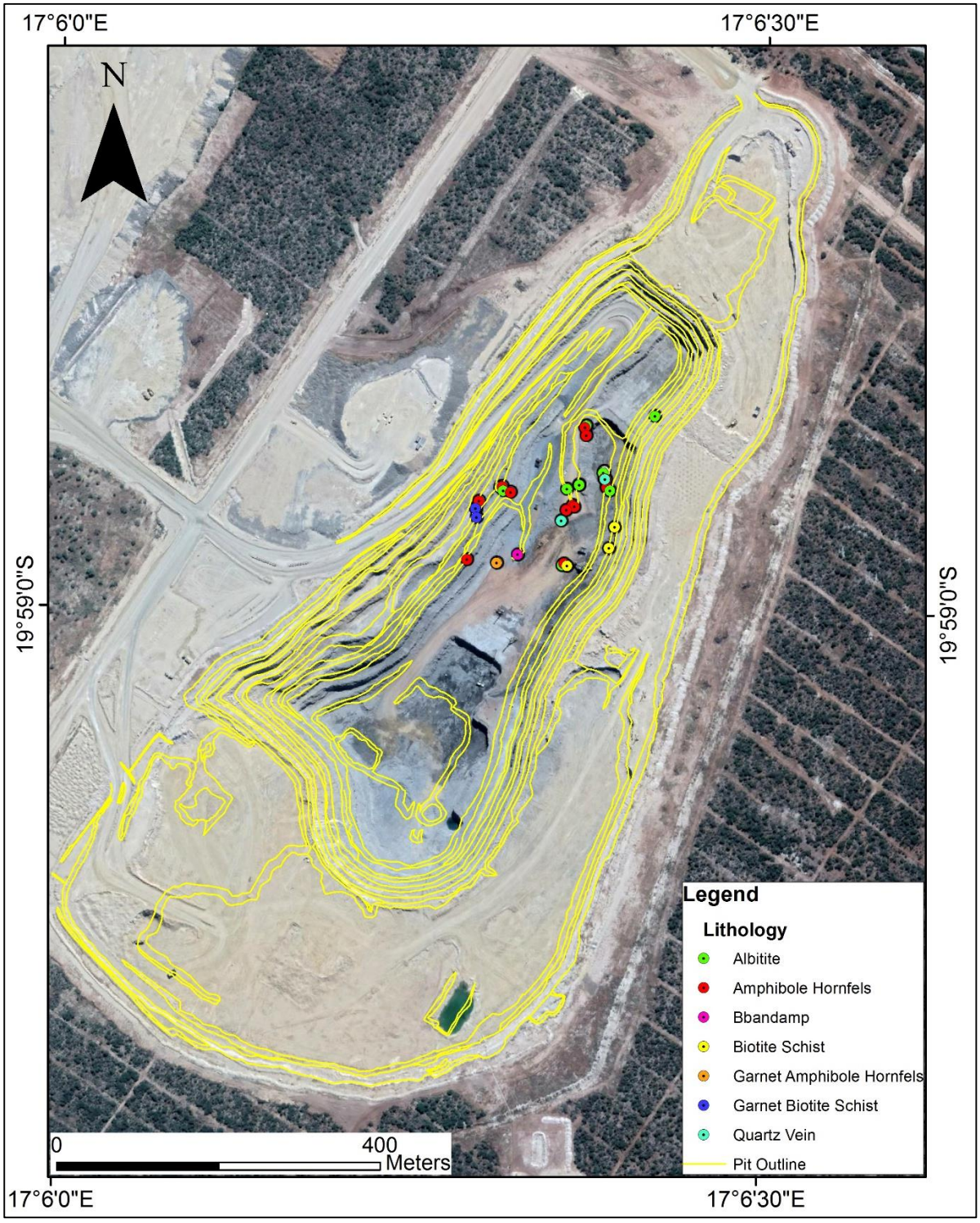

Figure 3-4 Sample Localities of the study area overlain on a google earth satellite image of the Otjikoto Mine. The yellow outline represents the pit outline in early 2016.

On close inspection, samples OTC232, OTC233, OTU235, OTC239, OTC236, OTC2310, OTU235, OTU322, OTU234, OTC203 and OTB234 contained visible ore minerals including magnetite, pyrrhotite, and pyrite. The remaining samples do not have visible occurrences of ore minerals. With the assistance of B2 Gold Namibia, the samples were subsequently transported to the University of Cape Town's Department Geological Sciences and made available for this study.

3.2 XRF Analysis

Major elements (Ti, Mn, Fe, K, Ca, Si, P, S, Mg, Na and Al) and some of the trace elements (Rb, Sr, Zr, Nb and Y) were analysed on the Otjikoto samples by using the XRF available at UCT's Department of Geological Sciences. The samples were crushed and milled to a powder form before analysis took place. The analysis was carried out by using the Panalytical Axios XRF spectrometer which consist of a rhodium end-window X-ray tube and a sample-changer with a sample capacity of 56. Major oxides are measured on fused disks prepared from ignited powder. The fusion disk preparation process was aided with a Claisse Fluxer. The XRF equipment was calibrated by using international standards, as determined by the geological sciences department. The Philips X-Ray analyser was set to 40 kV and 25 mA. The sample preparation procedure, as applied by Chetty (1998) and Duncan et al. (1984), was carried out. The lower limit of detection for the major oxides is 0.01 wt. %

3.3 Multi-Element LA-ICP-MS

The whole-rock analysis of trace elements by laser ablation procedure was undertaken on 24 non-mineralised representative rock samples collected during the sampling phase at the Otjikoto mine. The analysis was carried out at the University of Stellenbosch's ICP-MS and XRF laboratory facility. The trace elements in the rock were analysed on polished mounts from fusions. The LA-ICP-MS equipment consists of a Zeiss Merlin Fe SEM microscope for image acquisition, a cathodoluminescence detector and a smart SEM software (Frei & Gerdes, 2009). The attached Resonetics 193 nm excimer laser has energy output of 6.2 J per cm^2 and a frequency of 10 Hz. Two spots of 100 µm per sample were measured. The laser acceleration voltage was 20 kV with an 11nA beam current and a lower detection limit of 0.01 ppm. The calibration used was a BHVO-1 glass. The readings were taken with the laser ablation sector field inductively coupled plasma mass spectrometry (LA-SF-ICP-MS) which was connected to an M-50-SE excimer laser (Frei & Gerdes, 2009). The data was filtered with a 2σ error.

A resonetics 193 nm excimer laser was used for the analysis. The energy emitted was 6.2 J per cm^2. The frequency for the analysis was 10 Hz. There were two spots of 100 µm per sample. The ablation gas used was helium at 0.35 L per minute. The ablation time was 15 seconds background and 35 seconds ablation. The carrier gases used for the ICP-MS were argon at 075 L per minute and nitrogen at 0.004 L per minute.

3.4 Electron Microprobe Analysis

The microprobe analysis was carried out by using UCT's JEOL Super probe JXA-8100 electron probe micro analyser, which has 4 energy dispersive wavelength spectrometers and crystals that were able to measure major interesting elements of geological nature. The microprobe equipment contains a 2 gas flow proportional for light elements and for heavy elements, and two xenon detectors which are sealed. In addition, the micro analyser also contains secondary electron, backscattered electron and cathodoluminescence detectors. As a standard, synthetic and natural minerals were used (Finkelstein, 2010). The samples were analysed with a current of 20 µm, an acceleration voltage of 15 kV and a beam diameter of 3 µm. The parameters used in calibrating the electron microprobe are shown in Table 12 within the appendix section.

3.2 Fluid Inclusions

3.2.1 Microthermometry

Microthermometry was carried out within the Geological Sciences Department at the University of Cape Town. This was carried out by using a THMSG600 Linkam heating-freezing stage which is connected to a liquid nitrogen pump, a computer and a TMS 94 temperature programmer. The success of the method depends upon accurately identifying fluid inclusions and then looking through the microscope to identify phase changes during the heating and cooling. Phase changes occur at different temperatures. The THMSG600 heating-freezing stage can measure temperatures ranging between -197 °C and 600°C.

Types of temperature measurement for fluid inclusions

- **Th tot** – The temperature of total homogenisation
- **Th (CO_2) -** Homogenisation temperature of CO_2
- **Tm halite** – Temperature of halite dissolution
- **Tm (ice)** – Final temperature of ice melting in aqueous-carbonic and aqueous inclusions.

- **Tm (cla)** – Final temperature of clathrate melting
- **Tm (CO_2)** – Final temperature of CO_2 melting

3.2.2 Calculations

Salinity calculations for aqueous inclusions

The ice-melting temperature is used for determining the NaCl composition when the weight percentage of salinities is less than 23.2 wt. % NaCl (Goldstein & Reynolds, 1994). Tm (ice) was calculated by using a simple equation by Bodnar (1993) (Goldstein & Reynolds, 1994).

$$\text{Salinity (wt. \%)} = 0.00 + 1.78\,\theta - 0.0442\,\theta^2 + 0.000557\,\theta^3 \qquad \text{(Equation 3.1)}$$

Where θ is the melting temperature of ice (Tmice) in °C

The temperature of halite dissolution (Tm halite) was used for determining the salinities of inclusions with daughter crystals (>23.2 wt. % NaCl). The equation for calculating the salinity from halite dissolution is (Goldstein & Reynolds, 1994):

$$\text{wt.\% NaCl} = 26.242 + 0.4928\theta + 1.42\theta^2 - 0.223\theta^3 + 0.04129\theta^4 + 0.006295\theta^5 - 0.001967\theta^6 + 0.0001112\theta^7 \qquad \text{(Equation 3.2)}$$

Where θ = Tm halite in °C/100

Bulk Density

Using the temperature of ice melting as a variable (Tm ice), the bulk densities of the aqueous inclusions were calculated by using the computer program BULK (version 06/02) (Bakker, 2003). The composition and homogenisation temperatures were used to calculate the bulk densities of the carbonic inclusions. The equation of state used was by Thiery et al., (1994). The isochores of the aqueous and carbonic inclusions were plotted by using the software ISOC (version 06/02) (Bakker, 2003).

3.3 Stable Isotopes

Oxygen isotopes were determined on quartz and magnetite mineral grains from four samples (OTC239, OTU322, OTC2311 and OTC232). The laser fluorination method by Harris and Vogeli (2010) was used. All the oxygen isotope ratios were measured offline by using a Finnegan Mat Delta XP mass spectrometer in dual inlet mode. The data is presented in the

standard δ notation whereby δ = ((R sample/R standard)-1) x 1000, R = $^{18}O/^{16}O$ and SMOW is the Standard Mean Ocean Water. The oxygen isotope ratios were measured on O_2 glass.

With each batch of 10 samples, the internal standard of the monastery garnet (MON GT) was analysed in duplicate. MON GT has a $\delta_{18}O$ value of 5.38 ‰ calibrated against the UWG-2 garnet standard of Valley et al. (1995), with an assumption of a $\delta_{18}O$ value of 5.80 ‰ for UWG-2. The raw data was converted to the SMOW scale by using the average $\delta_{18}O$ value of MON GT (Harris & Vogeli, 2010). The long-term average difference in $d_{18}O$ values of 2 internal MONT GT standards run with each batch of 10 samples was 0.11‰ (n = 216), corresponding to a 2σ value of 0.15‰.

4 Petrography

4.1 Hand Specimen Descriptions

Biotite Schist

In hand specimen, the biotite schist from Otjikoto has a coarse grained texture as shown in Figure 4-1 (Image A). The rock unit has a light grey to dark grey fresh colour. The unit exhibits a weakly developed schistosic texture. The grain sizes of the constituent minerals range from 100 µm for the quartz mineral to 1500 µm for the elongated amphibole mineral. The biotite is subhedral. The rest of the dominant minerals, i.e. albite, amphibole, quartz and dolomite, do not have a characteristic crystal shape (anhedral).

Garnet Biotite Schist

In hand specimen, the garnet biotite schist from Otjikoto has a medium grained texture. The garnet grains are easily recognisable as red porphyroblasts as shown in Figure 4-1 (Image E) below. The general sequence of events that form a garnet porphyroblast are as follows (Passchier & Trouw, 1996): (1) A foliation develops, (2) a porphyroblast overgrows on the foliation and (3) deformation, recrystallization and grain growth then destroys the orientation of the matrix and then a S_2 foliation develops. The amphibole grains are elongated and easily distinguishable. The rock unit has a greyish to greenish colour. The rock has a foliated texture with a moderately developed schistosity and weakly formed cleavage planes. The grain sizes of the dominant minerals range from 50 µm for quartz to 2.5 mm for large almandine grains. The garnet grains exhibit well-formed characteristic crystal shapes. The biotite, amphibole, quartz and albite grains do not exhibit characteristic crystal faces (anhedral).

Albitised Biotite Schist

In hand specimen, the albitised biotite schist from Otjikoto has a medium to coarse-grained texture as shown in Figure 4-1 (Image C) below. Minor amounts of large almandine garnet grains (<1.5 mm) are visible in the rock unit. Small tourmaline grains are visible in the rock unit. The rock unit has a dark grey to dark green colour with red zones that are caused by the breakdown of almandine in the rock unit. The biotite grains are distinctly elongated in one direction, giving the rock unit a banded appearance. The grain sizes of the dominant minerals range from 50 µm for the albite to 1.5 mm for almandine. The tourmaline and almandine have well established crystal faces (euhedral) while the biotite, albite and dolomite are anhedral.

Albitite

In hand specimen, the albite hornfels from the Otjikoto gold deposit, which is commonly referred to as an albitite, generally has a fine grained textural appearance as shown in Figure 4-1 (Image D). The dominant albite mineral (60%) gives the rock unit a light green to greyish colour. The grain size ranges between 50 µm for the quartz to 300 µm for the albite. The overall texture of the rock unit is non-foliated granoblastic. This implies that the albite hornfels has undergone recrystallization under minimal deviatoric stress. The quartz, albite and dolomite grains are all anhedral as the grains do not exhibit well defined crystal faces.

Amphibole Hornfels

In hand specimen, the amphibole hornfels from the Otjikoto Deposit exhibits a fine to medium grained textural appearance. The rock unit has a distinctive greyish to greenish colour which is caused by the abundance of albite. The rock contains distinctive fine grained porphyroblasts of amphibole as shown in Figure 4-1 (Image F). Small amounts of chlorite are present with a light green colour. The grain sizes of the dominant minerals range between 200 µm for the chlorite and 2 mm for the large elongated amphibole porphyroblasts. The overall texture is granular with equi-dimensional grains, which can be interpreted as a granoblastic texture. The quartz and albite grains are anhedral as they do not have well defined crystal faces.

Garnet Amphibole Hornfels

In hand specimen, the garnet amphibole hornfels from the Otjikoto stratigraphy shows a fine grained textural appearance. The dolomite is slightly parallel to the mineral banding in the hornfels. The almandine and amphibole minerals form distinct porphyroblasts in the rock unit as shown in Figure 4-1 (Image B). The colour of the rock unit is light green to grey with minor bands. The grain sizes of the dominant minerals range from 100 µm for the albite to 4 mm for almandine. The overall texture is granular (non-foliated) with large porphyroblasts of almandine. The almandine grains are distinctly euhedral with well-formed crystal faces while

the biotite, quartz and albite grains is anhedral with no characteristic crystal faces. The visually estimated mineral composition of the rock units from the Otjikoto gold mine have been summarised in a table within the appendix section.

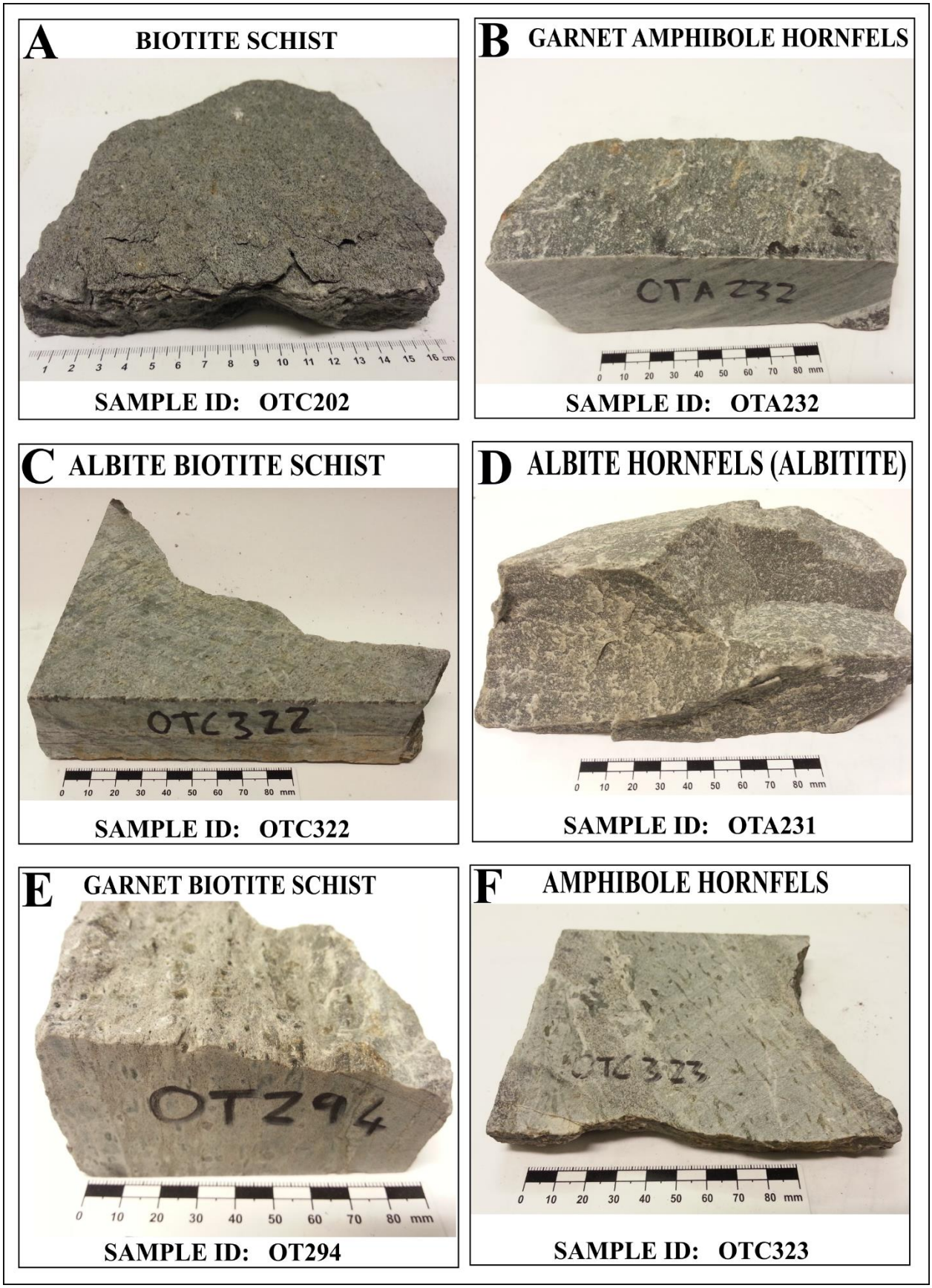

Figure 4-1 Hand specimen of the main rock types from the Otjikoto gold deposit. Image A shows a coarse grained biotite schist (OTC202). Image B shows the garnet amphibole hornfels with garnet porphyroblasts (OTA232). Image C shows the Albite biotite schist (OTC322). Image D shows the fine-grained albite hornfels (OTA231). Image E displays the garnet biotite schist with large garnet porphyroclasts (OT294). Image F shows the amphibole hornfels with amphiboles aligned parallel to the foliation (OTC323).

Pyrite-Magnetite Vein

Gold mineralisation at Otjikoto occurs in bedding parallel sheeted veins which are hosted by albitites, biotite schists and amphibole hornfels of the Okonguarri formation. No visible gold was observed in hand specimen collected from the field. The gold at Otjikoto commonly precipitates together with pyrrhotite, pyrite, chalcopyrite and magnetite. Pyrrhotite and magnetite are used as indicator minerals to decipher the presence of gold.

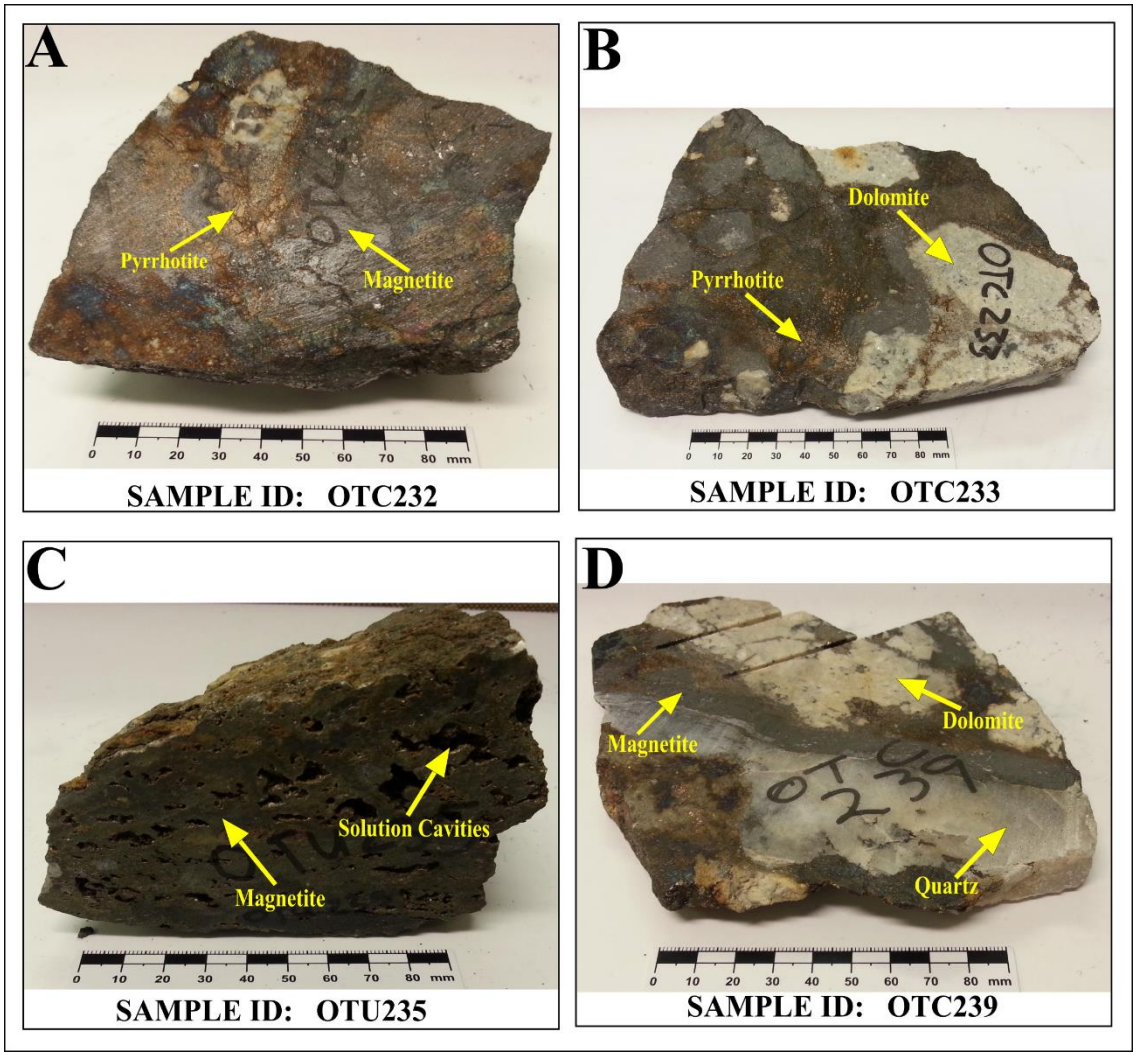

Figure 4-2 Hand specimen of the pyrite-magnetite veins from the Otjikoto gold deposit. Image A shows the pyrrhotite and magnetite visible in the disseminated vein (OTC232). Image B shows pyrrhotite and magnetite interlocked between dolomite grains (OTC233). Image C shows solution cavities found within the magnetite and pyrite grains (OTU235). Image D shows an intergrowth of magnetite within a dolomite matrix (OTC239). A quartz vein is also shown within image D (OTC239).

The sulphide vein exhibits a massive texture with pyrite and magnetite cross-cutting across the foliation. The vein is rich in carbonate (dolomite) grains which are intergrown with the pyrrhotite and magnetite as shown in Figure 4-2 (Image B and D). Image D also shows a quartz vein being introduced into the groundmass. The hand specimen unit is very dense. Pyrrhotite and magnetite are easily distinguishable in the samples as shown in Figure 4-2 (Image A)

below. Almandine porphyroclasts are present in most of the veined samples. Magnetite and pyrrhotite have grain sizes in excess of 1000 μm. The dolomite zones contains pyrrhotite and minor pyrite as shown in Figure 4-2 (Image B). The magnetite and pyrite form a coarse-grained texture with solution cavities visible as displayed in Figure 4-2 (Image C) below. The solution cavities are not filled with any material.

4.2 Thin Section Petrography

4.2.1 Biotite Schist

In thin section, the minerals visible are biotite, quartz, albite, and amphibole. Modal abundances of these minerals are summarised within table 11 of the appendix. Opaque minerals, pyrite and magnetite, are visible in thin section. The biotite schist is foliated and characterised by biotite oriented in a preferred direction, perpendicular to foliation as shown in Figure 4-4 (Image C and D).

The biotite exhibits a decussate texture as illustrated in Figure 4-4 (Image C and D) which consists of interlocking elongated and prismatic biotite grains that are randomly oriented within the ground mass. The decussate texture implies that the biotite grains are approaching textural equilibrium, although the crystals do not exhibit an equidimensional texture (Yardley et al., 1990). In the biotite schist (OT293), Figure 4-5 (image D), an assemblage of qtz + alb + amp +bio is observed.

4.2.2 Garnet Biotite Schist

In thin section, the minerals visible are biotite, quartz, plagioclase, amphibole and garnet (almandine). Modal abundances of these minerals are summarised within table 11 of the appendix. Opaque minerals, pyrite and magnetite, are visible in the thin sections. The garnet biotite schist is sheared in thin section. Minor occurrences of chlorite and muscovite are discernable in thin section. Almandine occurs as porphyroblasts surrounded by a quartz and albite rich matrix (Figure 4-3). This implies that the complex texture formed over a period of at least two deformation stages. Chlorite grains are replacing biotite which means that the rock unit underwent retrograde metamorphism under decreasing temperature conditions. The primary mineralogy of the garnet biotite schist is exhibited in the intermediate amphibolite facies. These conditions are prevalent during barrovian metamorphism. In the garnet biotite schist (OT294), Figure 4-5 (image A), an assemblage of qtz + bio + chl + grn is preserved.

The garnet porphyroclast form a ribbon texture as shown in Figure 4-3 (Image C and D). The mylonite has formed as the garnet biotite schist underwent intense strain. The quartz grains surrounding the garnet porphyroclast may have undergone syn-tectonic recrystallization. The mylonite shows that the grains surrounding the garnet porphyroblast underwent the most straining to form a ribbon texture (Yardley et al., 1990). The minerals are reduced to fine grained material in parts of the rock where deformation was greater, usually in strain shadows (Yardley et al., 1990). The most common interpretation is that the porphyroclasts of the ribbon texture were rolled by shearing parallel to the plane of schistosity (Yardley et al., 1990).

4.2.3 Albitised Biotite Schist

In thin section, the minerals visible are biotite, albite, dolomite, garnet and quartz. Modal abundances of these minerals are summarised within table 11 of the appendix. In polarised light, the albitised biotite schist has an evenly dispersed texture. The quartz grains exhibit undulate extinction with a strain shadow. The rock exhibits a granoblastic (equigranular) texture with albite and quartz grains forming small porphyroclasts. Biotite forms a decussate texture with intergrowths of albite, quartz, and small amounts of chlorite.

4.2.4 Albite hornfels (albitite)

The Albite Hornfels exhibits a granoblastic polygonal texture as shown in Figure 4-4 (Image E and F). In thin section, the minerals visible are albite, quartz and carbonate (dolomite) in an evenly dispersed matrix. Albite exhibits twinning. Opaque minerals, most likely magnetite and pyrite, are visible in thin section. Dolomite is found between opaque veins. In thin sections, the opaque minerals form a sieve texture. This texture usually results from fluids infiltrating the rock unit after recrystallization. Minor occurrences of muscovite are also visible in thin section (Yardley et al., 1990). Opaque minerals formed along a crack in a plane perpendicular to the foliation as shown in Figure 4-3 (Image A and B). The replacement of biotite by chlorite is a retrograde reaction. An assemblage of qtz + alb + chl has been observed in the albitite (OTA234), Figure 4-5 (Image B). Chlorite grains are visible in the quartz and albite matrix.

4.2.5 Amphibole Hornfels

In thin section, the minerals visible are albite, quartz, albite, and amphibole grains. Modal abundances of these minerals are summarised within table 11 of the appendix. Amphibole porphyroclasts are present in thin section which implies that the mineral might have formed by recrystallizing existing minerals during the metamorphic event. Opaque minerals, most likely

magnetite and pyrite, precipitated in the groundmass. Although rare, garnet minerals do occur and show a breakdown to chlorite. The amphibole hornfels (OTC323), Figure 4-5 (Image C) has an assemblage of qtz + amp + chl.

A granoblastic (polygonal) texture is exhibited by amphibole, as shown in Figure 4-3 (Image E and F). The amphibole has straight boundaries with an intersection of three grains. A granoblastic (polygonal) texture implies that the amphiboles were closely approaching textural equilibrium (Yardley et al., 1990).

4.2.6 Garnet Amphibole Hornfels

In thin section, the minerals present are quartz, biotite, chlorite and albite in addition to large grains of almandine and amphibole. Modal abundances of these minerals are summarised within table 11 of the appendix. Chlorite is replacing amphibole in the thin section as shown in Figure 4-4 (Image A and B). This suggests that the garnet amphibole hornfels has undergone retrograde metamorphism under decreasing temperature conditions. When chlorite is a secondary retrograde mineral, the rock unit was exposed to the lower grade greenschist facies after originally being formed in the amphibolite facies (Yardley et al., 1990). Opaque minerals, pyrite and pyrrhotite, are visible in the thin sections. The quartz and albite minerals exhibit a seriate texture.

Central porphyroblasts of garnet are visible in the garnet amphibole hornfels as illustrated in Figure 4-5 (Image E and F). Porphyroblasts provide clues on the tectonic setting and metamorphic event (Passchier & Trouw, 1996). Porphyroblasts are common in aluminium silicates (biotite, staurolite, garnet etc.) and are developed in upper greenschist to amphibolite metamorphic facies (Passchier & Trouw, 1996).

At Otjikoto, the euhedral porphyroblasts of garnet are reported to show strong mineralogical banding (Fletcher et al., 2013).

The visually estimated mineral composition of the thin sections from the Otjikoto gold mine have been summarised in the appendix (*Table 11*).

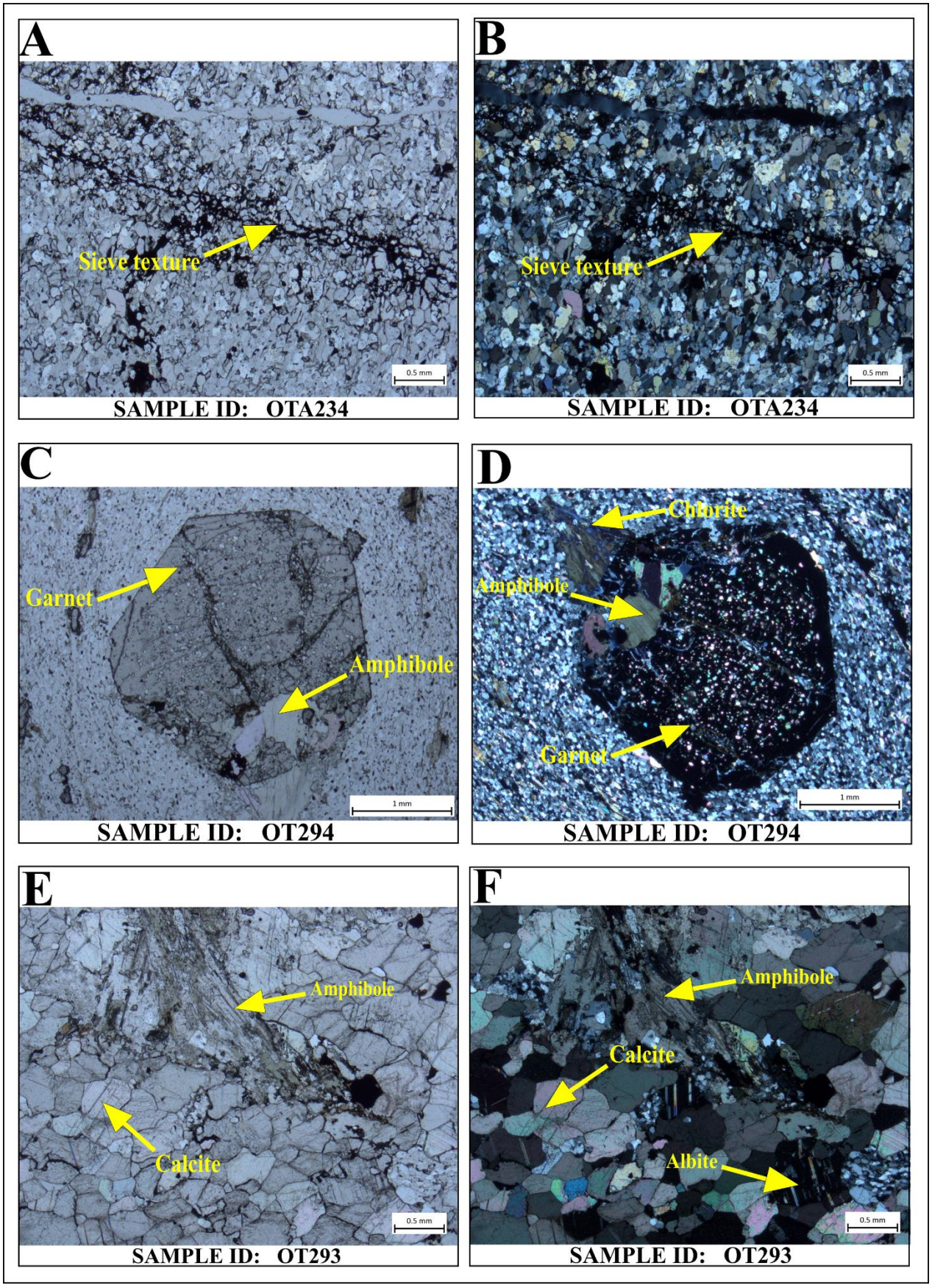

Figure 4-3 Photomicrographs under plane polarised light (PPL) and cross polarised light (XPL) showing the different types of metamorphic textures exhibited by rocks from Otjikoto. Image A and B display a sieve texture in the Albite Hornfels where magnetite (mag) forms along cracks in sample OTA234. Image C and D shows a mylonite being formed around a garnet porphyroclast, forming a ribbon texture in the garnet biotite schist (OT294). Image E and F displays a granoblastic texture in the amphibole hornfels with the amphibole forming a triple juction (OT293).

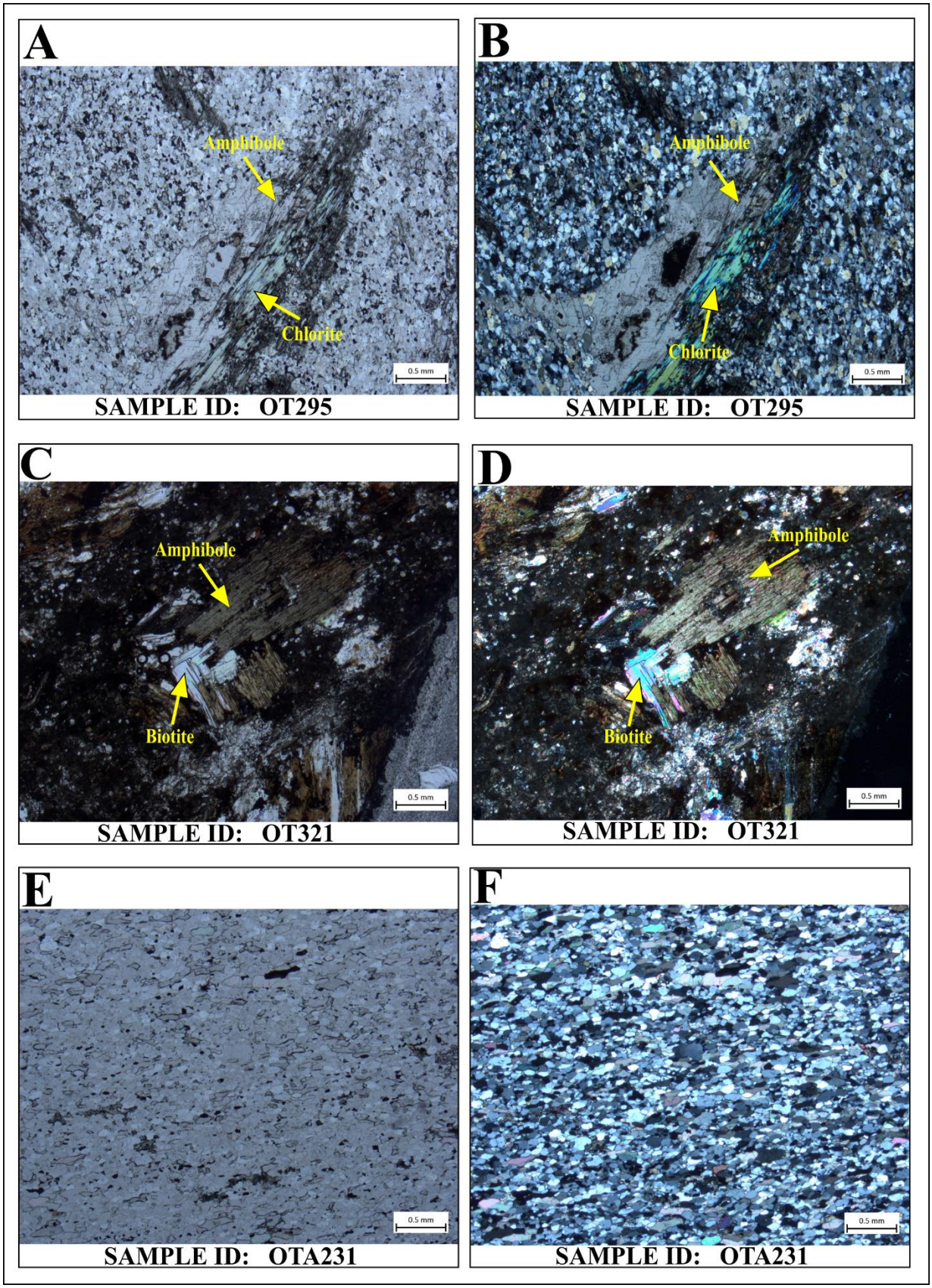

Figure 4-4 Photomicrographs under plane polarised light (PPL) and cross polarised light (XPL) showing the different types of metamorphic textures exhibited by rocks from Otjikoto. Image A and B display a replacement texture in the garnet amphibole hornfels where chlorite is replacing amphibole (OT295). Image C and D displays a dessucate texture in the biotite schist (OT231). Image E and F shows a granoblastic texture in the albitite (OTA231).

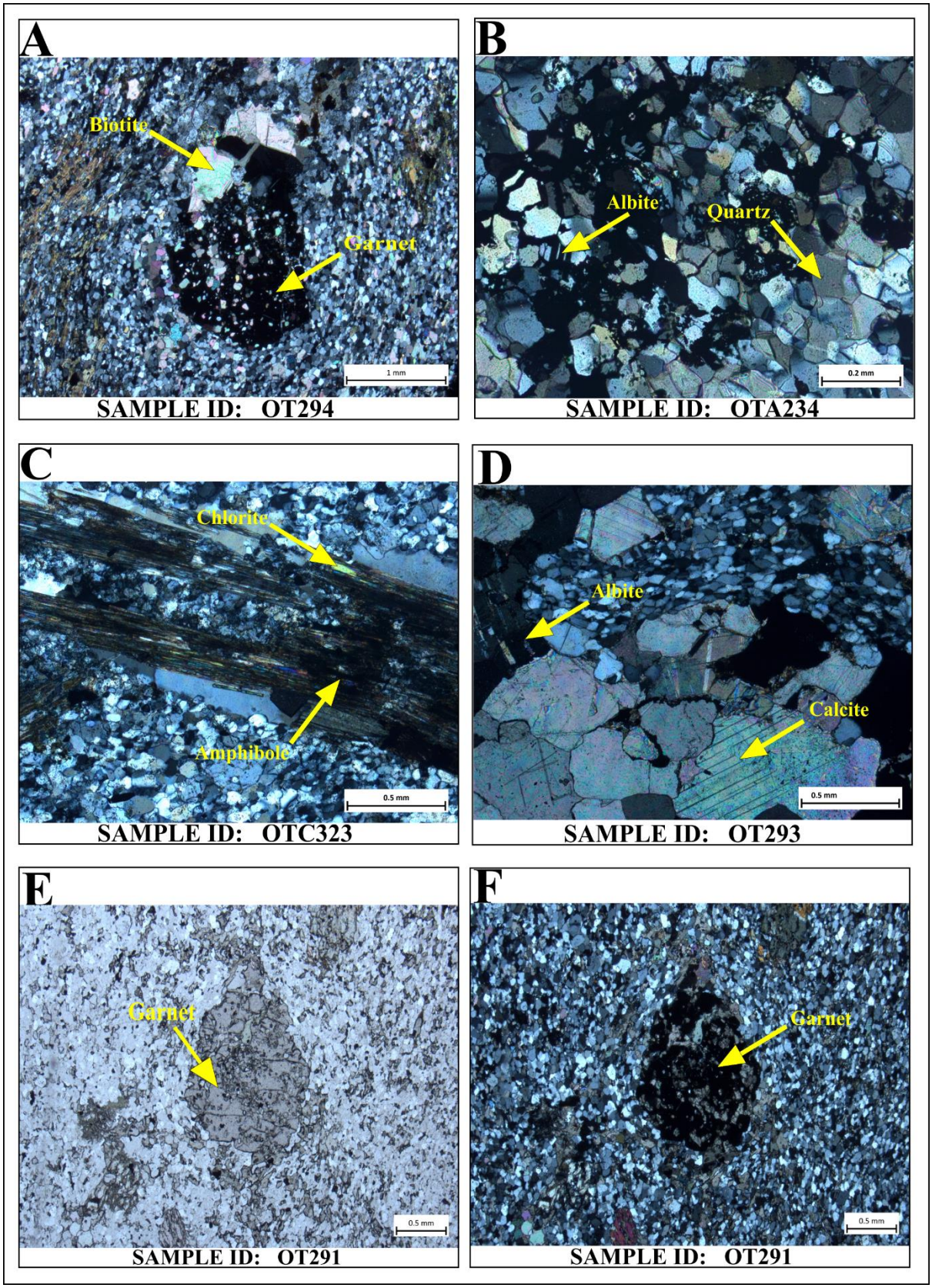

Figure 4-5 Photomicrographs under plane polarised light (PPL) and cross polarised light (XPL) showing the different mineral assemblages exhibited by rocks from Otjikoto. Image A shows an assemblage of qtz + bio + chl + grn in the garnet amphibole hornfels (OT294). Image B shows an assemblage of qtz + alb + chl in the albitite (OTA234). The amphibole hornfels shows an assemblage qtz + amph + chl in sample OTC323 (Image C). Image D shows an assemblage of qtz + alb + cal + bio in the biotite schist (OT293). In image E and F, the porphyroblastic texture of the amphibole hornfels shows an assemblage of qtz + grn + alb + amph (OT291).

4.3 Ore Petrography

An exsolution texture is illustrated in Figure 4-6 (Image A). An intergrowth pyrrhotite and magnetite is illustrated in Figure 4-6 (Image C). The grey sub-rounded grains are magnetite. Small scale concretionary zoning is visible in sample OTU235, Figure 4-6 (Image D). The bands have an elliptical shape and are present on magnetite. The composition of the banding remains visibly uniform.

In sample OTC232, Figure 4-6 (Image E), grains of magnetite (light grey) are visible. In sample OTC 2310, Figure 4-7 (Image E and F), pyrite is the brightest mineral (visible on the left side of the micrograph). Pyrrhotite is slightly darker than the pyrite. Pyrrhotite exhibits a trellis pattern. Pyrrhotite and pyrite are separated by pore spaces. In sample OTU322, Figure 4-7 (Image A), magnetite occurs as curved platy grains that are stacked together. Pyrrhotite exhibits polygonal grains. In sample OTU234, Figure 4-7 (Image C and D), pyrite occurs in a sheet of disseminated grains. Calcite grains occur within the pyrite.

In sample OTU235, Figure 4-7 (Image B) banded pyrite are visible in the upper left corner of the photo micrograph which forms mineral zoning. In the other corner part, anhedral pyrite and magnetite intergrowths are visible. Some of the open spaces are filled by carbonate minerals. An emulsion texture of magnetite (light grey) is evident in albite, mid-grey. There is an arrangement of exsolution bodies of magnetite in a body of albite. Emulsion textures form as a result of unmixing progressively (Edwards, 1965). Both the solutions in a solid state, simultaneously unmix, within the same ore (Edwards, 1965). This results in an intergrowth of crystals of magnetite and albite. The albite encloses the exsolution crystals of magnetite.

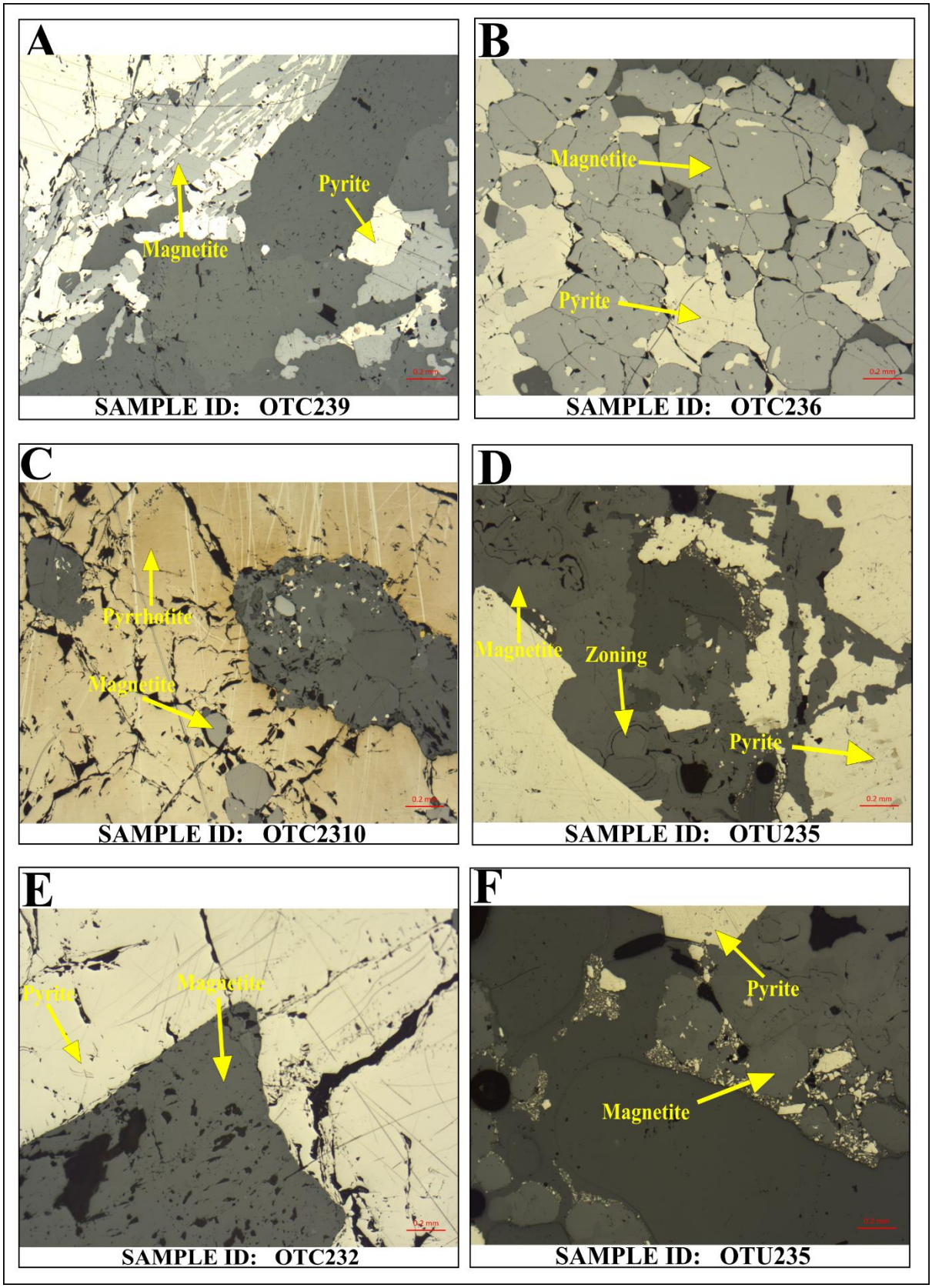

Figure 4-6 Photomicrographs under reflected light showing the different types of ore textures from Otjikoto. Image A displays an exsolution texture with magnetite and pyrite (OTC239). Image B displays intergrowths of pyrite (light) and magnetite (grey) (OTC236). Image C shows an intergrowth of pyrrhotite and magnetite (OTC2310). Image D and F shows small scale concretionary zoning in sample OTU235. Image E shows grains of magnetite (light grey) in sample OTC232.

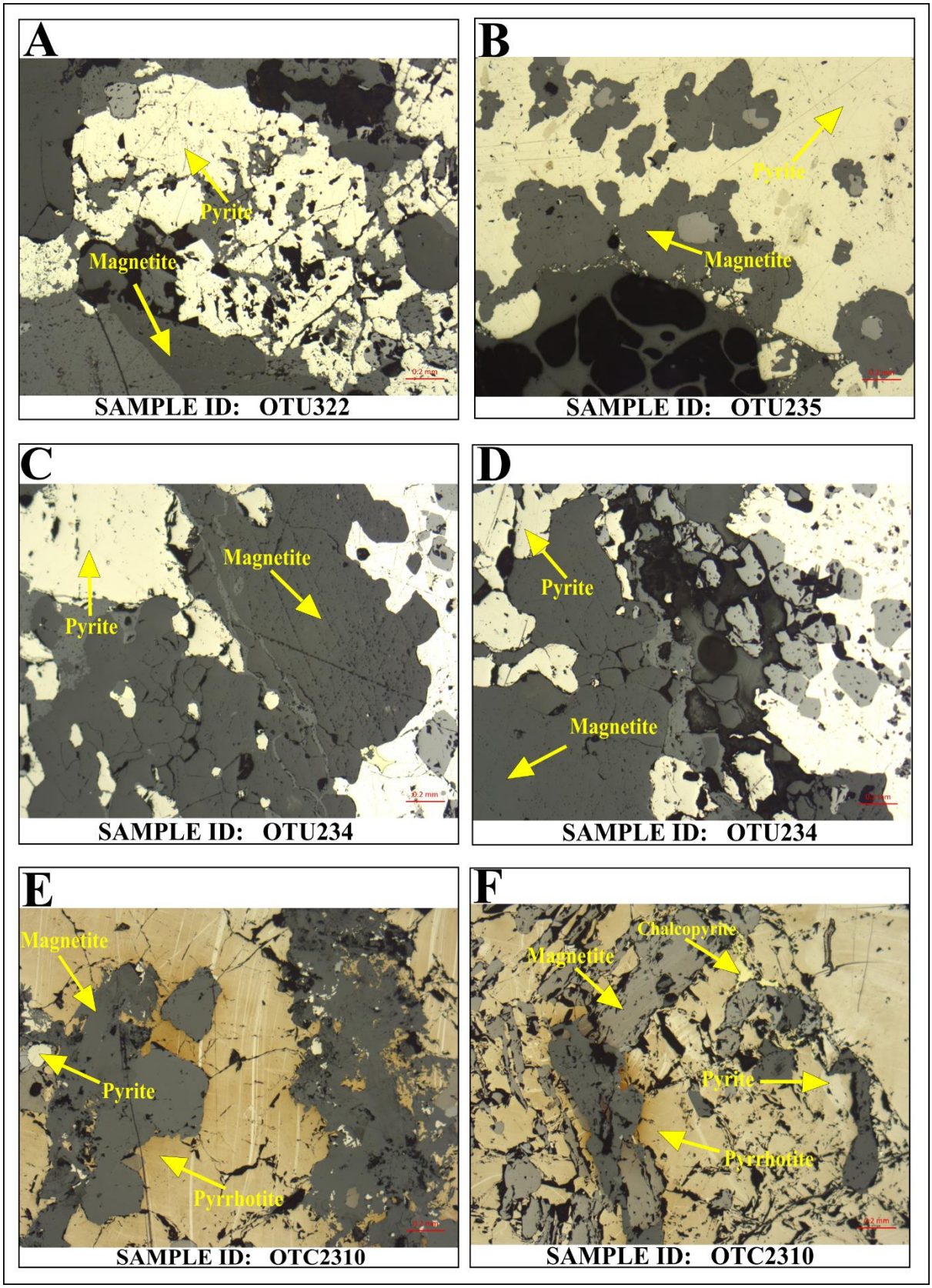

Figure 4-7 Photomicrographs under reflected light showing the different types of ore textures from Otjikoto. Image A displays magnetite which occurs as curved platy grains that are stacked together (OTU322). Image B displays banded pyrite which forms mineral zoning (OTU235). Images C and D shows pyrite which occurs in a sheet of disseminated grains and calcite grains occuring within the pyrite (OTU234). Image D and F shows small scale concretionary zoning in sample OTU235. Image E shows a slightly darker pyrrhotite exhibiting a trellis pattern (OTC2310). Image F shows a texture with pyrrhotite, pyrite, magnetite and chalcopyrite (OTC2310).

Based on the thin section and ore petrography, the paragenetic sequence is shown below.

Table 1 Paragenetic sequence of the minerals from Otjikoto

	EARLY → **LATE**
Quartz	
Albite	
Chlorite	
Calcite	
Amphibole	
Biotite	
Garnet	
Magnetite	
Pyrrhotite	
Chalcopyrite	
Pyrite	
Gold	

5 Results

This section addresses several aims of this study which are to determine the temperature of ore formation by interpreting the temperature of chlorite formation and by interpreting the oxygen isotope fractionation data of quartz and magnetite grains. The mineral chemistry was done on chlorites and amphiboles. The mineral chemistry of the chlorites allows us to calculate the temperatures of chlorite formation. The interpretation of the major and trace element data is also included in this section. The section also looks at the results obtained from fluid inclusion micro-thermometry.

5.1 Mineral Chemistry

5.1.1 Chlorite

Chlorite is a mica like clay mineral that can be found in different geological environments (De Caritat et al., 1993). Chlorite is common in rocks which are diagenetically altered (Inoue et al., 2010). Chlorite can be formed as either a precipitate from fluids or as a replacement mineral which replaces ferro-magnesium minerals (De Caritat et al., 1993). The general formula chlorite is $(Ru^{2+} + Ry^{3+} + Qz)^{vi}(Si_{4-x}Al_x)^{iv}O_{10+w}(OH)_{8-w}$ whereby u+y+z = 6, z = (y-w-x)/z and w is usually a small number or zero (De Caritat et al., 1993). R^{3+} represents Fe^{3+} or Al^{3+} and R^{2+} represents Fe^{2+} or Mg^{2+}. Q represents vacancies. Chlorite has a variable composition as its structure allows substitution to take place (Blumenthal, 2010). The most common substitution in chlorites is the tschermak exchange which is represented by $Mg^{vi}Si^{iv} <=> Al^{vi}Al^{iv}$ (De Caritat et al., 1993). The tschermak exchange results in a charge redistribution between the octahedral and tetrahedral layers, to achieve a charge balance (De Caritat et al., 1993). The chemical composition variation in chlorites allows us to determine the physiochemical conditions during formation of the deposit (Inoue et al., 2010). Chlorite geothermometry is a method of using the chlorite composition to estimate the temperature of formation (Inoue et al., 2010). The crystallization temperature of chlorite may be indicated by 3 types changes namely (1) changes in crystallographic features, (2) changes in the mineral assemblage and (3) changes in chemical composition as solid solutions between end-members (Cathelineau, 1988).

Microprobe analysis of chlorites in the amphibole hornfels and albite biotite schist from Otjikoto are presented in the table 2 below. Chlorite was analysed for the oxides of Ti, Si, Al, Fe, Mn, Mg, Ca, Na and K. The chlorite cations were calculated on a basis of 28 oxygens. When the Fe^{2+} and Fe^{3+} values were calculated, a full occupancy was assumed.

The calculation of Al^{IV} is related to the tschermak exchange between $Mg^{VI}Si^{IV}$ <=>$Al^{VI}Al^{IV}$. There is a redistribution of charges between the tetrahedral and octahedral layers but the overall charge balance must be maintained. The tetrahedral substitution of Si^{4+} by Al^{3+} via the tschermak exchange is accompanied by an equivalent amount of octahedral substitution of R^{2+} Al^{3+} in order to conserve the charge balance. Al^{IV} and Al^{VI} should be equivalent. The value of Al^{VI} in naturally occurring chlorites is greater/smaller than the value of Al^{IV}. If $Al^{VI} > Al^{IV}$ then the octahedral R^{3+} in excess of Al^{IV} may be interpreted as having replaced R^{3+} in a 2:3 ratio. If $Al^{VI} < Al^{IV}$ then the additional octahedral R^{3+}, in the form of Fe^{3+} may be interpreted as having replaced Al^{VI} in a 1:1 ratio. Therefore Al^{IV} is the difference between tetrahedral occupancy and Si^{IV}. If it's greater than 8, then its 8 minus Si.

$$Al^{VI} = Al - Al^{IV} \qquad \text{(equation 5.1)}$$

Table 2 Mineral composition data of chlorites shown as wt. % oxide. The number of ions are shown on the basis of 28 oxygens. XFe and Al^{IV} values were calculated for chlorites analysed in samples OTU322, OTC322 and OTC323. The temperatures of chlorite formation were calculated using the equation by Kranidiotis and MacLean (1987).

Sample ID	**OTU322**	**OTU322**	**OTU322**	**OTU322**	**OTC323**	**OTC323**	**OTC323**	**OTC323**
Analysis ID	**1-C1**	**1-r1**	**2-r1**	**4-C1**	**6-C1**	**7-C1**	**8-C1**	**9-C1**
Type	**Core**	**Rim**	**Rim**	**Core**	**Core**	**Core**	**Core**	**Core**
Oxide wt. %								
SiO2	25.99	25.14	27.01	29.56	28.08	26.88	27.03	26.78
TiO2	0.10	0.04	0.16	0.18	0.01	0.08	0.04	0.21
Al2O3	21.06	20.94	18.37	15.57	19.61	20.77	20.15	20.46
Cr2O3	0.06	0.02	0.00	0.03	0.01	0.01	0.13	0.11
FeO	30.60	31.57	34.27	30.43	23.38	23.21	23.85	24.27
MnO	0.08	0.08	0.09	0.10	0.11	0.06	0.07	0.11
MgO	12.40	11.58	10.29	10.61	18.58	18.14	18.14	17.28
CaO	0.06	0.14	0.10	0.05	0.04	0.03	0.00	0.06
Na2O	0.05	0.05	0.08	0.25	0.06	0.04	0.02	0.16
K2O	0.25	0.00	0.27	3.49	0.00	0.02	0.02	0.02
Totals	**90.65**	**89.56**	**90.64**	**90.26**	**89.88**	**89.24**	**89.46**	**89.45**
Cations								
Oxygens	**28**	**28**	**28**	**28**	**28**	**28**	**28**	**28**
Si	5.43	5.36	5.75	6.17	5.68	5.48	5.52	5.48
Al iv	2.57	2.64	2.25	1.83	2.32	2.52	2.48	2.52
Al vi	2.63	2.62	2.37	2.09	2.36	2.48	2.37	2.42
Ti	0.02	0.01	0.03	0.03	0.00	0.01	0.01	0.03
Cr	0.00	0.00	0.00	0.00	0.00	0.00	0.02	0.02
Fe3+	0.01	0.00	0.05	0.00	0.02	0.00	0.00	0.00
Fe2+	5.34	5.64	6.05	5.51	3.94	3.97	4.11	4.18
Mn	0.01	0.01	0.02	0.02	0.02	0.01	0.01	0.02

Mg	3.86	3.68	3.27	3.30	5.60	5.51	5.52	5.27
Ni	0.00	0.00	0.00	0.00	0.00	0.00	0.00	0.00
Zn	0.00	0.00	0.00	0.00	0.00	0.00	0.00	0.00
Ca	0.01	0.03	0.02	0.01	0.01	0.01	0.00	0.01
Na	0.04	0.04	0.06	0.20	0.04	0.03	0.02	0.13
K	0.13	0.00	0.15	1.86	0.00	0.01	0.01	0.01
Fe/(Fe+Mg)	0.58	0.61	0.65	0.63	0.41	0.42	0.43	0.44
Al^{IV} corrected	2.98	3.07	2.71	2.27	2.61	2.81	2.78	2.83
Temperature/°C	**333.56**	**343.20**	**304.90**	**258.80**	**294.55**	**316.17**	**312.97**	**318.17**

Continued…

Sample ID	OTC322	OTC322	OTC322	OTC322	OTC322	OTC322	OTC322	OTC322
Analysis ID	**1-C2**	**1-R1**	**2-R1**	**3-R1**	**3-C1**	**4-C2**	**4-r1**	**5-C1**
Type	**Core**	**Rim**	**Rim**	**Rim**	**Core**	**Core**	**Rim**	**Core**
Oxide wt. %								
SiO2	27.13	24.81	30.64	32.22	30.64	27.87	30.08	29.23
TiO2	0.09	0.06	0.96	1.17	1.25	0.06	0.39	0.10
Al2O3	20.85	21.89	13.80	15.02	15.47	20.39	19.61	17.81
Cr2O3	0.17	0.15	0.04	0.09	0.11	0.03	0.13	0.06
FeO	25.49	33.74	29.19	25.03	27.44	23.16	20.06	23.99
MnO	0.14	0.26	0.07	0.01	0.06	0.05	0.10	0.04
MgO	15.87	9.88	13.98	15.52	14.06	18.63	18.52	17.76
CaO	0.30	0.05	0.36	0.22	0.28	0.03	0.00	0.16
Na2O	0.05	0.10	0.31	0.29	0.31	0.02	0.08	0.14
K2O	0.60	0.14	0.22	1.83	1.02	0.02	1.77	0.04
Totals	**90.69**	**91.07**	**89.58**	**91.40**	**90.63**	**90.27**	**90.73**	**89.34**
Cations								
Oxygens	**28**	**28**	**28**	**28**	**28**	**28**	**28**	**28**
Si	5.51	5.25	6.39	6.42	6.25	5.60	5.90	5.95
Al iv	2.49	2.75	1.61	1.58	1.75	2.40	2.10	2.05
Al vi	2.52	2.73	1.81	1.99	2.01	2.44	2.49	2.24
Ti	0.01	0.01	0.15	0.18	0.19	0.01	0.06	0.02
Cr	0.03	0.02	0.01	0.01	0.02	0.01	0.02	0.01
Fe3+	0.00	0.00	0.20	0.19	0.20	0.03	0.08	0.10
Fe2+	4.35	5.99	4.89	3.99	4.48	3.86	3.21	3.98
Mn	0.02	0.05	0.01	0.00	0.01	0.01	0.02	0.01
Mg	4.81	3.12	4.35	4.61	4.28	5.58	5.42	5.39
Ni	0.00	0.00	0.00	0.00	0.00	0.00	0.00	0.00
Zn	0.00	0.00	0.00	0.00	0.00	0.00	0.00	0.00
Ca	0.06	0.01	0.08	0.05	0.06	0.01	0.00	0.04
Na	0.04	0.08	0.25	0.23	0.24	0.02	0.06	0.11
K	0.31	0.08	0.12	0.93	0.53	0.01	0.89	0.02
Fe/(Fe+Mg)	0.48	0.66	0.54	0.48	0.52	0.41	0.38	0.43
Al^{IV} corrected	2.82	3.21	1.99	1.91	2.12	2.68	2.36	2.35
Temperature/°C	**317.24**	**358.18**	**228.53**	**220.71**	**242.23**	**302.64**	**268.18**	**267.02**

The chlorites from Otjikoto were subdivided into oxidised and non-oxidised chlorites by using

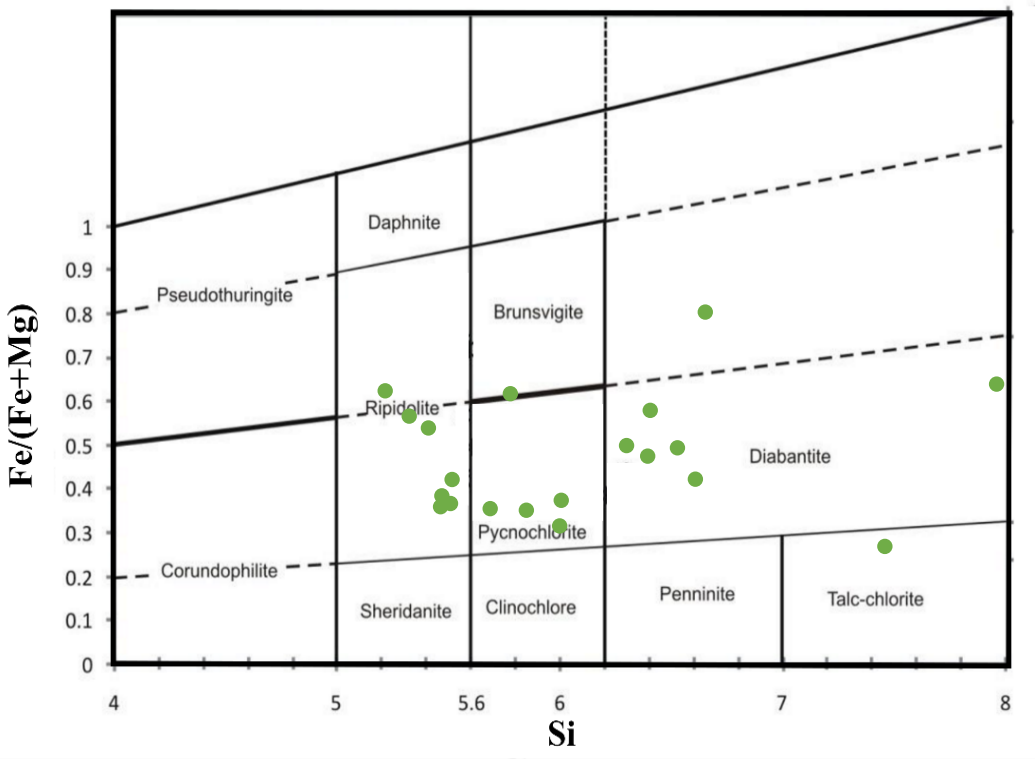

Figure 5-1 Classification of chlorites from Otjikoto based on 28 oxygens (Modified after Hey, 1954).

the chlorite nomenclature diagram by Hey (1954). The majority of the chlorites fall within the ripidolite stability field. Four chlorites fall within the pycnochlorite whereas field whereas 6 chlorites fall within the diabantite field.

Previous studies have showed that there is a relationship between the chemical composition of chlorite and temperature of chlorite formation (Inoue et al., 2010 and Cathelineau, 1988). The equation for calculating temperatures of chlorite formation from Cathelineau (1988) is:

$$T\ (°C) = -61.92 + 321.98\ Al^{iv} \qquad \text{(equation 5.2)}$$

The Al^{3+} in the chlorite's tetrahedral site is directly proportional to the temperature. This relation is expressed by the formula (Kranidiotis & MacLean, 1987):

$$T\ (C^{\circ}) = 106Al^{IV}_{Corrected} + 17.5 \qquad \text{(equation 5.3)}$$

Whereby

$$Al^{IV}corrected = Al^{IV}\ measured + 0.7XFe \qquad \text{(equation 5.4)}$$

Equation 5.3 from Kranidiotis and MacLean (1987) is a revision of the chlorite geothermometry equation by Cathelineau (1988) that takes in account an "Al-saturated

environment" as well as the X_{Fe} that is directly related to the composition of the whole rock (Blumenthal, 2010). Calculations using the equation by Cathelineau (1988) yielded temperatures between 446.80 °C to 823.52 °C which seems too high.

Using equation 5.3, the temperature of formation of the chlorites were calculated to be in the range of 220.71°C to 358.18 °C as shown in Table 2.

5.1.2 Amphibole

Amphiboles are structurally and chemically complex metamorphic minerals (Amiri et al., 2016). The general mineral formula for amphiboles is $\mathbf{AB_2C_5D_8O_{22}X_2}$ whereby A = Na, Ca, Pb, Li, K, B= Ca, Na, Li, Mg, Mn^{2+}, Fe^{2+}, C= Fe^{2+}, $Mn^{2+,}$ Fe^{3+}, Ti^{4+}, Al, Mn^{3+}, D= Si, Ti^{4+}, Al, Be and X= Cl, F, (OH), O^{2-} (Hawthorne et al., 2012). Amphibole minerals from the amphibole hornfels and garnet amphibole hornfels were plotted on the X_{Mg} vs Si ratio classification diagram whereby X_{Mg} is equal to $Mg/(Mg + Fe_{total})$. The Si values range between 7.74 to 7.92 atoms per formula unit (apfu). The X_{Mg} vs Si plot shows that the amphiboles analysed fall within the anthophyllite range. The X_{Mg} values range from 0.49 to 0.57 apfu. The average value for X_{Mg} is 0.54 apfu. Anthophyllite forms from the breakdown of magnesium-rich rocks and as a retrograde product in schists and gneisses. These amphiboles will not be used for geothermobarometric processes. Large amphibole porphyroblasts are present as a result of thermal metamorphism.

Table 3. Mineral composition data of amphiboles shown as wt. % oxide. The number of ions are shown on the basis of 23 oxygens. X_{Mg} values were calculated for amphiboles analysed in samples OTA232 and OTC323.

Sample ID	**OTC323**	**OTC323**	**OTC323**	**OTC323**	**OTC323**	**OTC323**	**OTC323**
Analysis ID	**1-C2**	**1-C3**	**1-C4**	**1-R1**	**1-R2**	**2-R1**	**2-C1**
Type	**Core**	**Core**	**Core**	**Rim**	**Rim**	**Rim**	**Core**
Oxide wt. %							
SiO2	53.90	53.89	55.32	55.34	54.69	54.34	53.83
TiO2	0.07	0.08	0.05	0.05	0.10	0.13	0.01
Al2O3	1.46	1.07	0.54	0.28	0.85	1.46	1.89
Cr2O3	0.04	0.03	0.04	0.05	0.04	0.21	0.10
FeO	25.54	24.45	25.79	25.40	25.77	25.12	25.77
MnO	0.39	0.37	0.47	0.45	0.50	0.41	0.42
MgO	17.05	17.17	17.55	17.93	17.30	17.02	17.28
CaO	1.05	1.53	0.64	0.61	0.38	1.44	0.45
Na2O	0.15	0.13	0.06	0.01	0.08	0.17	0.25
K2O	0.02	0.02	0.00	0.01	0.00	0.02	0.02
Totals	99.68	98.74	100.46	100.11	99.71	100.32	100.00
Cations							
Oxygens	**23**	**23**	**23**	**23**	**23**	**23**	**23**
Tetrahedral site							
Si	7.78	7.83	7.91	7.92	7.89	7.79	7.74
Al iv	0.22	0.17	0.09	0.05	0.11	0.21	0.26
total	**8.00**	**8.00**	**8.00**	**7.97**	**8.00**	**8.00**	**8.00**
Octahedral site							

Al vi	0.03	0.01	0.01	0.00	0.04	0.04	0.06
Ti	0.01	0.01	0.00	0.00	0.01	0.01	0.00
Cr	0.00	0.00	0.00	0.01	0.00	0.02	0.01
Fe3+	0.13	0.10	0.05	0.08	0.03	0.06	0.11
Fe2+	2.95	2.88	3.04	2.96	3.08	2.95	2.99
Mg	3.67	3.72	3.74	3.83	3.72	3.64	3.71
Mn	0.05	0.05	0.06	0.05	0.06	0.05	0.05
total	**6.84**	**6.76**	**6.90**	**6.93**	**6.94**	**6.78**	**6.93**
Alkali Cations							
Ca	0.16	0.24	0.10	0.09	0.06	0.22	0.07
Na	0.04	0.04	0.02	0.00	0.02	0.05	0.07
K	0.00	0.00	0.00	0.00	0.00	0.00	0.00
X_{Mg}	0.54	0.56	0.55	0.56	0.54	0.55	0.54

Continued…

Sample ID	**OTC323**	**OTC323**	**OTC323**	**OTC323**	**OTA232**	**OTA232**	**OTA232**	**OTA232**
Analysis ID	**3-R1**	**3-C1**	**5-C1**	**5-R2**	**1-R1**	**3-R1**	**5-R1**	**1-C1**
Type	**Rim**	**Core**	**Core**	**Rim**	**Rim**	**Rim**	**Rim**	**Core**
Oxide wt. %								
SiO2	54.58	54.84	55.55	55.29	53.71	53.60	53.96	53.32
TiO2	0.08	0.00	0.04	0.01	0.05	0.01	0.04	0.01
Al2O3	0.98	0.98	0.52	0.78	1.05	0.91	0.90	1.13
Cr2O3	0.08	0.06	0.00	0.03	0.04	0.05	0.03	0.02
FeO	24.54	25.32	24.79	24.76	28.77	28.59	28.65	28.31
MnO	0.42	0.42	0.41	0.48	0.38	0.37	0.35	0.32
MgO	17.38	17.56	18.57	18.35	15.61	15.82	15.91	15.64
CaO	1.43	0.89	0.61	0.53	0.74	0.70	0.51	0.94
Na2O	0.11	0.12	0.05	0.08	0.21	0.25	0.19	0.21
K2O	0.01	0.01	0.00	0.01	0.03	0.03	0.01	0.02
Totals	99.62	100.19	100.55	100.32	100.58	100.32	100.55	99.93
Cations								
Oxygens	**23**	**23**	**23**	**23**	**23**	**23**	**23**	**23**
Tetrahedral site								
Si	7.86	7.86	7.89	7.88	7.79	7.79	7.81	7.77
Al iv	0.14	0.14	0.09	0.12	0.18	0.15	0.15	0.19
total	**8.00**	**8.00**	**7.98**	**8.00**	**7.97**	**7.94**	**7.97**	**7.96**
Octahedral site								
Al vi	0.02	0.02	0.00	0.01	0.00	0.00	0.00	0.00
Ti	0.01	0.00	0.00	0.00	0.00	0.00	0.00	0.00
Cr	0.01	0.01	0.00	0.00	0.00	0.01	0.00	0.00
Fe3+	0.06	0.08	0.11	0.08	0.17	0.19	0.15	0.20
Fe2+	2.90	2.95	2.83	2.87	3.32	3.28	3.32	3.25
Mg	3.73	3.75	3.93	3.90	3.37	3.43	3.43	3.40
Mn	0.05	0.05	0.05	0.06	0.05	0.05	0.04	0.04
total	**6.78**	**6.86**	**6.93**	**6.92**	**6.92**	**6.95**	**6.95**	**6.89**
Alkali Cations								
Ca	0.22	0.14	0.09	0.08	0.12	0.11	0.08	0.15
Na	0.03	0.03	0.01	0.02	0.06	0.07	0.05	0.06
K	0.00	0.00	0.00	0.00	0.01	0.01	0.00	0.00
X_{Mg}	0.56	0.55	0.57	0.57	0.49	0.50	0.50	0.50

The amphiboles from Otjikoto were plotted on an amphibole classification diagram from Leake, et al., (2003). Most of the amphoble that were analysed from samples OTA232 and OTC323 plot within the anthophyllite field as shown in *Figure 5-2* below.

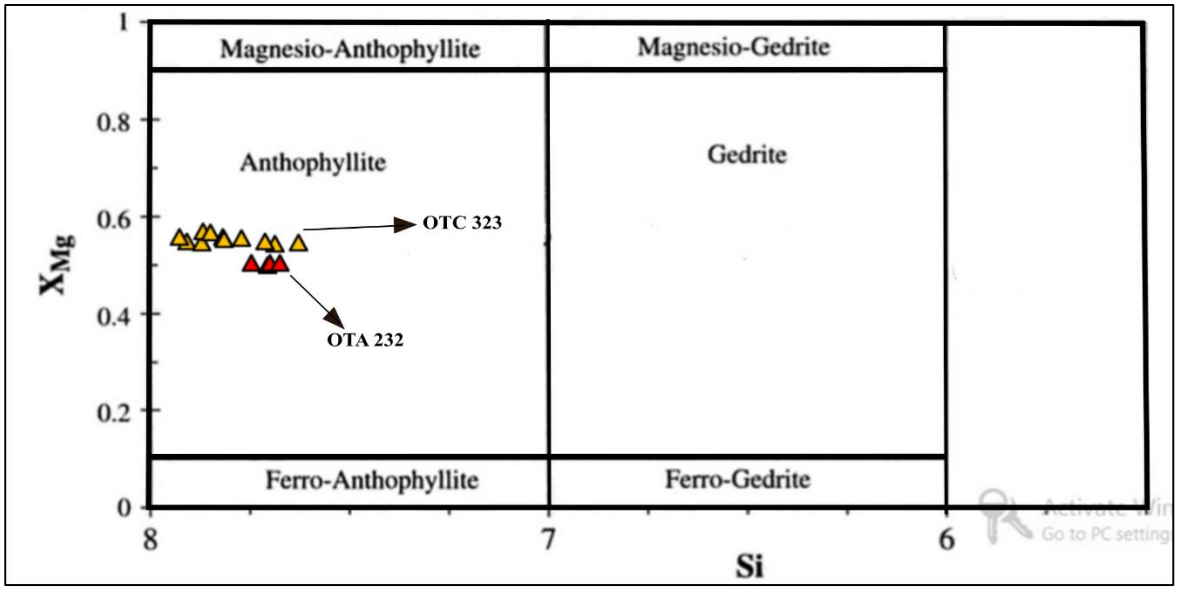

Figure 5-2 Classification of the amphiboles from samples OTA232 and OTC323. The atom amounts are expressed in apfu. (Modified after Leake et al., 2003).

5.2 Geochemistry

In this section, geochemical data for samples from Otjikoto are presented. Whole rock samples of non-mineralised, unaltered and altered rocks, from all the rock units at the Otjikoto gold mine, were analysed for both major and trace elements. The main purpose of the analysis was to characterise the chemical variations of major oxides and to study the nature of the trace elements in the host rocks. For the purpose of obtaining geochemical patterns of the altered and unaltered rocks at Otjikoto, the mineralised rock units were separated from the non-mineralised units. Only the non-mineralised samples were analysed for both major and trace elements. For trace element geochemistry, the plots were separated according to different rock types. An attempt was made to analyse at least one sample of each rock type. Most of the samples analysed are albitites and amphibole hornfels units which also make up the host rock. The entire results are presented in Tables 4 and 5 within this section. Trace elements were analysed by both ICP-MS and XRF analysis methods. Multi-element ICP-MS provides a larger number of trace elements compared to the XRF analysis. This section is subdivided into two parts, namely the major elements section and the trace elements section.

Table 4. Major elements and trace elements of selected samples from Otjikoto obtained by XRF analysis. NM stands for not measured. Values are expressed as wt. %

Sample	**OT-**	**OT-233**	**OT-292**	**OT-294**	**OT-295**	**OT-311**	**OTA-234**	**OTA-3212**
Lithology	Albitite	Amphibole Hornfels	Amphibole Hornfels	Garnet Amphibole Hornfels	Albitite	Biotite Schist	Albitite	Amphibole Hornfels
SiO_2	65.5	60.6	69.4	55.4	81.2	58.6	71.7	60.7
TiO_2	0.86	0.85	0.72	0.90	0.42	0.84	0.60	0.65
Al_2O_3	13.2	15.2	11.3	17.8	7.2	14.6	10.3	12.9
FeO	3.67	5.64	3.94	6.35	2.82	5.14	4.53	4.68
Fe_2O_3	0.61	0.94	0.65	1.05	0.47	0.85	0.75	0.78
MnO	0.15	0.13	0.10	0.14	0.05	0.22	0.09	0.23
MgO	2.41	3.27	3.18	3.93	1.60	4.16	2.20	3.21
CaO	5.91	4.60	4.12	5.87	2.31	7.48	4.00	9.26
Na_2O	7.46	8.57	6.14	8.19	3.62	7.75	5.53	7.32
K_2O	0.04	0.07	0.22	0.09	0.24	0.18	0.09	0.07
P_2O_5	0.23	0.15	0.20	0.25	0.12	0.21	0.16	0.19
Zn	8.41	12.9	10.5	NM	27.1	18.9	8.80	9.63
Cu	<5	<5	<5	NM	<5	5.09	<5	<5
Ni	4.04	12.7	12.6	NM	20.9	19.3	5.87	10.3
Mo	<5	<5	<5	NM	<5	<5	<5	<5
Nb	12.9	10.5	9.00	NM	11.9	10.6	7.7	7.29
Zr	246	173	204	NM	234	203	176	142
Y	46.5	42.4	40.5	NM	46.9	39.4	36.2	32.8
Sr	59.2	52.9	45.8	NM	71.1	82.2	56.4	50.2
Rb	<2	1.53	12.2	NM	21.8	10.6	<2	<2
U	<5	<5	<5	NM	<5	<5	<5	<5
Th	10.6	10.1	8.44	NM	10.6	8.92	6.16	5.93
Pb	<5	4.85	5.63	NM	5.58	4.63	<5	5.04
Co	<5	<5	7.87	NM	<5	<5	<5	<5
Cr	94.3	95.6	71.5	NM	90.3	122	75.0	86.4
V	61.8	188	105	NM	160	254	84.7	109
F	376	502	845	NM	991	790	414	580
S	465	1008	537	NM	283	2608	754	288
Cl	112	110	141	NM	194	115	114	115
Sc	18.0	25.2	15.2	NM	20.5	27.1	20.5	17.5
Ba	28.6	34.8	32.9	NM	96.0	57.3	14.7	13.5

Continued…

Sample ID	**OT-312**	**OT-333**	**OTA-231**	**OTA-232**	**OTB-233**	**OTB-234**	**OTB-3211**	**OTB-322**
Lithology	Amphibole Hornfels	Amphibole Hornfels	Albitite	Amphibole Hornfels	Albitite	Albitite	Albitite	Albitite
SiO_2	54.9	63.4	81.5	81.5	56.0	67.0	67.4	56.0
TiO_2	0.79	0.79	0.38	0.38	0.84	0.79	0.65	0.94
Al_2O_3	14.9	14.5	6.90	6.90	16.0	10.6	12.5	15.9
FeO	5.02	5.89	1.99	1.99	5.14	5.20	4.37	4.74
Fe_2O_3	0.83	0.98	0.33	0.33	0.85	0.86	0.73	0.79
MnO	0.19	0.08	0.07	0.07	0.18	0.19	0.10	0.16
MgO	4.32	3.87	1.33	1.33	3.50	2.60	3.04	3.39
CaO	10.3	2.85	3.39	3.39	8.23	6.46	3.98	8.78
Na_2O	8.54	7.27	4.00	4.00	8.97	6.04	6.99	9.14
K_2O	0.04	0.17	0.03	0.03	0.05	0.06	0.08	0.04
P_2O_5	0.20	0.20	0.08	0.08	0.26	0.19	0.18	0.18
Zn	9.59	17.2	7.65	10.8	8.81	11.9	8.41	10.1
Cu	<5	<5	<5	<5	<5	<5	<5	<5
Ni	9.08	33.8	18.0	19.1	1.37	15.0	3.83	-0.15
Mo	<5	<5	<5	<5	<5	<5	<5	<5
Nb	9.55	10.4	8.87	7.50	9.99	7.47	11.4	6.60
Zr	158	183	162	183	263	157	179	157
Y	36.6	44.2	39.2	36.5	35.7	34.4	39.0	30.6
Sr	56.2	38.9	59.1	55.1	67.5	42.8	51.0	59.1
Rb	<2	9.79	<2	4.74	<2	1.72	<2	<2
U	<5	<5	<5	<5	<5	<5	<5	<5
Th	7.99	9.51	7.73	6.39	8.81	6.42	10.8	7.10
Pb	<5	4.72	4.51	4.69	4.54	4.75	5.20	4.69
Co	6.50	11.0	<5	<5	<5	5.21	<5	<5
Cr	84.9	94.0	79.7	73.6	94.5	76.0	103	68.4

V	141	196	106	95	135	138	158	54
F	398	1075	333	484	455	491	355	358
S	798	541	412	284	978	407	509	796
Cl	116	125	155	134	130	104	124	114
Sc	28.2	24.6	20.3	14.2	16.6	16.4	27.2	14.7
Ba	19.1	43.6	26.5	20.4	22.2	17.9	32.4	9.30

Continued…

Sample	**OTB-231**	**OTB-232**	**OTC-204**	**OTC-231**	**OTC-234**	**OTC-321**	**OTC-322**	**OTC-201**
Lithology	Amphibole Hornfels	Amphibole Hornfels	Amphibole Hornfels	Amphibole Hornfels	Garnet Biotite Schist	Amphibole Hornfels	Amphibole Hornfels	Albitite
SiO_2	55.8	67.3	65.1	67.6	59.0	63.2	59.7	67.2
TiO_2	0.61	0.64	0.78	0.8	0.95	0.91	0.94	0.63
Al_2O_3	11.7	12.1	13.1	11.0	18.0	15.6	15.8	11.4
FeO	7.50	4.51	4.56	3.69	6.33	4.41	4.91	4.44
Fe_2O_3	1.25	0.75	0.76	0.61	1.05	0.73	0.82	0.74
MnO	0.29	0.11	0.17	0.18	0.07	0.09	0.12	0.16
MgO	4.33	2.91	2.33	2.82	4.04	3.35	3.85	2.38
CaO	11.8	4.73	5.57	6.83	2.28	3.81	5.53	6.34
Na_2O	6.59	6.74	7.43	6.25	7.26	7.56	7.89	6.52
K_2O	0.05	0.07	0.04	0.04	0.75	0.09	0.21	0.05
P_2O_5	0.16	0.16	0.19	0.21	0.21	0.27	0.24	0.15
Zn	NM	7.36	6.30	33.8	NM	18.2	NM	7.50
Cu	NM	<5	8.20	7.14	NM	4.75	NM	<5
Ni	NM	12.5	0.30	21.9	NM	7.47	NM	9.58
Mo	NM	<5	<5	<5	NM	<5	NM	<5
Nb	NM	10.5	9.83	12.6	NM	8.74	NM	9.74
Zr	NM	200	254	226	NM	191	NM	187
Y	NM	44.3	35.8	47.0	NM	33.7	NM	36.8
Sr	NM	87.1	61.2	77.2	NM	75.8	NM	57.6
Rb	NM	<2	<2	3.38	NM	4.58	NM	<2
U	NM	<5	<5	<5	NM	<5	NM	<5
Th	NM	9.33	8.88	11.1	NM	7.80	NM	8.85
Pb	NM	<5	<5	4.70	NM	5.23	NM	4.97
Co	NM	5.82	<5	14.92	NM	<5	NM	<5
Cr	NM	95.8	86.4	116	NM	80.2	NM	80.9
V	NM	98.2	72.1	193	NM	144	NM	65.4
F	NM	464	365	697	NM	543	NM	380
S	NM	1021	770	1668	NM	1915	NM	594
Cl	NM	118	105	101	NM	104.5	NM	117
Sc	NM	27.0	15.4	22.8	NM	20.2	NM	19.2
Ba	NM	21.4	17.6	34.3	NM	27.3	NM	24.6

Continued…

Sample ID	**OTC-323**	**OTC-324**	**OTC-331**	**OTC-3332**	**OTU-231**	**OTU-234**	**OTU-322**
Lithology	Amphibole Hornfels	Garnet Biotite Schist	Amphibole Hornfels	Amphibole Hornfels	Banded Amphibole Hornfels	Albitite	Albite Biotite Schist
SiO_2	58.7	79.6	66.6	58.2	70.6	59.6	67.6
TiO_2	1.08	0.45	0.71	0.98	0.60	0.85	0.64
Al_2O_3	17.4	9.05	12.0	18.3	11.4	16.1	12.3
FeO	5.30	3.09	3.81	6.92	3.64	7.08	4.92
Fe_2O_3	0.88	0.51	0.63	1.15	0.60	1.18	0.82
MnO	0.11	0.03	0.18	0.08	0.08	0.06	0.09
MgO	3.69	1.93	3.14	4.21	2.71	5.24	3.06
CaO	4.27	1.10	6.24	2.18	3.90	2.55	3.95
Na_2O	7.89	3.74	6.40	6.97	6.10	6.20	6.44
K_2O	0.38	0.38	0.09	0.82	0.13	0.85	0.10
P_2O_5	0.28	0.11	0.18	0.21	0.16	0.32	0.16
Zn	NM	37.3	13.7	29.0	14.0	33.2	8.70
Cu	NM	<5	<5	<5	49.9	3.40	50.0
Ni	NM	31.3	16.2	14.9	10.8	30.8	16.6
Mo	NM	<5	<5	<5	<5	<5	<5
Nb	NM	12.8	7.41	8.01	6.36	12.2	7.82
Zr	NM	202	153	169	133	205	155

Y	NM	45.6	35.1	36.4	35.3	45.0	30.6
Sr	NM	96.2	48.4	52.1	65.1	98.1	39.2
Rb	NM	39.2	7.28	5.53	<2	37.0	51.8
U	NM	<5	<5	<5	<5	<5	<5
Th	NM	11.8	6.72	7.68	7.74	11.7	6.39
Pb	NM	<5	4.55	<5	5.11	<5	<5
Co	NM	11.6	<5	<5	8.42	10.1	5.88
Cr	NM	143	77	81	77	132	86
V	NM	245	112	115	85	233	113
F	NM	1631	624	702	716	1189	735
S	NM	878	339	292	6568	903	508
Cl	NM	114	119	111	114	111	170
Sc	NM	24.5	16.2	18.8	19.5	23.1	15.1
Ba	NM	247	23.3	24.2	<5	239	198

Table 5 Trace elements of selected samples from Otjikoto obtained by ICP-MS analysis. Values are expressed in ppm.

Sample	**OT233**	**OT292**	**OT294**	**OT311**	**OT312**	**OT333**	**OTB232**	**OTB233**
Rock Type	Amphibole Hornfels	Amphibole Hornfels	Garnet Amphibole Hornfels	Amphibole Hornfels	Albitite	Amphibole Hornfels	Amphibole Hornfels	Albitite
Sc	20.9	17.1	21.8	20.3	15.5	19.6	24.2	13.0
V	183	128	246	222	117	202	119	288
Cr	108	80.6	113	105	81.2	132	112	56.9
Co	11.2	30.6	12.2	9.38	7.07	12.2	33.7	8.32
Ni	54.8	48.3	71.5	42.4	27.6	167	151	22.7
Cu	38.9	59.0	65.9	110	496	370	163	48.2
Zn	19.6	17.4	22.8	24.7	7.81	19.3	13.2	9.6
Rb	0.38	16.7	2.01	4.69	0.14	7.23	0.18	0.14
Sr	65.6	50.0	61.9	104	44.8	46.1	120	67.3
Y	34.0	35.2	37.4	39.2	24.7	34.5	41.7	18.0
Zr	157	223	177	223	128	174	248	167
Nb	12.2	11.3	13.7	14.3	9.8	12.0	14.9	7.6
Mo	0.65	0.80	0.97	0.56	0.66	1.19	1.31	0.58
Cs	0.09	2.05	0.67	0.56	0.00	0.99	Below	0.00
Ba	17.4	33.8	22.9	26.5	13.2	25.5	16.8	11.6
La	34.6	31.3	37.1	38.4	24.1	36.1	48.5	16.6
Ce	68.7	65.3	73.6	76.9	47.4	72.8	93.5	33.4
Pr	8.20	7.90	9.07	9.16	5.75	8.66	11.04	4.25
Nd	32.6	32.9	35.9	37.1	23.4	33.7	44.1	16.8
Sm	7.17	6.59	7.65	7.95	5.20	6.89	9.14	3.57
Eu	1.48	1.18	1.46	1.59	0.96	1.22	2.08	0.86
Gd	6.44	6.50	7.05	7.23	4.57	6.65	9.65	3.74
Tb	0.98	0.85	1.06	1.21	0.71	1.02	1.29	0.59
Dy	6.06	6.01	7.26	6.71	4.69	6.53	7.93	3.50
Ho	1.15	1.24	1.50	1.43	0.89	1.37	1.52	0.60
Er	3.74	3.77	3.88	4.08	2.91	3.54	4.50	1.83
Tm	0.47	0.53	0.57	0.60	0.32	0.53	0.63	0.30
Yb	3.40	3.45	3.68	4.12	2.49	3.58	3.92	1.85
Lu	0.49	0.46	0.61	0.58	0.40	0.49	0.60	0.29
Hf	4.65	5.97	4.92	6.13	3.95	5.20	7.44	4.66
Ta	0.82	0.80	0.85	1.04	0.66	0.87	1.03	0.47
Pb	1.64	1.29	1.59	1.87	0.83	1.41	1.35	0.89
Th	9.18	9.09	12.2	10.8	7.32	9.33	11.7	5.06
U	3.94	3.64	5.35	3.99	3.20	4.33	4.91	2.19

Continued…

Sample	**OTA232**	**OTA234**	**OTA3212**	**OTB231**	**OTC201**	**OTC204**	**OTC231**	**OTC234**
Rock Type	Amphibole Hornfels	Albitite	Amphibole Hornfels	Albitite	Albitite	Albitite	Amphibole Hornfels	Biotite Schist
Sc	15.0	16.4	12.4	19.6	17.3	12.9	17.2	24.8
V	118	110	111	79.1	56.6	96.0	145	251
Cr	81.6	93.3	68.0	61.2	89.0	65.2	107	120
Co	9.52	2.46	2.80	10.9	6.65	5.26	24.8	11.6
Ni	53.0	35.4	30.1	28.0	50.2	31.8	57.2	57.4
Cu	85.1	38.9	29.0	26.0	52.7	96.5	174	26.7
Zn	265	11.0	16.1	9.78	61.2	8.60	30.5	37.7
Rb	3.31	0.20	0.92	0.00	0.00	6.37	0.44	35.5

Sr	74.9	80.2	51.5	67.6	71.9	50.1	102	97.8
Y	31.2	33.5	23.2	18.2	33.2	25.5	37.2	36.9
Zr	204	212	135	97.7	183	161	219	178
Nb	10.0	12.2	9.59	7.52	16.7	8.37	14.5	14.3
Mo	1.77	0.92	0.57	0.63	0.73	0.54	2.01	0.87
Cs	0.43	0.00	0.25	0.00	0.00	0.47	0.09	3.75
Ba	25.4	20.3	14.2	12.7	16.1	31.7	17.9	181
La	27.8	33.1	20.8	16.4	25.8	25.7	34.6	36.7
Ce	56.7	68.4	43.7	34.0	53.8	53.7	72.5	74.9
Pr	7.12	8.22	5.17	4.13	6.76	6.39	9.20	9.06
Nd	27.1	32.6	21.5	16.0	26.6	25.1	35.7	34.7
Sm	6.21	6.75	3.82	4.14	5.53	4.31	7.07	7.44
Eu	0.95	1.19	0.82	0.85	1.13	0.82	1.43	1.40
Gd	5.76	6.38	4.51	3.87	4.86	4.86	7.01	7.30
Tb	0.95	0.97	0.61	0.53	0.84	0.76	1.10	1.00
Dy	5.64	6.12	3.88	3.18	5.87	4.84	6.73	7.00
Ho	1.18	1.23	0.87	0.73	1.21	0.95	1.26	1.39
Er	3.49	3.78	2.29	2.19	3.51	2.89	4.15	3.78
Tm	0.49	0.52	0.34	0.31	0.43	0.43	0.59	0.53
Yb	3.21	3.08	2.10	2.01	3.22	2.16	3.40	3.94
Lu	0.54	0.57	0.31	0.31	0.43	0.36	0.62	0.54
Hf	5.14	6.42	3.78	2.74	5.29	4.10	5.97	5.27
Ta	0.72	0.86	0.61	0.50	0.81	0.59	0.97	0.96
Pb	2.53	0.98	1.05	1.24	2.08	0.78	1.22	1.74
Th	7.92	9.63	6.76	5.07	8.31	7.48	11.3	11.8
U	3.06	5.24	2.63	2.41	3.62	3.36	4.21	5.01

Continued…

Sample	**OTC321**	**OTC324**	**OTC331**	**OTC3332**	**OTU231**	**OTU322**	**OTB234**	**OTB321**
Rock Type	Amphibole Hornfels	Garnet Biotite Schist	Amphibole Hornfels	Amphibole Hornfels	Amphibole Hornfels	Biotite Schist	Amphibole Hornfels	Albitite
Sc	13.4	30.9	12.5	12.0	21.4	11.5	17.8	18.4
V	141	334	114	99.4	248	93.8	163	135
Cr	66.5	161	64.5	58.9	152	72.5	85.9	89.6
Co	2.90	16.8	7.71	6.92	7.63	11.6	9.31	8.80
Ni	40.1	81.3	45.7	38.5	60.6	46.0	47.0	27.9
Cu	32.0	38.9	39.1	26.4	58.9	97.4	18.3	18.6
Zn	25.7	55.5	16.4	27.3	53.5	11.9	17.8	12.1
Rb	5.00	48.1	5.59	3.06	Below	48.9	3.13	0.13
Sr	70.7	131	51.0	46.9	107	41.1	53.1	54.9
Y	29.1	47.7	24.3	23.8	37.9	24.8	30.4	28.5
Zr	162	245	142	146	213	165	167	150
Nb	9.30	17.7	8.74	7.89	23.1	8.44	10.73	11.45
Mo	0.74	0.59	0.72	0.68	0.98	1.31	0.57	0.65
Cs	0.72	5.09	1.02	0.45	Below	0.84	0.54	0.00
Ba	24.6	251	18.5	26.2	16.0	146	17.4	13.3
La	23.0	47.0	20.7	19.8	39.2	21.0	27.5	26.3
Ce	47.2	96.9	43.4	42.0	77.3	44.5	55.9	55.2
Pr	5.81	11.9	5.32	5.29	9.32	5.58	6.76	6.81
Nd	23.4	45.9	21.2	20.2	36.3	22.4	26.4	25.9
Sm	5.16	9.08	4.37	4.62	7.37	5.47	5.88	4.70
Eu	0.97	1.64	0.77	0.76	1.62	0.93	0.99	1.06
Gd	4.86	10.1	4.92	4.17	7.49	4.30	5.77	4.79
Tb	0.74	1.29	0.70	0.64	1.02	0.66	0.91	0.79
Dy	5.19	8.73	4.18	4.30	6.39	4.18	5.51	5.23
Ho	1.13	1.74	0.87	0.83	1.34	0.94	0.98	1.01
Er	3.20	5.04	2.57	2.69	4.01	2.89	3.32	2.86
Tm	0.41	0.78	0.47	0.34	0.64	0.37	0.51	0.47
Yb	2.79	5.07	2.66	2.23	4.12	2.34	2.96	3.01
Lu	0.45	0.71	0.36	0.34	0.66	0.34	0.43	0.46
Hf	4.48	6.93	4.24	3.87	5.63	4.41	4.54	3.79
Ta	0.64	1.31	0.59	0.57	1.19	0.54	0.74	0.79
Pb	1.22	2.15	1.15	0.87	3.37	1.14	1.32	1.20
Th	7.10	15.9	6.35	6.38	13.3	6.24	9.14	8.44
U	2.42	7.41	2.74	2.51	6.07	1.62	4.30	3.95

5.2.1 Major Elements

For this study, major elements were analysed in order to characterise the whole rock geochemistry rocks from Otjikoto. The albitites from Otjikoto, which are the main host rocks, exhibit a wide range of silica (46.70-57.36 wt. %), alkali (Na_2O: 5.51-7.15 wt. % and K_2O: 0.04-0.43wt. %), alumina (Al_2O_3 of 9.76-13.23 wt. %) and iron content (4.58 to 8.02 wt. %) of Fe_2O_3. The high sodium content is probably due to the presence of albite.

The samples for Otjikoto were plotted on major oxide vs silica plots. The TiO_2 vs SiO_2 diagram shows a negative correlation for the rock samples (Figure 5-3). As the TiO_2 content decreases, the SiO_2 content increases. The TiO_2 content for the albitites ranges from 0.4 to 0.9 wt. %. The amphibole hornfels shows the lowest TiO_2 content of 0.28 wt. % and the highest TiO_2 content of 1.1 wt. %. The Al_2O_3 vs SiO_2 diagram exhibits a slight negative correlation for the Otjikoto rock samples (Figure 5-3). The alumina content increases with decreases amount of silica. The alumina content for the albitites ranges between 7 and 16 wt. %. The amphibole hornfels shows the highest alumina content of 18.1 wt. % whereas the albitite sample shows the lowest alumina content of 6.2 wt. %. The samples from Otjikoto also show a slight negative correlation on the MgO vs SiO_2 diagram. Silica enrichment increases as the MgO content decreases. The MgO content in the samples ranges between 1 and 5.2 wt. %. The MgO content of the albitites ranges from 1 to 5.2 wt. %. The MgO content of the amphibole hornfels is within a narrow range, between 2.2 to 4.2 wt. %. The banded amphibole hornfels has an MgO content of 2.6 wt. %.

The CaO vs SiO_2 shows a minor negative correlation between the CaO and SiO_2 (Figure 5-3). Some of the samples are scattered within the plot. The calcium oxide values range between 2 and 12.1 wt. %. The albitite has the highest calcium content of 12.1 wt. % with a silica content of 55.8 wt. %. The garnet biotite schist has the lowest CaO content of 2 wt. % at a silica content of 80 wt. %. The Na_2O vs SiO_2 plot of the Otjikoto samples shows a negative correlation (Figure 5-3). The albitite shows the highest Na_2O content of 9 wt. % at 56.2 wt. % of SiO2, which may be attributed to the abundance of the sodium rich feldspar (albite) in the rock unit. The Na_2O values range between 3.2 and 9 wt. %. The biotite schist has a Na2O content of 7.8 wt. %. The banded amphibole hornfels has a Na_2O content of 6 wt. % at 71 wt. % SiO_2.

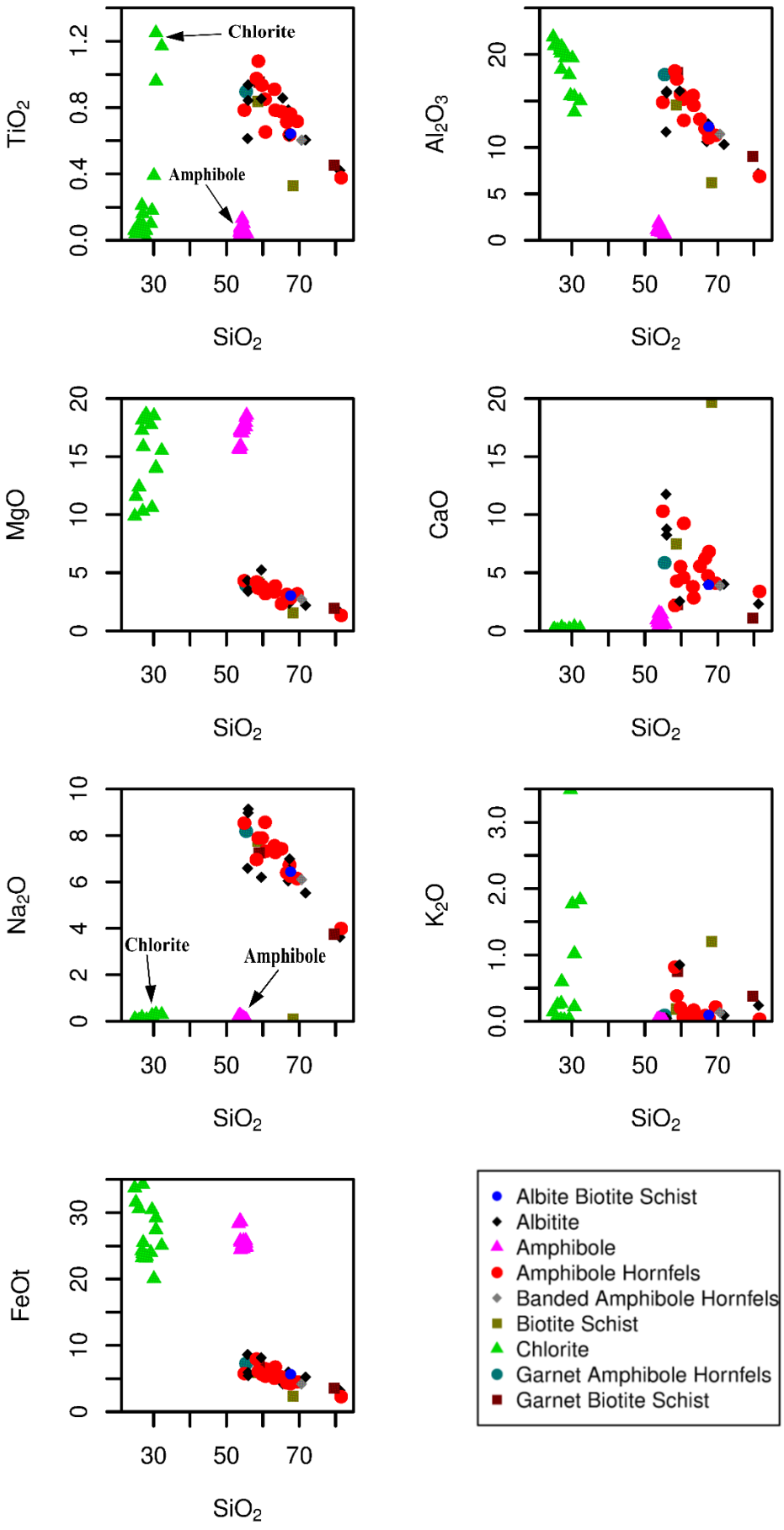

Figure 5-3 Harker diagram for selected major element oxides vs. Silica for analysed Otjikoto rock samples and minerals. The major oxides for the rock samples were analysed by XRF whereas the major oxides for the chlorite and amphibole were obtained by electron microprobe analysis.

The K_2O vs. SiO_2 diagram for the Otjikoto samples shows a scattered pattern with no correlation (Figure 5-3). Most of the albitites have a low potassium oxide content ranging from 0.01 to 0.23 wt. %. The K_2O content of the amphibole hornfels ranges from 0.1 – 0.81 wt. %. The total FeO vs silica diagram shows a slight negative correlation whereby the silica content increases as the FeOt content decreases (Figure 5-3). The FeOt values range between 2 wt. % and 9 wt. %. The albitite samples have the lowest and highest FeOt content of 2 wt. % and 9 wt. % respectively.

The chlorite and amphibole minerals from samples OTC 323, OTA 232, OTC 322 and OTU 322 were also plotted on the major oxide vs silica variation diagrams to show how samples vary in terms of the minerals they might contain (Figure 5-3). The TiO_2 vs SiO_2 diagram does not show any correlation for the amphibole and chlorite minerals plotted. The TiO_2 content ranges from 0.01 to 1.25 wt. % for the chlorite and from 0.01 to 0.13 wt. % for the amphiboles. The Al_2O_3 vs SiO_2 diagram shows a slight negative correlation for chlorites and no correlation for amphiboles. The Al_2O_3 content ranges from 13.80 to 21.89 wt. % for the chlorites and from 0.28 to 1.89 wt. % for the amphibole mineral. The MgO vs SiO_2 diagram does not show any correlation for the amphibole and chlorites. The MgO content ranges from 9.88 to 18.63 wt. % for chlorites and from 15.61 to 17.93 wt. % for amphiboles. The CaO vs SiO_2 diagram does not exhibit any correlation for the chlorite and amphibole mineral. The CaO content ranges from 0.03 to 0.36 wt. % for chlorites and from 0.38 to 1.44 wt. % for the amphiboles. The Na_2O vs SiO_2 diagram does not show any correlation for chlorite and amphibole. The small Na_2O content ranges from 0.02 to 0.31 wt. % for chlorites and from 0.01 to 0.25 wt. % for amphiboles. The K_2O vs SiO_2 diagram shows a minor positive correlation for chlorite and no correlation for amphiboles (Figure 5-3). The K2O content ranges from 0.02 to 1.83 wt. % for chlorites and from 0.01 to 0.03 wt. % for amphiboles. The FeOt vs SiO_2 diagram shows a slight negative correlation for both the chlorites and amphiboles. The FeOt content ranges from 20.06 to 34.27 wt. % for chlorite and from 24.45 to 28.77 wt. % for amphiboles.

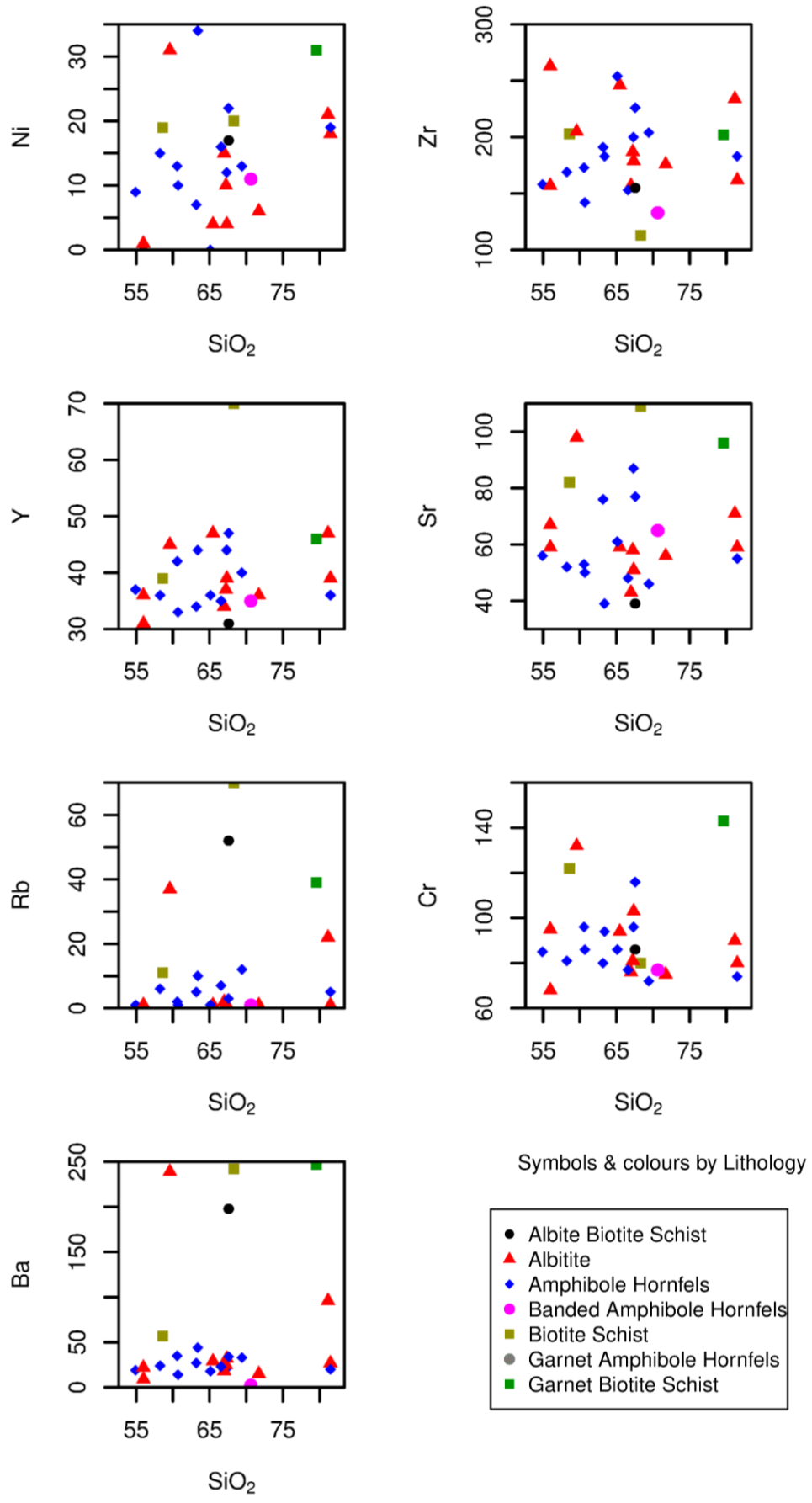

Figure 5-4 Variation diagrams for selected trace elements vs. silica for analysed Otjikoto rock samples. Ni, Zr, Y, Sr, Rb, Cr and Ba were analysed by using XRF analysis.

The samples from Otjikoto were plotted on the trace element vs. SiO_2 variation diagrams. The variation diagrams were plotted by using the trace element data obtain from XRF analysis. The Ni content slightly increases as the silica content increases (Figure 5-4). The Ni values range between zero and 34 ppm. The amphibole hornfels shows the lowest and highest Ni content of 0 and 34 ppm respectively.

The Zr vs. SiO_2 diagram does not show any correlation for the samples plotted (Figure 5-4). The Zr content of the albitites ranges between 157 and 246 ppm. The albitite shows the highest Zr content of 246 ppm. The lowest Zr content of 133 ppm is exhibited by the banded amphibole hornfels. The Y vs. SiO_2 diagram shows a minor positive correlation whereby the Y content slightly increases with silica enrichment in the rocks (Figure 5-4). The Y content in the rocks narrowly ranges from 31 ppm to 47 ppm. Both the albitite and amphibole hornfels exhibit the highest Y content of 47 ppm. The Sr vs. SiO_2 diagram does not show any correlation between the element Sr and the silica content in the rocks. Most of the samples appear to be scattered on the plot (Figure 5-4). The Sr content ranges from 31 ppm in the albite biotite schist to 98 ppm in the albitite.

The Rb vs. SiO_2 diagram does not exhibit any correlation between the element Rb and the silica content (Figure 5-4). Most of the samples are depleted in Rb with most of the samples showing an Rb content of less than 15 ppm. The Cr vs SiO_2 diagram shows a minor negative correlation. The amount of Cr slightly decreases as the silica content increases (Figure 5-4). The Cr content ranges from 63 ppm in the albitite to 141 ppm in the garnet biotite schist. Most of the rocks have a Cr content of less than 100 ppm. The Ba vs. SiO_2 diagram does not show any correlation (Figure 5-4). The Ba values range from 0 to a peak value of 252 ppm in the garnet biotite schist. Most of the samples are depleted in Ba showing values of less than 50 ppm.

5.2.2 Trace Elements

Twenty-four samples from Otjikoto were plotted on the trace element vs. Zr variation diagrams as shown in Figure 5-5 below. The diagrams were plotted using the data obtained by LA-ICP-MS.

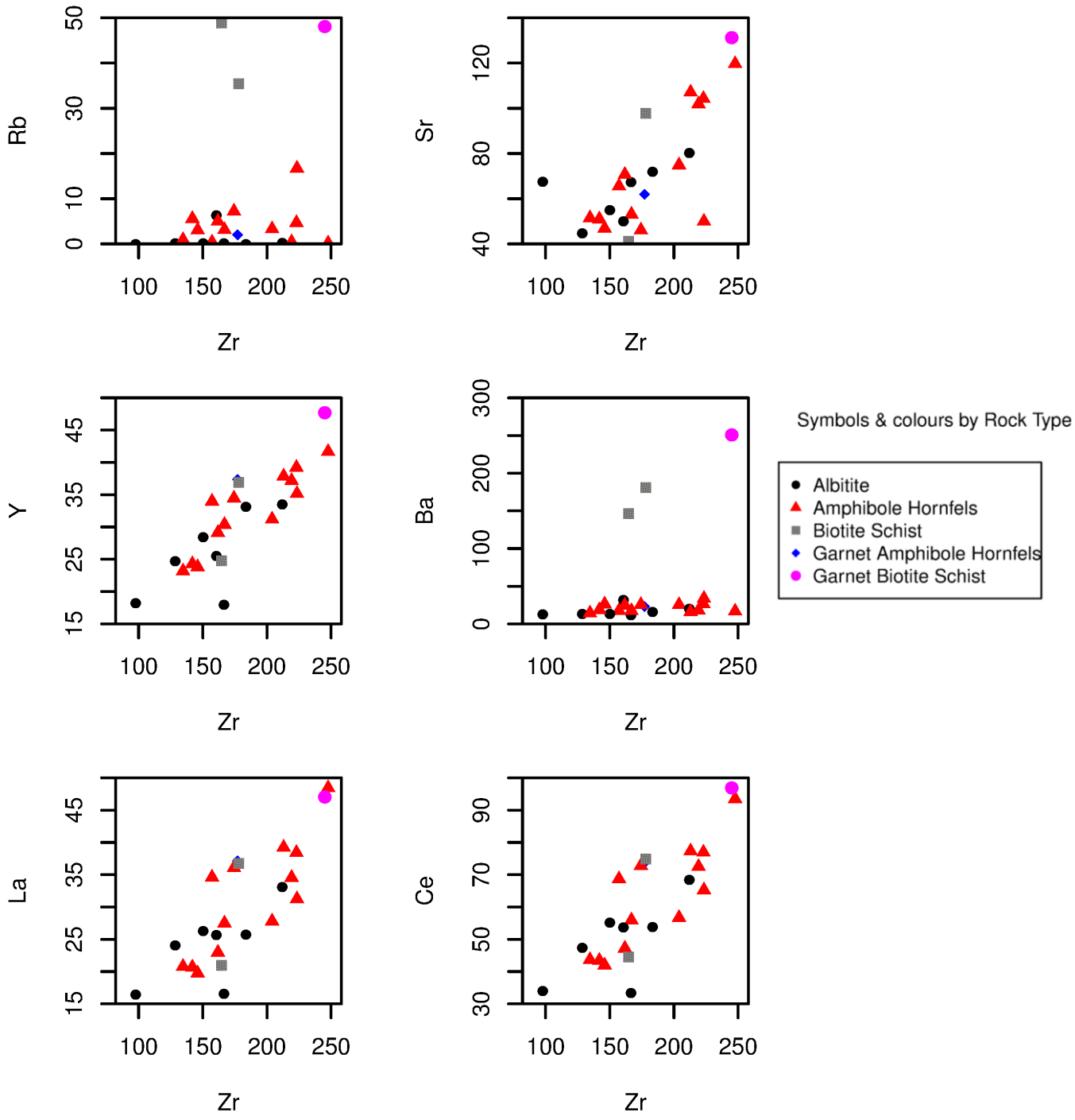

Figure 5-5 Variation diagrams for selected trace elements vs. Zr for analysed Otjikoto rock samples. Rb, Sr, Y, Ba, La and Ce were analysed by ICP-Ms analysis.

The samples on the Rb vs. Zr diagram appear to be scattered (Figure 5-5). There is no correlation between the two elements. The Rb content ranges from zero to 50 ppm in the biotite schist. Most of the rocks are depleted in Rb with contents below 10 ppm. The garnet

biotite schist also shows a high Rb content with a value of 49 ppm. The Sr vs. Zr diagram shows a strong positive correlation (Figure 5-5). The Sr content increases as the rocks are enriched with Zr. The biotite schist shows the lowest Sr content with a value of 40 ppm. The garnet biotite schist exhibits the highest Sr content with a value of 130 ppm. The Y vs. Zr diagram also shows a strong positive correlation between the two elements. The Y content increases as the rocks are enriched with Zr. The albitite has the lowest Y content of 17 ppm whereas the garnet biotite schist has the highest with a value of 47 ppm. The Ba vs. Zr diagram does not show any correlation. The biotite schist and the garnet biotite schists are enriched with Ba showing values of 148 and 250 ppm respectively. All the other samples are depleted in Ba with contents of less than 40 ppm. The La vs. Zr diagram shows a strong positive correlation between La and Zr (Figure 5-5). The albitite shows the lowest La content with a value of 17 ppm. The amphibole hornfels shows the highest La content with a value of 48 ppm. The garnet biotite schist also exhibits a fairly high content with a value of 43 ppm. The Ce vs. Zr diagram shows a positive correlation. The Ce content increases as the rocks are enriched with zircon. The garnet biotite schist has the highest Ce value of 94 ppm. The albitite has the lowest Ce content with a value of 34 ppm.

The rare earth elements (REE) of samples from Otjikoto have been normalised using chondrite meteorite values (McDonough & Sun, 1995). Most of the albitites have similar REE patterns (Figure 5-6) with a negative Eu anomaly. This may imply that during fractional crystallization of plagioclase, the magma was reduced during upward movement and lost Eu. All the albitites are enriched in light rare earth elements (LREE) in comparison to the heavy rare earth elements (HREE).

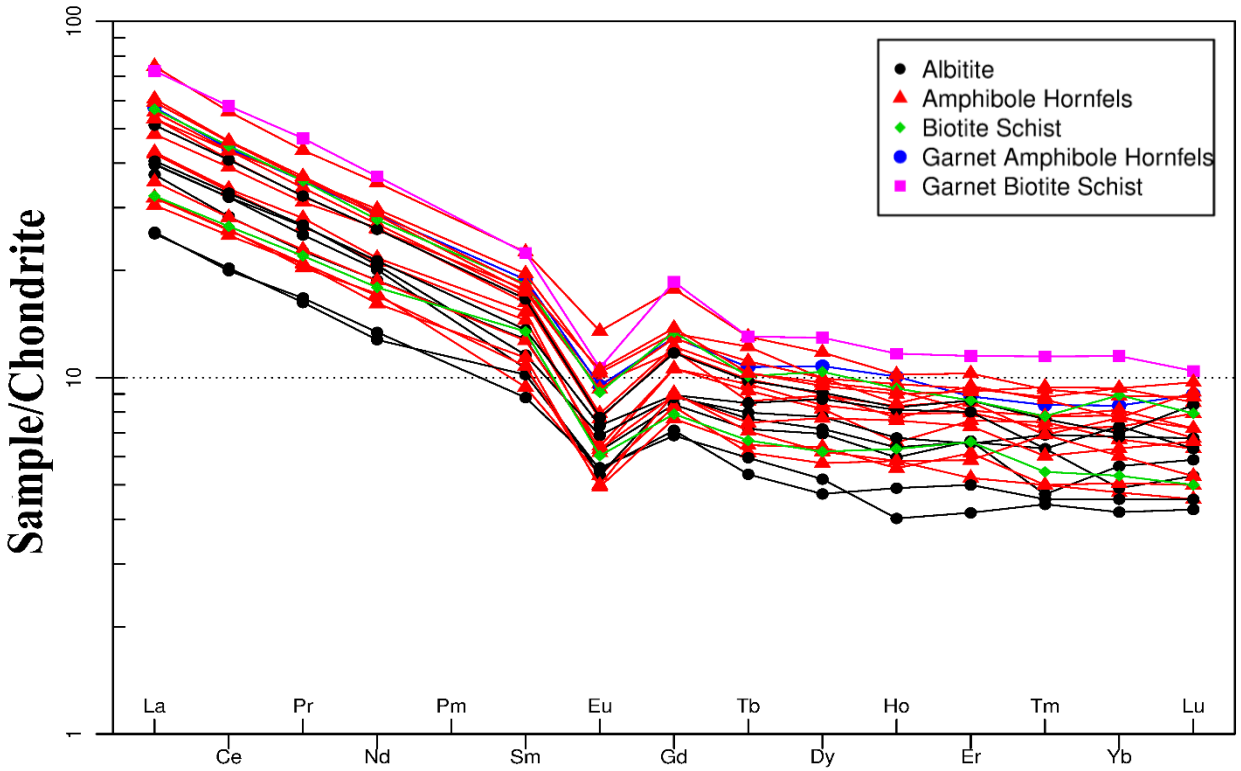

Figure 5-6 Spider plot showing chondrite normalised REE patterns for samples from Otjikoto. The chondrite values were taken from McDonough and Sun (1995).

The banded amphibole hornfels, amphibole hornfels and garnet amphibole hornfels all show similar REE patterns (Figure 5-6). All of the amphibole hornfels show a moderate negative Eu anomaly. All of the samples are enriched with LREE in comparison to the HREE concentrations. The banded amphibole hornfels and the garnet amphibole hornfels show a higher LREE and HREE concentrations in comparison to the rest of the amphibole hornfels samples. The HREE pattern of most of the samples is almost flat. The garnet biotite schist and biotite schist have similar REE concentrations and patterns (Figure 5-6). The garnet biotite schist and biotite schist are enriched in LREE compared to the HREE concentrations. The samples have a moderately negative Eu anomaly. The HREE pattern of the biotite schists and garnet biotite schist are relatively flat. The garnet biotite schist has a higher LREE and HREE concentration.

5.3 Fluid Inclusion Study

Double-polished fluid inclusion wafers were prepared for two samples from the Otjikoto gold mine, namely OTC 239 and OTU 322 as shown in Figure 5-7 and Figure 5-8. The two samples are from mineralised quartz veins of the main ore zone, which consists of albitites and amphibole hornfels (Figure 5-7 and Figure 5-8). When studying fluid inclusions, two assumptions have to be made. The first assumption is that the volume of the inclusion will not change, i.e. isochoric, from the time it was entrapped (Reynolds et al., 1994). The second assumption is that a fluid inclusion will remain chemically closed from the time it was entrapped, i.e. isoplethic (Reynolds et al., 1994). The fluid inclusions were identified as being either primary (isolated or cluster) or secondary (trails) inclusions. The volumetric proportions of the liquid to vapour ratios, were estimated petrographically by using the diagram by Roedder (1972). Before petrographic studies were undertaken, the field conditions and the geological framework had to be considered (Reynolds et al., 1994). Most of the fluid inclusions observed in samples OTC239 and OTU322 are of secondary origin. Some of the secondary inclusions are hosted within microstructures. The fluid inclusions were noted as either LV, LVS or V based on the phases observed at room temperature. Primary inclusions (isolated) are present in both samples. The isolated inclusions are visibly larger than the secondary inclusions that were found in trails.

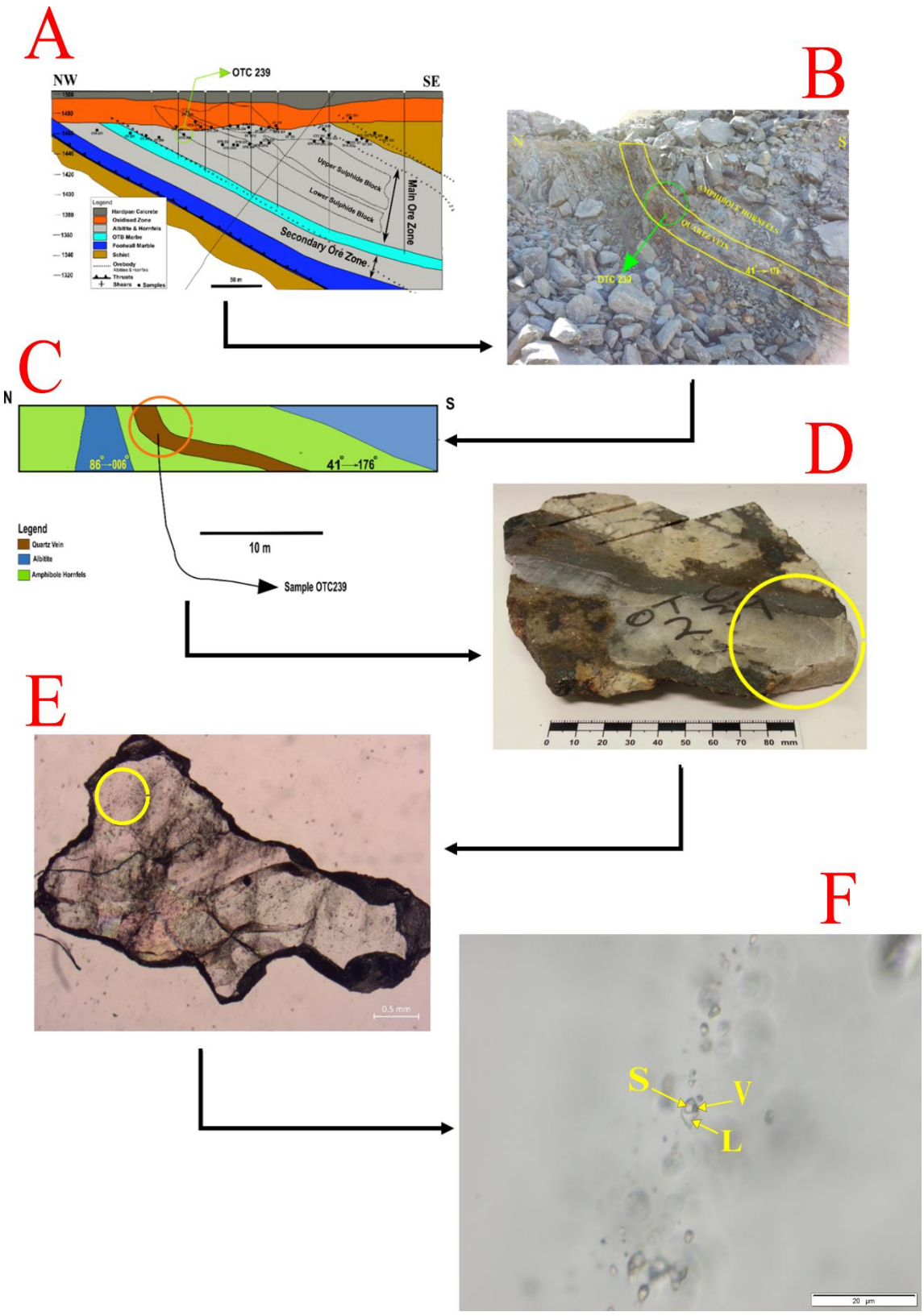

Figure 5-7. Diagrams that show the different steps for fluid inclusion petrography. A) Cross section of the Otjikoto deposit indicating the locality where sample OTC239 was taken. B) Shows a photograph of the sample locality of sample OTC239. C) Shows the face map from the field mapping in the open pit. D) Shows the hand specimen of sample OTC239 and the part that was used for preparing the double polished wafer. E) Shows a small double polished wafer chip (OTC239a). F) Shows a LVS type inclusion in a secondary trail (OTC239a_11)

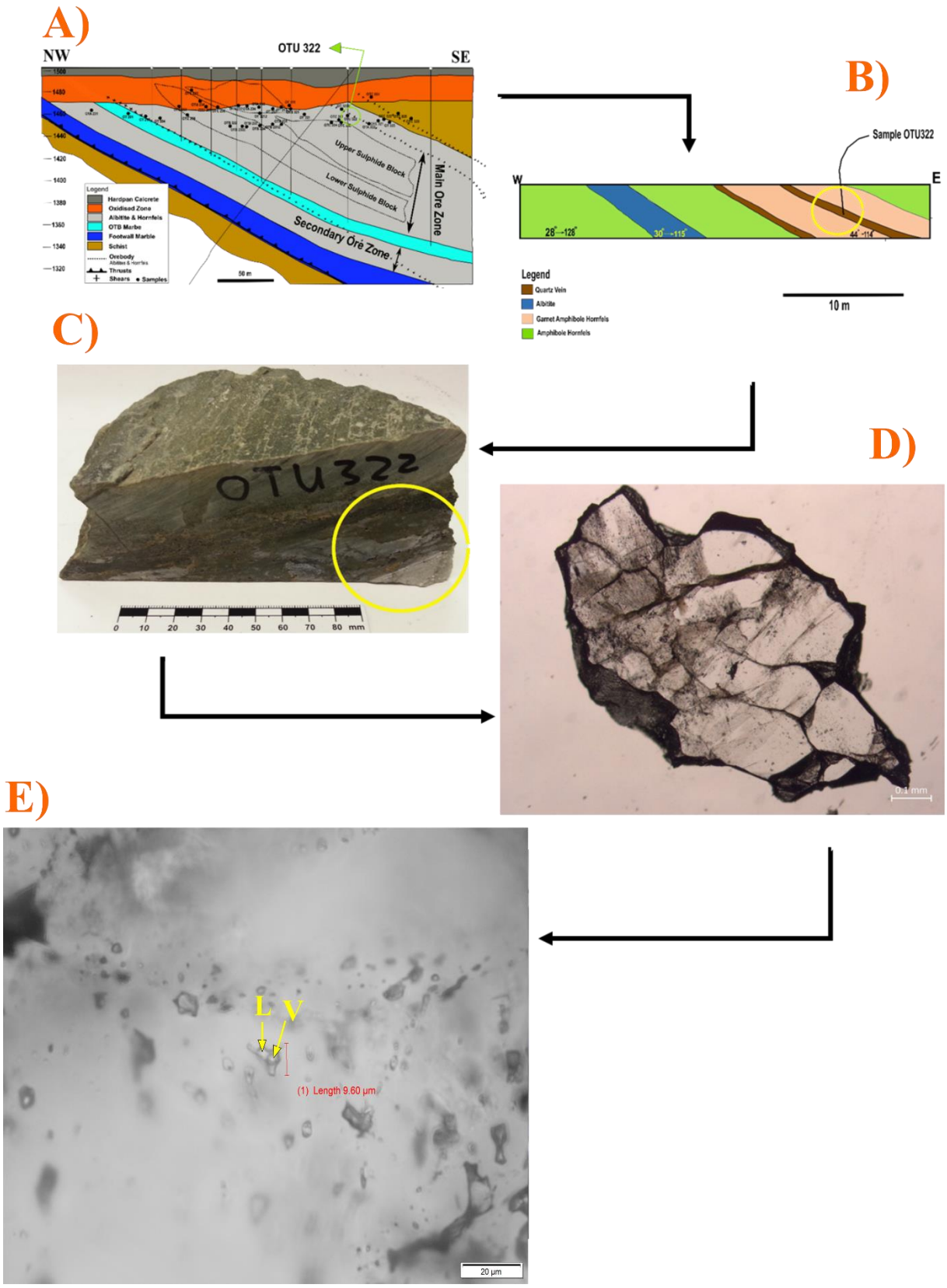

Figure 5-8. Diagrams that show the different steps for fluid inclusion petrography. A) Cross section of the Otjikoto deposit indicating the locality where sample OTU322 was taken. B) Shows the face map from the field mapping in the open pit. C) Shows the hand specimen of sample OTU322 and the part that was used for preparing the double polished wafer. D) Shows a small double polished wafer chip (OTU322b). E) Shows a LV type inclusion in a secondary trail (OTU322b_5).

5.3.1 Microthermometry

The fluid inclusions from Otjikoto are divided into 3 types, based on their microthermometric properties. The fluid inclusion types are aqueous, aqueous-carbonic and carbonic inclusions. Most of the phase transitions measured in sample OTC239 and OTU322 are from secondary inclusions. In sample OTU322, fewer phase changes were measured as most of the inclusions were relatively too small to observe (<9 µm). In both samples OTC239 and OTU322, all three types of inclusions were observed.

In sample OTC239, eighty-two inclusions were analysed in total. From the 82 inclusions analysed, only 66 inclusions showed phase transitions during the low temperature and high temperature measurements.

Twenty-three inclusions were analysed in sample OTU322. From the total, 20 inclusions showed phase transitions during the high and low temperature microthermometric runs. The inclusions from this sample were also categorised into primary (n = 12) and secondary (n = 11) fluid inclusions.

Type I: Aqueous Inclusions

These are the least common inclusion types that are found in samples OTC239 and OTU322. The sizes varied from 8 µm to 37 µm. These inclusions are generally colourless in appearance. The shapes of these inclusions are irregular and are generally elongated. The vapour to liquid proportion of these inclusions ranges from 10% to 40%.

The temperature measurements were obtained for 15 aqueous inclusions in total. In sample OTC239, 11 temperature readings were obtained while in sample OTU322, only 4 readings were obtained (Table 6). From the 11 inclusions measured in sample OTC239, 9 are secondary while 2 are primary. In sample OTU322, one aqueous inclusion is primary while 3 are secondary. The percentage of the vapour ranged from 10-40% in sample OTC239 and from 10-20% in sample OTU322.

The melting temperature of ice observed (Tm Ice) ranged from -20.8 to -0.5°C in sample OTC239 and from -19.8 to -18.3°C in sample OTU322 (n=8). The temperature of total homogenisation ranged from 156 to 221°C in sample OTU322 and from 129 to 444°C in sample OTC239 (n=10). For inclusions that contained halite crystals, the temperature of halite dissolution (Tm halite) ranged from 152 to 374°C in both samples (n=7). Using Tm halite values, the salinity for inclusions containing halite crystals ranged from 30 to 44.5 wt.% NaCl eq. (n=8). For fluid inclusions without halite crystals, the Tm ice values were used

to calculate the salinity which ranged from 0.9 to 22.9 wt.% NaCl eq. in sample OTC239 (n=7) and from 21.2 to 22.2 wt.% NaCl eq. in sample OTU322 (n=2). The bulk density of the aqueous inclusions were calculated by inputting the salinity and total homogenisation temperatures into the Bulk Software (Bakker, 2003). Within the Bulk software, the equation used for calculating the bulk density is by Bodnar (1993). The bulk density of aqueous inclusions ranged from 0.73 g/cm^3 to 1.23 g/cm^3. The phase change temperature variations of the aqueous inclusions are presented in histograms (Figure 5-13 and Figure 5-14).

Table 6 Microthermometry data of the aqueous inclusions from samples OTC239 and OTU322. All temperatures are measured in °C. The bulk density is expressed in g/cm^3.

Chip	FI	Phase	Type	Petro	size/µm	%vap	Tmice	Thtot	Mode	Tm halite	Salinity wt%NaCl	bulk density
OTU322b	2	LVS	Primary	Isolated	11	10.0		221	L	211	32.4	1.11
OTU322b	3	LV	Secondary	Trail	10	10.0	-18.3	156	L		21.2	1.07
OTC 239b	4	LVS	Secondary	Trail	9	15.0		187	L	340	41.9	1.23
OTU322b	4	LVS	Primary	Isolated	8	10.0				225		
OTC 239e	6	LV	Secondary	Trail	20	10.0	-18.9	287	L		21.6	0.95
OTC 239a	7	LV	Primary	Cluster	15	10.0	-15.0				18.6	
OTU322b	7	LV	Primary	Isolated	11	20.0	-19.8				22.2	
OTC 239b	8	LV	Secondary	Trail	16	10.0	-19.0				21.7	
OTC 239a	10	LVS	Secondary	Trail	13	10.0		444	L	374	44.5	1.01
OTC 239e	10	LVS	Secondary	Trail	17	10.0		356	L	346	42.1	1.07
OTC 239e	11	LVS	Secondary	Trail	9	10.0		129	L	177	31.4	1.18
OTC 239e	12	LV	Secondary	Trail	15	10.0	-20.8	363	L		22.9	0.88
OTC 239c	16	LV	Primary	Isolated	15	40.0	-0.5	290	L		0.9	0.73
OTC 239d	29	LVS	Secondary	Trail	16	10.0		129	L	152	30.0	1.17
OTC 239g	42	LV	Secondary	Trail	37	10.0	-3.0				5.0	

Type II: Aqueous-Carbonic Inclusions

These inclusions are common in samples OTC239 and sample OTU322. The sizes of the aqueous-carbonic inclusions range from 8 µm to 27 µm in both samples and are generally colourless in appearance. The vapour to liquid ratio of these inclusions ranges from 10% to 90%.

The temperatures of 21 aqueous-carbonic inclusions were measured in total. From the total, 15 inclusions were measured in sample OTC239 and 6 inclusions were measured in sample OTU322.

The temperature of clathrate melting (Tm clath) ranges from 0.3 to 8.1°C (n=8). The melting temperature of CO_2 (Tm CO_2) ranged from -60.2 to -57.4°C in sample OTU322 and from -59.8

to -57.2°C in sample OTC239 (n=10). The melting temperature of ice (Tm ice) ranged from -21.0 to -2.0 °C in both samples combined (n=6). The homogenisation temperature of CO_2 (Th CO_2) ranged from -40.8 to -10.7°C in sample OTU322 and from -39.3 to -14.0°C in sample OTC239 (n=11). The temperature of total homogenisation ranged from 156 to 384°C in sample OTU322 and from 151 to 488°C in sample OTC239 (n=9). The phase change temperature variations of the aqueous-carbonic are shown in the histogram presented in Figure 5-11, Figure 5-12, Figure 5-13, and Figure 5-14.

Table 7 Microthermometry temperature data of the aqueous-carbonic inclusions from samples OTC239 and OTU322. All temperatures are measured in °C.

Chip	FI	Phase	petro	size/µm	%vap	Tmice	TmCO2	ThCO2	Mode	Tm cla	Thtot	Mode
OTU322b	1	LV	primary	21	20.0		-59.3	-25.4	L			
OTC 239a	3	LV	primary	15	15.0	-2.0		-32.0	L	2.3	225	L
OTC 239e	3	LVS	secondary	22	20.0	-9.3					367	L
OTC 239a	4	LV	primary	8	15.0			-39.0	L	8.1		
OTC 239e	4	LV	Secondary	11	20.0	-16.6				0.5	151	L
OTU322b	5	LV	secondary	12	30.0			-40.8	L		295	L
OTC 239e	5	LVS	Secondary	9	10.0					2.1	488	V
OTU322b	6	LV	primary	10	10.0		-58.4	-10.7	L	2.2	384	L
OTC 239b	6	LV	primary	23	15.0		-58.0	-14.0	L			
OTC 239e	7	LV		13	90.0		-59.8	-39.3	L			
OTC 239h	7	LV	Primary	26	40.0					0.3		
OTC 239e	8	LV		18	20.0		-58.9	-22.9	L			
OTU322b	8	LV		9	40.0	-13.3	-57.4	-26.9	L			
OTC 239e	9	LVS		11	10.0		-57.2					
OTU322b	9	LV	secondary	17	10.0		-60.2	-10.7	L			
OTU322b	10	LV	primary	13	10.0						156	L
OTC 239a	11	LVS	primary	27	10.0							
OTC 239a	12	LV	secondary	16	20.0	-21.0				4.9	289	L
OTC 239c	15	LV	secondary	15	10.0		-59.0	-23.0	L			
OTC 239g	34	LVS	Primary	19	15.0					2.3	321	L
OTC 239f	46	LV	secondary	24	20.0	-7.0	-58.1					

Type III: Carbonic Inclusions

The gaseous inclusions are the most common inclusions observed in samples OTC239 and OTU322. The carbonic inclusions are generally dark in colour. The sizes of these inclusions range from 5 µm to 38 µm. The vapour to liquid ratios of these inclusions ranges from 10 % to 90% vapour.

In sample OTC239, temperature measurements of 41 carbonic inclusions were obtained (*Table 8*). Most of these inclusions were monophase with a vapour percentage of 90% in both samples combined. In sample OTU322, 10 carbonic inclusions were measured of which 4 inclusions were primary and 6 inclusions were secondary.

The initial melting temperature of CO_2 (Tm CO_2) ranged from -59.4 to -57.5°C in sample OTU322 and from -61.0 to -58.0°C in sample OTC 239 (n=50). The homogenisation temperature of CO_2 (Th CO_2) into the liquid phase ranged from -50.6 to -4.4°C in sample OTU322 and from -55.1 to -9.0°C in sample OTC239 (n=47). The composition of the gaseous inclusions was determined by plotting the Tm CO_2 and Th CO_2 values onto the VX composition diagram (Thiéry et al., 1994). The gaseous composition plot is shown in *Figure 5-9*. In both samples combined, the fluid composition (X) range of CO_2 and CH_4 is 0.8-1.0 and 0-0.2 (n=46) respectively (*Table 8*). The bulk density of the gaseous inclusions was calculated by inputting Th CO_2 and the composition of CO_2 and CH_4 into the bulk software (Bakker, 2003). The equation of state used for calculating the bulk density is by Thiéry et al., (1994). The temperature variations of the phase changes are presented in histograms shown in Figure 5-11 and Figure 5-12.

Table 8 Microthermometry temperature data of the carbonic inclusions from samples OTC239 and OTU322. All temperatures are measured in °C. The bulk density is expressed in g/cm^3.

Chip	FI	Phase	Type	petro	size/µm	% Vap	TmCO2	ThCO2	Mode	CO2	CH4	bulk density
OTC 239h	1	Monophase	Secondary	Trail	28	90	-59.8	-34.5	L	0.9	0.1	0.97
OTU322a	1	Monophase	Primary	isolated	15	90	-59.4	-50.6	L	0.9	0.1	1.00
OTC 239b	2	Monophase	Primary	isolated	17	90	-59.0	-19.0	L	0.9	0.1	0.91
OTC 239h	2	Monophase	Secondary	Trail	15	90	-59.9	-30.9	L	0.9	0.1	0.96
OTU322a	2	Monophase	Primary	isolated	20	90	-58.4	-18.5	L	0.9	0.1	0.95
OTC 239b	3	Monophase	Primary	cluster	16	90	-58.0	-19.2	L	0.9	0.1	0.91
OTC 239h	3	Monophase	Secondary	Trail	27	90	-58.8	-29.6	L	0.9	0.1	0.95
OTU322a	3	Monophase	Primary	isolated	18	90	-58.5	-33.5	L	0.9	0.1	1.00
OTC 239h	4	Monophase	Primary	isolated	20	90	-60.3	-41.2	L	0.8	0.2	0.89
OTU322a	4	Monophase	Primary	isolated	8	90	-59.4	-25.2	L	0.9	0.1	0.90
OTC 239b	5	Monophase	Secondary	Trail	26	90	-59.0	-11.0	L	0.9	0.1	0.87
OTC 239h	5	Monophase	Primary	isolated	23	90	-60.1	-25.7	L	0.8	0.2	0.83
OTU322a	5	Monophase	Secondary	Trail	16	90	-58.8	-22.3	L	0.9	0.1	0.92
OTC 239h	6	Monophase	Secondary	Trail	38	90	-59.5	-38.4	L	0.9	0.1	0.99
OTU322a	6	Monophase	Secondary	Trail	11	90	-57.9	-7.4	L	0.9	0.1	0.86
OTU322a	7	Monophase	Secondary	Trail	12	90	-57.9	-28.5	L	1.0	0.0	1.03
OTC 239h	8	Monophase	Secondary	Trail	22	80	-58.8	-17.8	L	0.9	0.1	0.90
OTU322a	8	Monophase	Secondary	Trail	14	90	-58.2	-4.4	L	0.9	0.1	0.84
OTC 239b	9	Monophase	Secondary	Trail	18	90	-59.0	-13.0	L	0.9	0.1	0.88
OTC 239h	9	Monophase	Primary	isolated	24	90	-59.1	-19.7	L	0.9	0.1	0.91
OTU322a	9	Monophase	Secondary	Trail	12	90	-57.5	-21.9	L	1.0	0.0	1.01
OTC 239h	10	Monophase	Primary	isolated	19	90	-59.9	-52.2	L	0.9	0.1	1.03
OTU322a	12	Monophase	Secondary	Trail	21	90	-57.7	-24.2	L	1.0	0.0	1.01
OTC 239c	14	Monophase	Primary	isolated	13	90	-60.0	-23.6	L	0.8	0.2	0.82
OTC 239c	17	Monophase	Secondary	Trail	12	90	-60.0	-34.0	L	0.8	0.2	0.86
OTC 239c	18	Monophase	Primary	isolated	11	90	-59.0	-47.0	L	0.9	0.1	1.02
OTC 239c	19	Monophase	Secondary	Trail	12	90	-60.0	-29.0	L	0.8	0.2	0.88
OTC 239c	20	Monophase	Secondary	Trail	19	90	-59.0	-9.0	L	0.9	0.1	0.86
OTC 239c	21	Monophase	Primary	isolated	14	90	-61.0	-53.0	L	0.9	0.1	0.99
OTC 239c	22	Monophase	Primary	isolated	12	90	-60.0	-49.0	L	0.8	0.2	0.92
OTC 239d	23	Monophase	Secondary	Trail	18	90	-60.0	-49.0	L	0.8	0.2	0.97
OTC 239d	24	Monophase	Secondary	Trail	9	90	-60.0	-21.5	L	0.8	0.2	0.85

OTC 239d	25	Monophase	Primary	isolated	14	90	-59.0	-45.0	L	0.9	0.1	0.99
OTC 239d	26	Monophase	Primary	isolated	25	90	-59.0					
OTC 239d	27	Monophase	Primary	isolated	20	90	-60.0	-50.0	L	0.9	0.1	0.98
OTC 239d	28	Monophase	Secondary	Trail	15	90	-59.4	-19.0	L	0.9	0.1	0.87
OTC 239d	31	Monophase	Secondary	Trail	10	90	-60.0	-49.0	L	0.8	0.2	0.97
OTC 239d	32	LV	Primary	isolated	17	10	-60.0					
OTC 239d	33	Monophase	Primary	cluster	7	90	-59.0					
OTC 239g	35	Monophase	Secondary	Trail	19	90	-59.0					
OTC 239g	36	Monophase	Primary	isolated	16	90	-60.0	-45.0	L	0.8	0.2	0.95
OTC 239g	37	Monophase	Secondary	Trail	14	90	-60.0	-42.0	L	0.9	0.1	0.93
OTC 239g	38	Monophase	Secondary	Trail	27	90	-59.0	-32.0	L	0.9	0.1	0.94
OTC 239g	39	Monophase	Secondary	Trail	21	90	-59.0	-39.0	L	0.9	0.1	0.96
OTC 239g	43	Monophase	Secondary	Trail	23	90	-60.0	-32.0	L	0.9	0.1	0.90
OTC 239g	44	Monophase	Secondary	Trail	29	90	-59.7	-42.6	L	0.9	0.1	0.96
OTC 239g	45	Monophase	Secondary	Trail	24	90	-59.6	-35.0	L	0.9	0.1	0.92
OTC 239f	47	Monophase	Primary	isolated	16	90	-60.2	-55.1	L	0.9	0.1	0.99
OTC 239f	48	Monophase	Primary	isolated	16	90	-60.0	-52.6	L	0.8	0.2	0.98
OTC 239f	49	Monophase	Primary	isolated		90		-51.1	L			
OTC 239f	50	Monophase	Primary	isolated	5	90	-60.3	-59.1	L	0.8	0.2	1.01

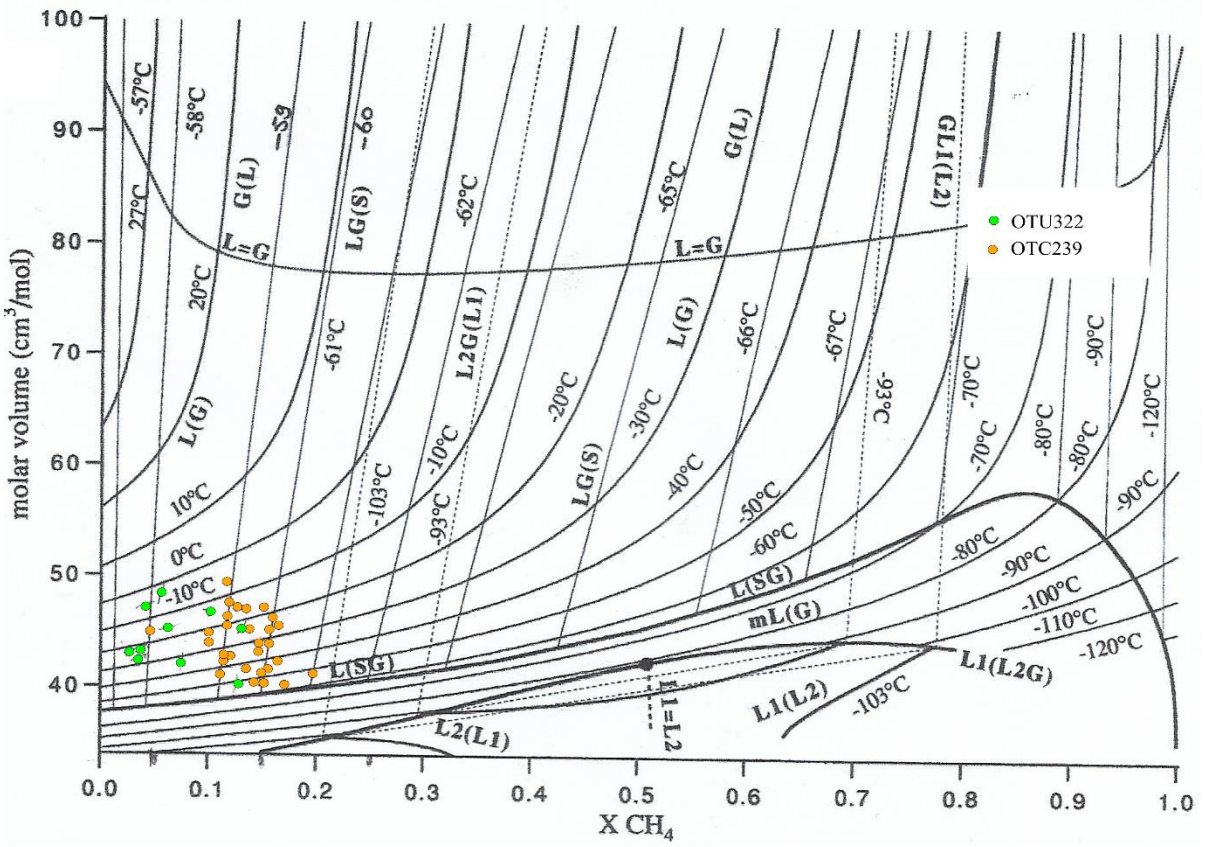

Figure 5-9 VX diagram for the CO_2-CH_4 fluid system. The orange points represent the Tm CO_2 and Th CO_2 plots for sample OTC239 while the green points represent Tm CO_2 and Th CO_2 plots for sample OTU322.

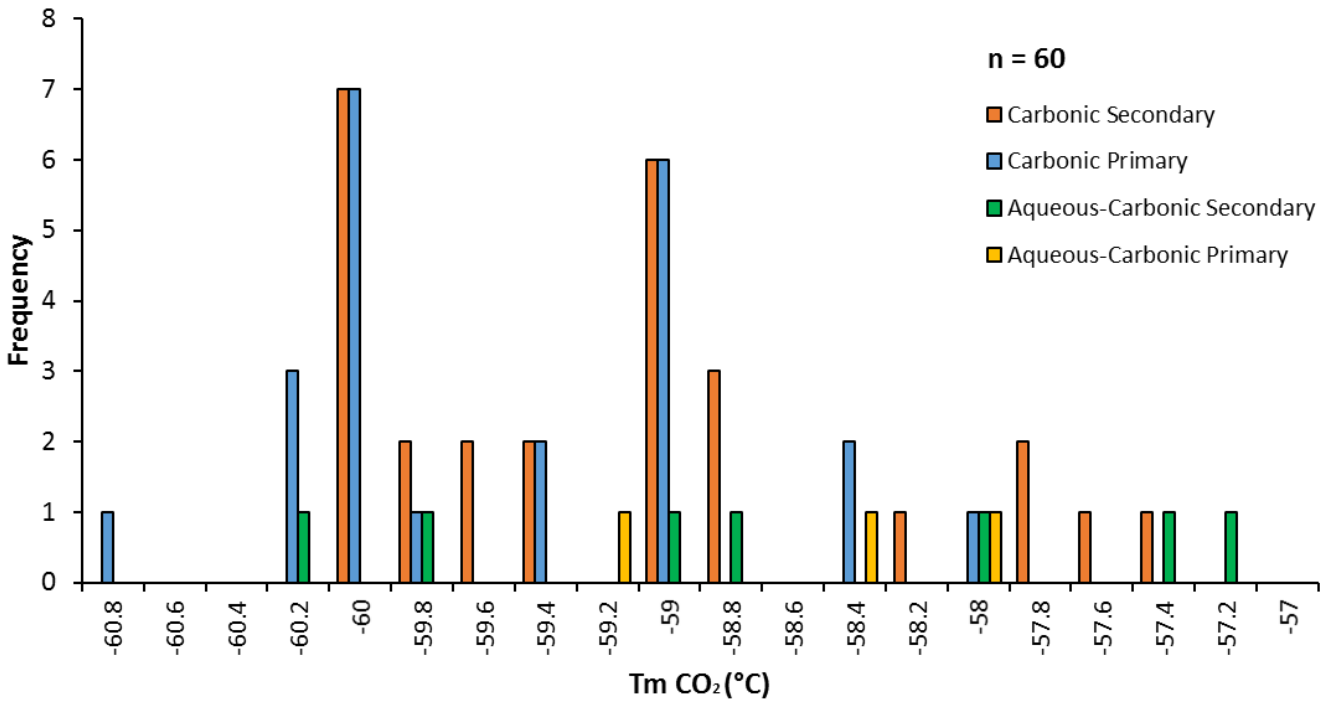

Figure 5-11 Histogram showing the distribution of the melting temperature of CO_2 (Tm CO2) for carbonic and aqueous-carbonic inclusions.

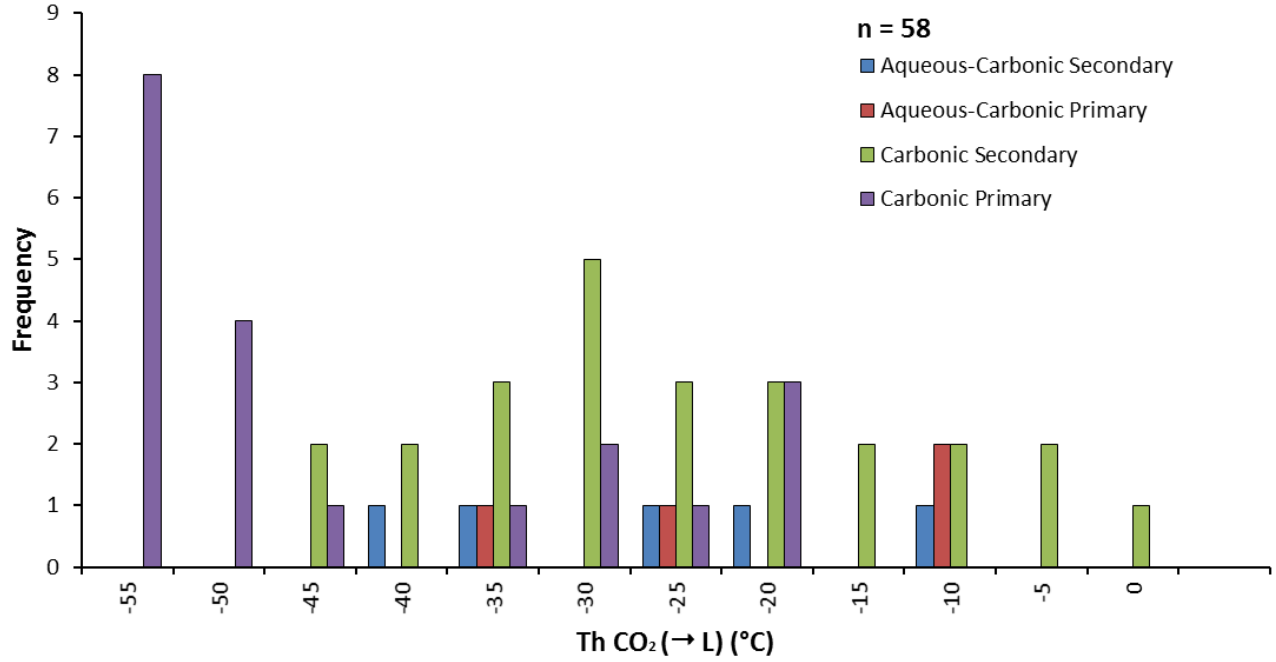

Figure 5-12 Histogram showing the distribution of the homogenisation temperature of CO_2 to the liquid phase (Th CO_2) for carbonic and aqueous-carbonic inclusions.

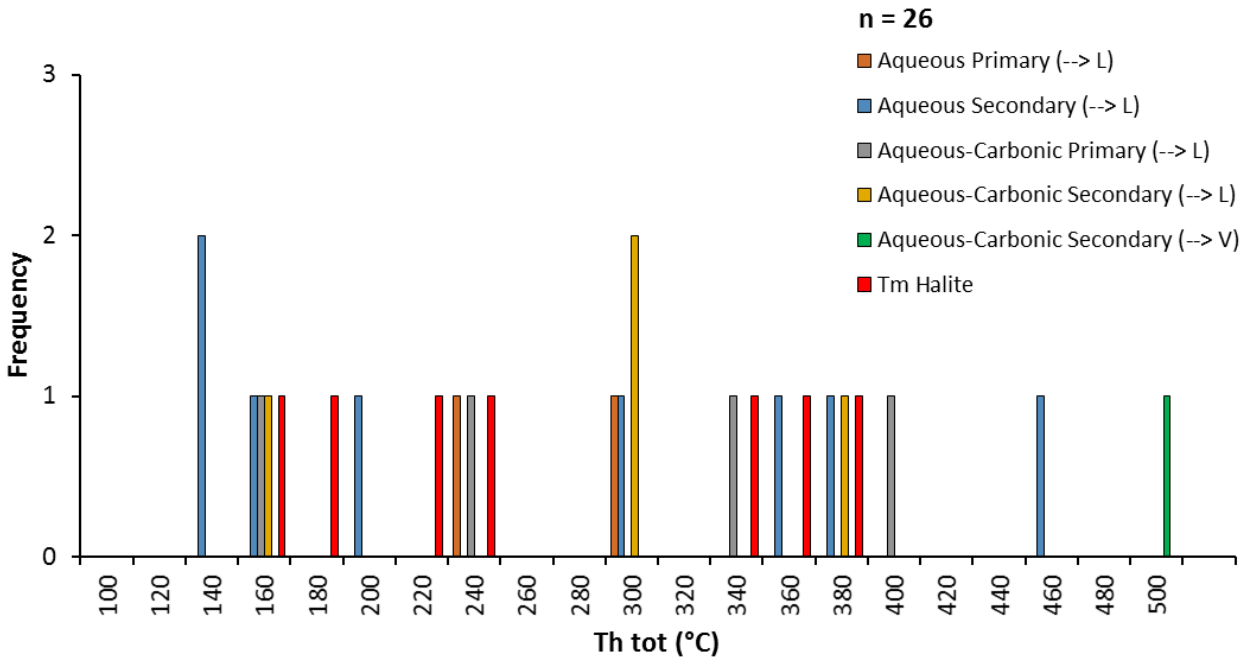

Figure 5-13 Histogram showing the distribution of the total homogenisation temperature (Th tot) for aqueous and aqueous-carbonic inclusions. Tm halite values are also plotted on the same histogram.

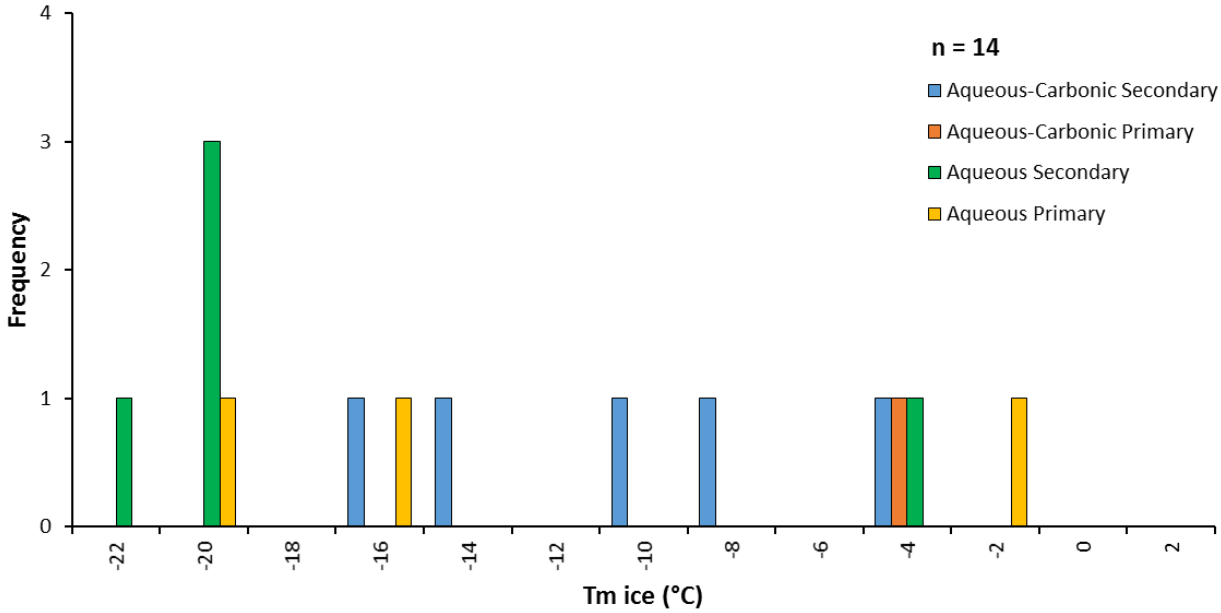

Figure 5-14 Histogram showing the distribution of the melting temperature of ice (Tm ice) for aqueous and aqueous-carbonic inclusions.

5.4 Oxygen Isotopes

The $\delta^{18}O$ values were obtained for quartz and magnetite samples from the mineralised veins. The values are 8.35 ‰ and 8.75 ‰ for the magnetite (n=2) and 17.51 ‰ to 18.47 ‰ for the quartz samples (n=4) (Table 9). The quartz and magnetite grains were extracted from veins which are hosted by the amphibole hornfels, garnet amphibole hornfels and albitites from the Okonguarri Formation. The average $\delta^{18}O$ values for the magnetite grains are 8.55 ‰ (n=2). A previous study on the Otjikoto deposit by Curtis (2006) showed that the $\delta^{18}O$ for the vein quartz range between 16.8 ‰ to 18.3 ‰. The quartz grains have an average $\delta^{18}O$ value of 18.11 ‰ (n=4) which is within same range as the result obtained by Curtis (2006).

Table 9 Stable isotope data for the magnetite and vein quartz from samples OTC239, OTU322, OTC232 and OTC2311

Sample ID	d18O (‰)	Mineral
OTC239 qtz	18.47	Quartz
OTU322 qtz	18.03	Quartz
OTC239 mgt	8.75	Magnetite
OTC2311 qtz	17.51	Quartz
OTC232 qtz	18.42	Quartz
OTC2311 mgt	8.35	Magnetite

5.4.1 Oxygen Isotope Thermometry

Stable isotopes analysis can be used to determine the equilibrium temperatures of mineral assemblages. An important aspect is that fractionation of isotopes decreases as the temperature increases and is independent of the pressure changes (Weiss, 2013). Quartz is enriched in ^{18}O whereas magnetite is depleted in ^{18}O (Weiss, 2013). The oxygen isotope fractionation factor is expressed by:

$$\alpha_{1\text{-}2} = R_1/R_2 \qquad \text{(Hoefs, 1997)}$$

Whereby R= $^{18}O/^{16}O$ of each mineral which participates in the fractionation process. The fractionation factor (α) further be expressed in terms of temperature (Bottinga & Javoy, 1973):

$$1000 \ln \alpha = A \times 10^6 T^{-2}$$

The letter A is the thermometric coefficient and T is the absolute temperature expressed in Kelvin (Javoy, 1977). There is a relationship between the δ-values of two minerals and the isotope fractionation between them (Weiss, 2013):

$$\Delta_{1\text{-}2} = \delta_1 - \delta_2 = 1000 \ln \alpha_{1\text{-}2} \quad \text{if } \delta < 10 \text{ ‰} \qquad \text{(Hoefs, 1997)}$$

$$\alpha_{1\text{-}2} = 1000 + \delta_1 / 1000 + \delta_2 \quad \text{if } \delta > 10 \text{ ‰} \qquad \text{(Hoefs, 1997)}$$

The above equations allow the fractionation temperatures to be calculated by applying the $\delta^{18}O$ values of two minerals which are in textural equilibrium. The error estimate for oxygen isotopes is 0.2 per mil. The fractionation temperatures were calculated for two of these samples (OTC2311 and OTC239) and found to be 554.8-555.2°C and 533.8-534.2°C respectively with an error estimate of 0.2 per mil.

6 Discussion

6.1 Fluid inclusion study

The type of fluid inclusion populations at Otjikoto are distinguished based on their arrangements within the quartz veins and the composition of the fluid present at the time of entrapment.

The fluids within the Okonguarri Formation contain a combination of aqueous, aqueous-carbonic and carbonic inclusions. Of the three types of fluid inclusion types that are present at Otjikoto, the carbonic fluids are the most common (n=51).

The melting temperatures of the vapour in the carbonic systems was below the critical point of CO_2 (-56.6 °C), hence no pure single phase CO_2 inclusions are present. The $TmCO_2$ values which plot over a range of -61.0°C to -57.2 °C is evidence that other gases are present in the orogenic fluids of Otjikoto.

As only a few aqueous inclusions were observed which may signify the close association of hydrous minerals (biotite and muscovite) with the quartz-vein at Otjikoto. The minor occurrences of aqueous inclusions may be a result of a) Unmixing of H_2O-CO_2 fluid systems and the selective trapping of CO_2, b) selective leakage of H_2O rich fluids from the individual inclusions and c) two fluid systems (aqueous and carbonic) operating separately (Klein & Fuzikawa, 2010).

At room temperatures, the carbonic inclusions from the Okonguarri Formation showed a 90% volume of CO_2. The fluid inclusions appear in quartz veins that cross-cut across the bedding at Otjikoto. Methane, which is also present in the carbonic inclusions, is a common gas that is found in sedimentary basins and forms due to the breakup of orogenic material at high temperatures and pressures. Methane is common in digenetic inclusions (Goldstein & Reynolds, 1994).

The moderate to high salinity of the aqueous inclusions of the fluids are also supported by the presence of daughter crystals at room temperature. The salinities ranged from 30.0 to 44.5 wt. % NaCl eq. in aqueous inclusions with halite crystals and from 0.9 to 22.9 wt. % NaCl eq. in inclusions without halite crystals. The high salinities at Otjikoto may be attributed to retrograde metamorphic hydration reactions.

Fluid immiscibility is believed to be an important process that takes place in the deposition of many epithermal and mesothermal orogenic gold deposits (Naden & Shepherd, 1989). There

are a few aspects which are used as evidence for fluid immiscibility, namely: (1) Similar homogenisation temperature (Th CO_2) ranges for aqueous-carbonic and carbonic inclusions which implies that the two fluid types have similar ages (Ramboz et al., 1982). (2) The co-existence of clusters of aqueous-carbonic with both primary carbonic and aqueous-carbonic inclusions which implies that these inclusions formed from heterogeneous mixtures with two end members (Yao et al., 2001). (3) Homogenisation temperatures which are lower in aqueous inclusions than in primary aqueous-carbonic inclusions (Gubelin & John, 1986). (4) An H_2O phase percentage volume of 10-20% at room temperature or an invisible H_2O phase in the carbonic inclusions which may imply that H_2O depleted and CO_2 enriched end members resulted from phase separation of an H_2O-CO_2 fluid (Burrus, 1981). Based on the criteria for fluid immiscibility and fluid inclusion observations of the samples from Otjikoto, there is evidence of fluid immiscibility. The homogenisation temperature of CO_2 (Th CO_2) values of the aqueous-carbonic and carbonic inclusions have similar ranges as shown in Figure 5-13 above. The Th CO_2 values ranged from -55.1 to -9 in the carbonic inclusions and from -40.8 to -10.7 in the aqueous-carbonic inclusions which implies that the two fluid inclusion types have a similar age range. In addition, the primary aqueous and carbonic inclusions do co-exist with the aqueous-carbonic inclusions in clusters. Although not many measurements were obtained, the homogenisation temperatures (Th tot) were found to be generally lower in the aqueous inclusions than in the primary aqueous-carbonic inclusions. A plot of total homogenisation vs. salinity shows a large spread which may be indicative of fluid immiscibility (*Figure 6-1*).

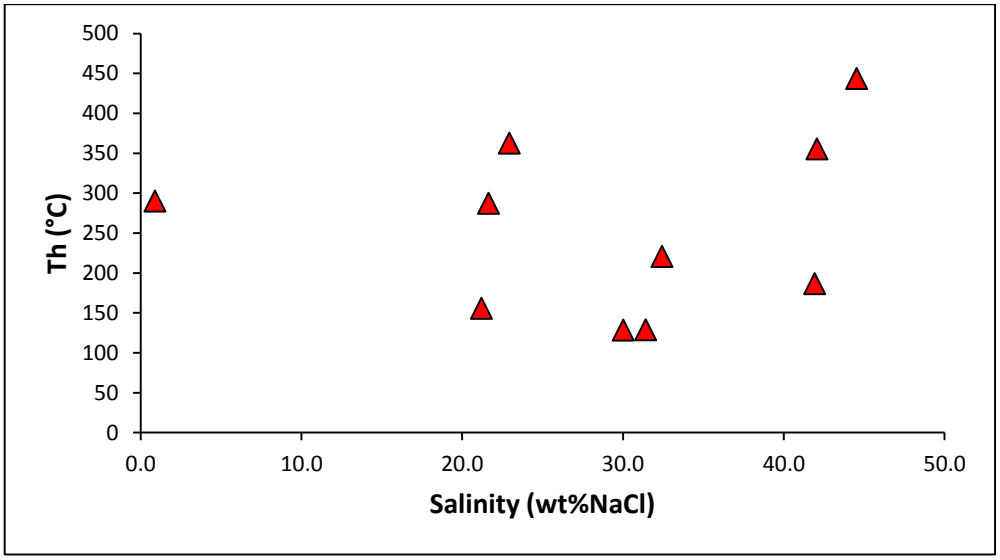

Figure 6-1 A plot of Total homogenisation vs. Salinity which shows the data spread for the aqueous inclusions that may be indicative of fluid immiscibility.

The inclusions from Otjikoto show a large density variation ranging from 0.73 to 1.23 g/cm^3 in the aqueous inclusions and from 0.81 to 1.03 g/cm^3 in the carbonic inclusions. Large

densities may be a result of fluid trapping under fluctuating pressure, fluid trapping under decreasing density, or water leakage, re-equilibrium under retrograde conditions or any combination of these factors (Klein & Fuzikawa, 2010).

The immiscibility of CO_2-H_2O fluids is well known in metamorphic fluids at shallow crustal levels, especially for forming hydrothermal ores (Kaszuba et al., 2006). The multiphase immiscibility of CO_2-H_2O fluids usually takes place over wide temperature and pressure ranges, close to 400°C and 300 MPa (Kaszuba et al., 2006). CO_2-H_2O immiscibility is usually accompanied by geochemical and textural evidence, although no textural evidence can be highlighted. An important characteristic of CO_2-H_2O immiscibility is that aqueous reactions are influenced by supercritical CO_2 fluids which results in metals being dissolved and redistributed as organometallic compounds (Kaszuba et al., 2006). The immiscible supercritical CO_2 produces acidic brines that are silica and carbonate saturated (Kaszuba et al., 2006). These brines are placed into rock systems and facilitate the precipitation of carbonates and quartz in veins (Kaszuba et al., 2006).

It is therefore proposed that the aqueous (H_2O) and carbonic inclusions (CO_2-CH_4) from the Okonguarri Formation are the end members of fluid immiscibility. The large range of homogenisation temperatures may indicate that these are a product of the two end members. The presence of CO_2 and CH_4 may be justified by the decomposition of the carbonaceous metasediments which are found in the stratigraphy at Otjikoto.

6.1.1 Pressure-Temperature Conditions

The measured total homogenisation temperature (Th tot) of the aqueous and aqueous-carbonic inclusions yields only the minimum temperature of trapping (Shepherd et al., 1985). The following aspects are used to determine the maximum temperature of trapping: (1) The isochore intersection of the co-existing fluids, (2) the dissolution temperatures of the daughter crystals, (3) the crystallization temperatures calculated using independent geothermometers (e.g oxygen isotope thermometry) and (4) the vapour pressure at the homogenisation temperature (Shepherd, et al., 1985; Ashworth, 2014). The temperatures obtained from stable isotope thermometry were found to be found to be 534°C and 555°C which could be interpreted as possible ore formation temperatures.

Isochores are used for estimating the minimum trapping pressure and temperature of the fluids. The isochores for aqueous inclusions were calculated by inputting the salinity, bulk density and the homogenisation temperatures into the ISOC software (Bakker, 2003). The equation of state used for the Isochore calculation is by Bodnar and Vityk (1994). The calculated isochores

were used to plot a temperature vs pressure curve (Figure 6-2). The isochores for the gaseous inclusions were calculated by inputting the bulk density and composition of CH_4 and CO_2 into the ISOC software. The equation of state used for the isochore calculation is by Holloway (1977).

Not all the micro thermometric data could be used to plot the isochores as some of the data generated is limited. The gradient of the aqueous inclusions are higher than those of the carbonic inclusions (Figure 6-2). The higher gradient represents a higher density whereas a lower gradient represents a lower density.

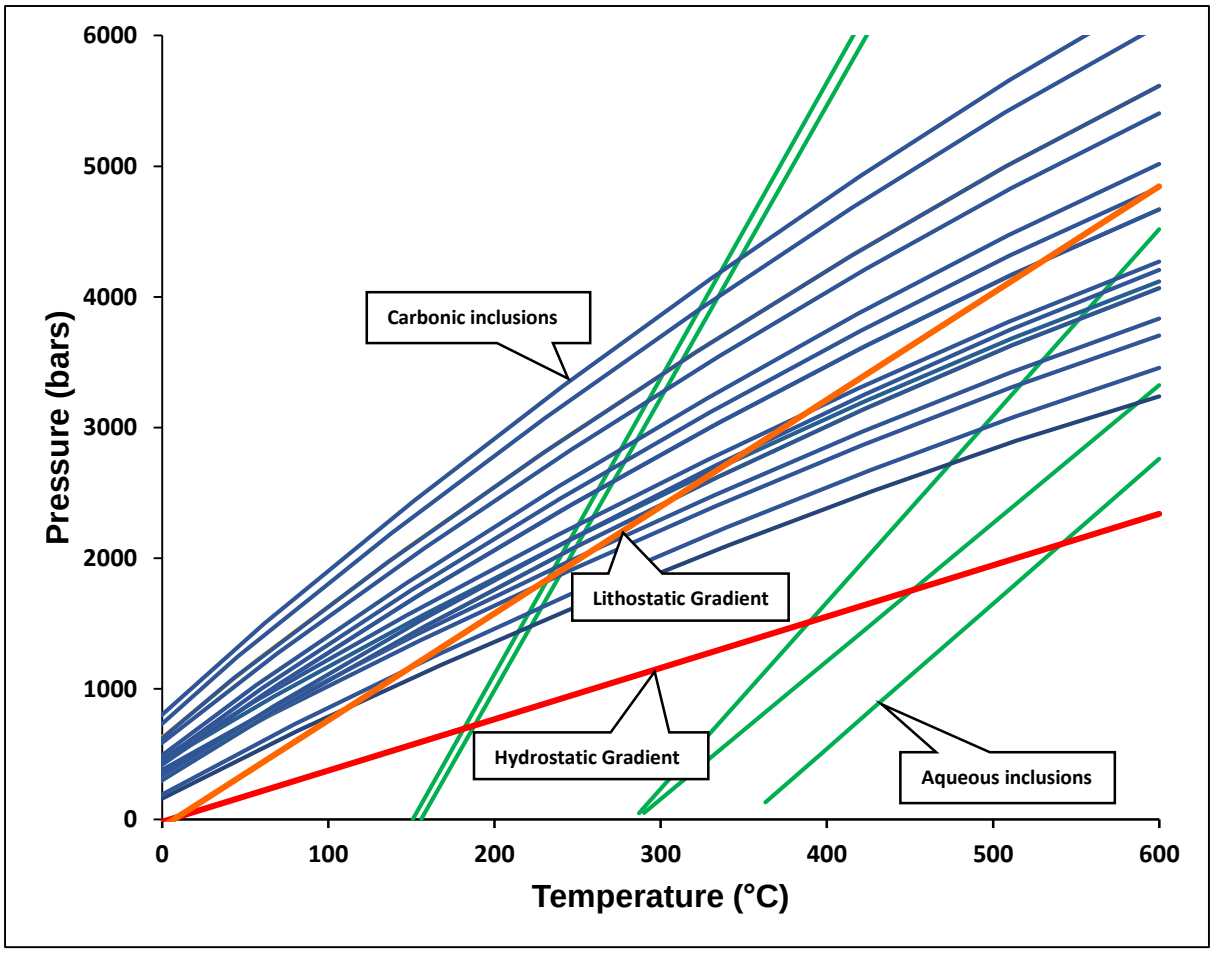

Figure 6-2 Isochore plots for the fluid inclusions at the Otjikoto deposit. The lines with the steep slopes (green) represent the aqueous inclusions. The lines with the shallow slope (blue) represent the carbonic inclusions. The lithostatic gradient is shown by the orange line. The hydrostatic gradient is shown by the red line.

The depth of the ore formation conditions were calculated by using the equation:

$$P = pgz \qquad \text{(Equation 1)}$$

P represents the pressure in bars, g is the gravitational acceleration (9.8 m/s^2), z is the depth and p is the lithostatic density (2.60 g/cm^3 for metamorphic rocks). At temperatures of the

550°C, the fluids intersect the lithostatic gradient at 4 kbar which corresponds to a depth of ~16km.

6.2 Mineral Chemistry

A plot of X_{Fe} vs Si by Hey (1954) Figure 5-1 shows that these chlorites can be classified as ripidolite, pycnochlorite, diabantite and talc-chlorites. The majority of the chlorites fall within the ripidolite stability field. At Otjikoto, the chlorites are believed to have replaced amphiboles during retrograde metamorphism within the greenschist facies (Scheepers, 2000). Chlorite geothermometric calculations were applied on the microprobe data as shown in Table 2. The results from chlorite geothermometry show that the temperature of chlorite formation ranges from 220.7°C to 358.2°C which is lower than the temperature obtained from stable isotope thermometry.

The amphiboles analysed are magnesium rich and plot within the anthophyllite stability field of the XMg vs Si diagram by Leake et al., (2003) as shown in Figure 5-2. Petzel (2010) points out that the amphiboles from Otjikoto are usually surrounded by bleached haloes which suggests that they have formed from the breakdown of earlier alteration or metamorphic minerals such as ankerite or dolomite. Amphibole alteration has commonly been observed in the shear zones at Otjikoto (Petzel, 2010).

6.3 Major Elements

The Harker diagrams in Figure 5-3 show that the amphibole hornfels has a wide compositional variation of Al_2O_3 (6-18 wt. %), MgO (1-4.2 wt. %), CaO (2-10 wt. %), Na_2O (3-8 wt. %) and FeOt (2-8 wt. %). The albitites also show a similar compositional variation of Al_2O_3 (6-15 wt. %), MgO (1-5.2 wt. %), CaO (2-12 wt. %), Na_2O (3.3-9 wt. %), and FeOt (3-8.5 wt. %). All the samples analysed show a strong negative correlation of TiO_2, Al_2O_3, MgO, Na_2O and FeOt vs SiO_2. On the Ni, Zr, Y, Sr, Rb, Cr and Ba vs SiO_2 harker diagrams, no correlation could be inferred.

6.4 Trace Elements

Based on the trace element composition, the rocks from Otjikoto were subdivided into 3 categories namely albitites, amphibole hornfels, and biotite schists. The albitites show similar REE patterns as shown in Figure 5-6. All the albitites exhibit a negative Eu anomaly which may be attributed to a reduced magma that lost Eu during the fractional crystallisation of plagioclase. The banded amphibole hornfels, garnet amphibole hornfels and amphibole

hornfels all showed similar REE patterns and were grouped together on the same diagram as shown in Figure 5-6. All of these samples were more enriched with LREE in comparison to the HREE concentrations. The garnet biotite schist and biotite schist all showed similar REE patterns and were grouped together on the same plot as shown in Figure 5-6. These samples showed a moderate Eu anomaly.

The analysed samples showed a large compositional variation of Rb (1-50 ppm), Sr (40-130 ppm), Y (17-47 ppm), Ba (2-250 ppm), La (17-47 ppm), Ce (33-95 ppm) and Zr (100-250 ppm). The Sr, Y, La and Ce vs Zr plots show a strong positive correlation (Figure 5-5).

6.5 Albitisation

Orogenic gold deposits have undergone hydrothermal alteration which is created in zonal patterns (Groves et al., 1998). The composition and intensity of the alteration is proportional to the crustal level and the composition of the wall rock (McCuaig & Kerrich, 1998). However, in clastic sedimentary host rocks, alteration is bound to small zones around the ore bodies (Groves et al., 1998). The main minerals formed by wall rock alteration are sulphide minerals (arsenopyrite, pyrrhotite or pyrite), carbonate minerals (dolomite, ankerite, magnetite, calcite or siderite), alkali enriched silicates (albite, Sericite, biotite, K-feldspar or aragonite), quartz and chlorite (Goldfarb et al., 2000).

The resultant fragile rock, from the albitisation of the biotite schist, cracked widely during the D3 and D4 deformational events (McDonald et al., 2011). These events deformed the Karibib Formation marble rock unit in a ductile way and allowed mineralising fluids to develop (McDonald et al., 2011). The albitisation process of the biotite schist and albite hornfels seen at Otjikoto is an irregular event inside the Central Zone of the Damaran Belt (Van Der Merwe & Wanless, 2007). The rheology of the host rock has been altered by the intense albitisation procedure which means the albitised zones may be more likely to host auriferous quartz veins (Van Der Merwe & Wanless, 2007).

There is an abundance of albite in rocks at Otjikoto. The albite content is caused by sodic metasomatism resulting in widespread albitisation (Tomkinson, 1999). There are instances where the garnet-biotite schist has undergone less albitisation, with the original rock still being unchanged (Tomkinson, 1999). The albitisation event occurred during the D1 deformational event, which resulted in isoclinal folding (Tomkinson, 1999). The presence of medium to large amphibole porphyroblasts in some rock units is a result of static thermal metamorphism at a later period (Tomkinson, 1999). The host rocks of the vein at Otjikoto are interpreted to be albitised contact metamorphosed and are therefore related to distal skarnification (Tomkinson,

1999). Geochemical analysis of core logs from Otjikoto indicates that albite is the main replacement mineral at Otjikoto (Curtis, 2006). Between the lithologies at Otjikoto, the albitite underwent the highest degree of metasomatism whereas the footwall marble is not metasomatised (Curtis, 2006). In terms of ranking the degree of albitisation (*Figure 6-3*), the albitite is followed by the albite biotite schist, amphibole albitite, biotite banded amphibole albitite, biotite schist, garnet biotite schist and marble (Curtis, 2006). During the main albitisation process, the metasomatic fluids spread widely and percolated through weak structures in the country rock (Curtis, 2006) . The albitised units host the bulk of the mineralised veins. In addition to albitisation, some of the country rock units were altered by chlorite-amphibole alteration (Petzel, 2010). The major oxide data shows that the albitite have the highest Na_2O content of 9 wt. %, which may be attributed to the abundance of the sodium rich feldspar (albite) in the rock unit. The Na_2O values range between 3.2 and 9 wt. %. The biotite schist has a Na2O content of 7.8 wt. %. The banded amphibole hornfels has a Na_2O content of 6 wt. %.

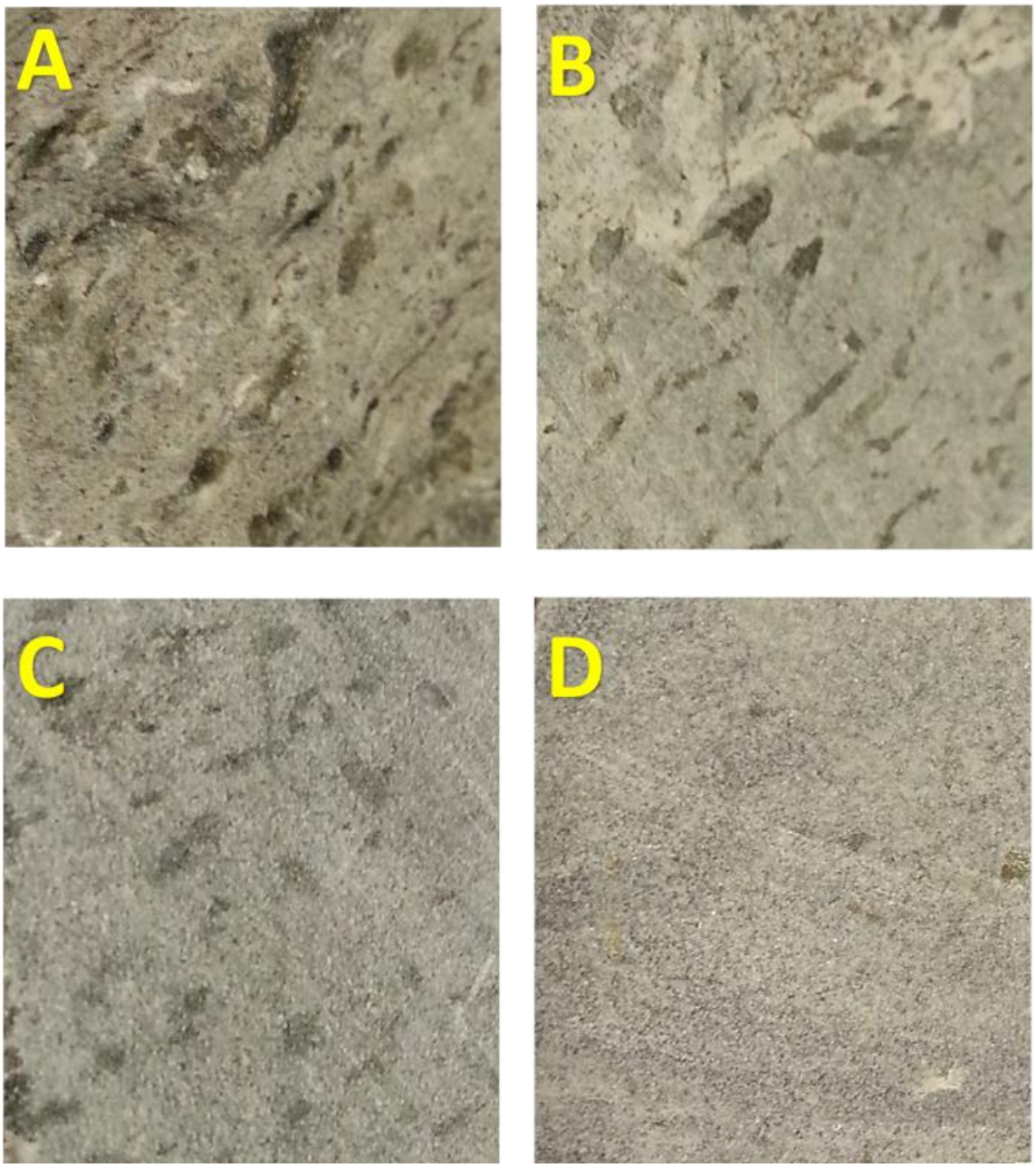

Figure 6-3 Rock textures of the various stages of Albitisation. Image A shows the texture of a coarse grained biotite schist (first stage of albitisation). Image B shows an albite biotite schist. Image C shows the amphibole hornfels. Image D shows the fine-grained albitite (last stage of albitisation).

During the Na-Ca metasomatic process, Na was exchanged for Ca or K, and in some instances, Ca is exchanged for Fe and Mg (Scheepers, 2000). The albitisation process was then followed by prograde regional metamorphism within the lower amphibolite facies (Petzel, 2010). The albitisation at Otjikoto is similar to the alteration within the lithology at the Placer Dome's Osborne mine, in Australia (Steven, 2001).

When new albite is formed, a significant mineralogical change takes place in addition to the replacement of feldspar by albite. The metasomatism process consisted of evaporates and salts in a closed groundwater basin which formed sodium rich brines (Scheepers, 2000). The Na-rich brines then reacted with silicate fragments to develop albite (Scheepers, 2000). Calcium

was released from plagioclase during digenesis and is present in the authigenic carbonates (Scheepers, 2000). The potassium released during metasomatism is incorporated with mica (Scheepers, 2000).

6.6 Conceptual Mineralisation Model for the Otjikoto Gold Deposit

In the Northern Zone of the Damara Orogeny, metapelites and carbonate rocks were deposited at ~700 Ma, to form the Swakop Group rocks (Miller, 2008). Deformation of the Swakop Group rocks took place at 620-580 Ma during the subduction of the Kalahari Craton beneath the Congo Craton (Miller, 2008). The subduction took place in a north-south direction and led to the formation of east-west striking folds (Lehmann et al., 2015).

The mineralised veins are believed to be of late Damaran age (Wanless et al., 2010). The amphiboles have undergone retrograde metamorphism within the greenschist facies and are replaced by biotite and chlorite. Temperatures of 534°C and 555°C have been obtained from quartz veins during oxygen isotope thermometry.

The Karibib Formation, which forms the hanging wall at Otjikoto, hosts pyrrhotite, pyrite and dolomite containing veins which appear to have formed from metamorphic fluid segregations (Scheepers, 2000). Metamorphic fluids were formed at lower crustal levels by the breakdown of minerals in carbonates and pelites during metamorphism. Stable oxygen isotope data from Curtis (2006) indicate that the mineralizing fluids from Otjikoto are derived from metamorphic fluids and not from magmatic fluids. The mineralising fluid migration and subsequent trapping was facilitated by the brittle-ductile deformation during the late Damaran D3-D4 deformation events (Wilton et al., 2002). This means that the gold remained in the solution as a result of the high chloride content in the mineralizing fluid (Petzel, 2010).

There is limited information in the literature that explains the transport mechanism of the mineralizing fluids from the lower crustal levels to the ore deposition site. It is suggested that the large scale structures were responsible for transporting the mineralizing fluid and regional scale structures were important for forming localised fluid traps at Otjikoto (Wanless et al., 2010). The faults in the area are interpreted to be related to the D2 deformational event of the Damara Orogeny. There is field evidence of steep faults and fractures that may have acted as a passage for the mineralizing fluids to move from deep levels within the crust (Petzel, 2010). The strike-slip faults have been identified from photo-geology and are also related to the D2 event (Lytle et al., 2013). Tomkinson (1999) noted the presence of an N-S trending right lateral fault zone which is believed to be responsible for localizing the gold mineralization. The

marbles and the mineralised albitites are part of an oblique thrust ramp system (Fletcher et al., 2013). These thrust systems are believed to have acted as fluid channels (Petzel, 2010). Thrusting took place during the D1 deformation event.

At Otjikoto, the hydrothermal fluid flow was enhanced by the presence of minor faults and joints. This fluid flow formed from iron-rich hydrothermal alteration which is closely associated with the gold mineralisation (Knupp, 2012). Petzel (2010) suggested that there are two fluid flow zones at Otjikoto, the high fluid flow zone and the low fluid flow zone. The high fluid flow zone is characterised by potassic alteration and calcite replacement of schist in the presence of thrusts. The low fluid flow zone is characterised by retrograde metamorphism.

Dextral shear systems, which intersected host rocks, are described as regional structures that facilitated the development of the sheeted vein system (Steven, 2001 and Fletcher et al., 2013). As the mineralizing fluids reacted with albitites and the karibib marbles, a change in the oxygen fugacity and the pH may have taken place. This could have also acted as a control for the gold mineralization. The dextral shears, which act as localised fluid traps, are required to allow the gold to accumulate and precipitate in economically justifiable amounts. Some of the rock units, such as the albitites, are more likely to be mineralised. Wanless et al (2010) explained that the preferential mineralisation of the albitites may be a result of their proximity to the carbonate units which may have played a geochemical role in facilitating the gold precipitation. Various authors (i.e. Scheepers, 2000 and Wanless et al., 2010) believe that the gold precipitation at Otjikoto was facilitated by oxidation-reduction (redox) processes and changing pH/Eh conditions within the vicinity of the marble unit. This is supported by the presence of CH_4 within the fluid inclusions. The gold precipitated as free gold and was depleted in sulphur (Tomkinson, 1999). A general observation is that the amount of gold precipitation is related to the presence of albite and carbonate minerals in the host rocks (Petzel, 2010). A conceptual mineralisation model is shown in Figure 6-4. The gold at Otjikoto commonly precipitates together with pyrite, pyrrhotite, magnetite and chalcopyrite (Wilton et al., 2002). Field observations have shown that visible gold is uncommon at Otjikoto. Pyrrhotite and magnetite are used as indicator minerals to decipher the presence of gold.

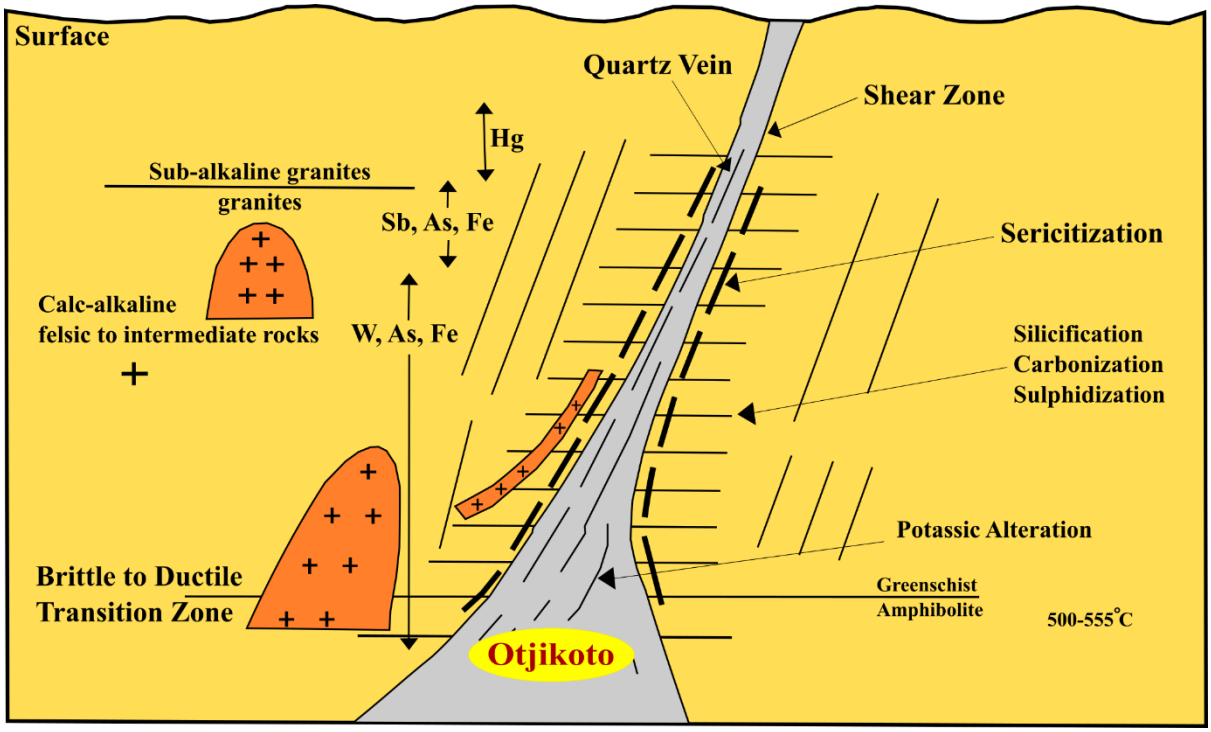

Figure 6-4 A schematic sketch which shows the suggested mineralisation model for the Otjikoto deposit. Metamorphic fluids were generated at lower crustal depths (6-29 km) of the Damara Orogen. These fluids may have formed as a result of albitisation in the metapelites during retrograde metamorphism at the lower greenschist to mid-amphibolite facies. Large scale structures (i.e folds) were responsible for transporting the fluids whereas regional structures (i.e thrust belts) were responsible for forming fluid traps. The diagram is modified after *(Groves et al., 1998)*.

6.7 Comparison to the Navachab Gold Deposit

The Navachab gold deposit is located within the Southern Central Zone of the Damara Orogeny. The Navachab gold mine is an open pit mine with current resources of 3.91 million ounces and ore reserves of 1.93 million ounces (Nthite, 2014). The mine produced an average of 80,000 ounces per annum during its lifetime (Nthite, 2014). The mine is located 11 km to the southwest of Karibib in Central Namibia. The Navachab gold mine is located 274 km from the Otjikoto Gold Mine.

Until recently, Navachab was the only operating gold mine within the Damara Orogeny. The deposit is hosted by a sequence of calc-silicates, marbles and biotite schists (Wulff, 2008). The rock types found at Navachab are from the Oberwasser, Okawayo and Spes Bona Formations (Dziggel et al., 2009). The highest grade of gold mineralization is hosted in banded calc-silicate rocks which are found at the base of the Okawayo Formation (Dziggel et al., 2009). The metasedimentary units at Navachab are intruded by pegmatites, aplite dikes and are cross-cut by auriferous veins, which is evidence of concordant and discordant contact relationships (Dziggel et al., 2009). The interpretation of these lithological relationships is that the magmatic activity took place concurrently with mineralization during ore deposition.

Two different styles of mineralization have been reported at Navachab (Kisters, 2005 and Dziggel et al, 2009). The first style of mineralization, which also exhibits the highest gold grade, is related to bedding parallel massive sulphide lenses (Dziggel et al., 2009). These sulphide lenses are found within the calc-silicate rocks and plunge at shallow angles towards the northeast (Dziggel et al., 2009). The sulphide lenses have an elongated cylindrical shape of 5 m high and up to 1.5 m wide ore bodies (Kisters, 2005). Drilling shows that the lenses can be traced for 1800 m in a down plunge direction (Dziggel et al., 2009). The second type of mineralisation style at Navachab is related to quartz hosted sulphide veins which cross-cut through all the rock types (Kisters, 2005). The quartz veins have a lateral extent of 3km x 1 km and continue throughout the entire width of the NW limb of the Karibib Dome (Dziggel et al., 2009). In both types of mineralisation style at Navachab, gold mainly occurs as native gold. Other ore minerals are sphalerite, arsenopyrite and chalcopyrite (Dziggel et al., 2009). Alteration halos are found between the contact of the wall rock and mineralised zones. These halos are made up of almandine garnet, clinopyroxene, biotite, k-feldspar and quartz (Dziggel et al., 2009). Pressure and temperature conditions of 2-2.5 kbar and 580 °c respectively, have been reported from geobarometry and thermometry studies of the sphalerite and arsenopyrite (Nörtemann et al., 2000). Granulite facies conditions are analogous to the Navachab gold deposit (Wulff, 2008).

The Navachab Deposit has been interpreted by Nörtemann et al (2000) and Creus (2011) as a reduced skarn deposit which formed in three development stages. The first developmental stage is related to metamorphism at constant chemical composition (isochemical) and dehydration of the banded marble. The second developmental stage led to more dehydration and decarbonization of the banded marble to form a garnet to pyroxene skarn (Creus, 2011). The third development stage led to retrograde metamorphism, alteration, fracturing and ore precipitation. Mineralisation developed as the sulphur fugacity increased and temperature decreased (Nörtemann et al., 2000).

The first notable similarity between Otjikoto and Navachab is that both gold deposits are hosted by rocks at the same stratigraphic level, namely the Okawayo and Oberwasser members. The Oberwasser rocks at Navachab consist of biotite schists and calc-silicates which have been observed at Otjikoto. The Okawayo member rocks are made up of dolomitic marbles, which are present at both Navchab and Otjikoto. However, the gold mineralisation at Otjikoto is not hosted by marble units whereas gold-bearing veins are present in marble units at Navachab. Another similarity is that in both deposits, mineralisation occurs in sheeted veins which are

continuous in strike. The thickness of these individual veins is also similar in both deposits, 1 cm to 10 cm.

At Navachab, the mineralising fluids were made up of a H_2O-CO_2-NaCl-$CaCl_2$ mixture (Wulff, 2008). At Otjikoto, the mineralising fluids are made up of a mixture of H_2O-CO_2-CH_4-NaCl. The mineralising fluids at Navachab have a low to moderate salinity (4-16 wt. % NaCl/$CaCl_2$) (Wulff, 2008). The mineralising fluids at Otjikoto have a moderate to high salinity (0.9-44.5 wt. % NaCl eq.).

The major difference between the Navachab and Otjikoto gold deposits are the ore minerals. The ore minerals at Navachab are sphalerite, bismuth, bismutinite, pyrrhotite, arsenopyrite, chalcopyrite and free gold. At Otjikoto, the ore minerals present are magnetite, chalcopyrite, pyrrhotite, pyrite and free gold. There is no sphalerite and bismuth mineralisation at Otjikoto. The quartz veins at Navachab are more continuous, compared to Otjikoto. Compared to Otjikoto, there is no evidence of albitisation at Navachab as opposed to Otjikoto. The dominant type of alteration at Navachab is silicification whereas at Otkikoto its albitisation.

At Navachab, conventional geothermometric methods suggested that the maximum ore formation conditions are at 500-550 °C at a pressure of 2000 bars (Wulff, 2008). The ore formation temperatures at Navachab are fairly comparable to oxygen isotope thermometric temperatures obtained from the Otjikoto samples (534 and 555°C).

The Navachab deposit occurs within the Southern Central Zone (sCZ) whereas the Otjikoto deposit occurs within the Northern Zone of the Damara Orogen. Both deposits are Neoproterozoic in age, having formed between 640 to 680 Ma (Petzel, 2010). Although both deposits were formed within the same timeframe, the deposition mechanism may have been slightly different.

7 Conclusions

1. Thin section petrography observations indicate that some of the chlorite grains appear to have underwent retrograde metamorphism under decreasing temperature conditions. The retrograde metamorphism took place under greenschist facies conditions.
2. During thin section petrography, euhedral almandine grains were observed and occur as porphyroblasts surrounded by a quartz and an albite rich matrix. The almandine grains are relatively large and show an intergrowth that is indicative of syn-tectonic metamorphic growth.
3. Analysis of the microprobe data on the amphiboles shows that the analysed grains are made up of anthophyllites. The anthophyllites form from the breakdown of magnesium rich rocks and as a retrograde product in schists. Microprobe data of the chlorites was also analysed and showed that the majority of the chlorites are made up of ripidolites. The other types of chlorites identified were pycnochlorites and diabantites.
4. Harker diagrams of major elements vs silica were plotted by using the major element data. All the samples analysed show a strong negative correlation of TiO_2, Al_2O_3, MgO, CaO, Na_2O, K_2O and FeOt vs SiO_2.
5. The microprobe data was used to calculate the temperatures of chlorite formation by using the equation by Kranidiotis and MacLean (1987). This equation is a revision of the chlorite geothermometry equation by Cathelineau (1988) that takes in account an "Al-saturated environment" as well as the X_{Fe} that is directly related to the composition of the whole rock. The temperatures calculated were in the range of 221°C to 358 °C.
6. The fluid inclusions from Otjikoto are divided into 3 types, based on their microthermometric properties. The fluid inclusion types are aqueous (NaCl equivalent), aqueous-carbonic, and carbonic (CO_2-CH_4) inclusions. The carbonic inclusions are the most abundant. The presence of CO_2 and CH_4 may be justified by the decomposition of the carbonaceous metasediments which are found in the stratigraphy at Otjikoto.
7. The fluid inclusions from Otjikoto show a large density variation ranging from 0.73 to 1.23 g/cm^3 in the aqueous inclusions and from 0.81 to 1.03 g/cm^3 in the carbonic inclusions.
8. It is suggested that the aqueous and carbonic inclusions from the Okonguarri Formation are the end members of fluid immiscibility. The homogenisation temperature of CO_2 (Th CO_2) values of the aqueous-carbonic and carbonic inclusions have similar ranges. The Th CO_2 values ranged from -55.1 to -9 in the carbonic inclusions and from -40.8 to -10.7 in the aqueous-carbonic inclusions which implies that the two fluid inclusion

types have a similar age range. In addition, the primary aqueous and carbonic inclusions do co-exist with the aqueous-carbonic inclusions in clusters.

9. The $\delta^{18}O$ values were obtained for quartz and magnetite samples from the mineralised veins. The values range from of 8.35 ‰ to 8.75 ‰ for the magnetite and 17.51 ‰ to 18.47 ‰ for the quartz samples.
10. Oxygen isotope thermometry was used to calculate the fractionation temperatures for the vein quartz and magnetite. The temperatures obtained were 555°C and 534°C.
11. The microthermometric data for the aqueous inclusions were used to calculate the salinity of the inclusions. The salinities ranged from 30.0 to 44.5 wt. % NaCl eq. in aqueous inclusions with halite crystals and from 0.9 to 22.9 wt. % NaCl eq. in inclusions without halite crystals. The moderate to high salinity of the aqueous inclusions are also supported by the presence of daughter crystals at room temperature.

8 References

Alkmim, F. et al., 2006. Kinematic evolution of the Araçuaí-West Congo orogen in Brazil and Africa: Nutcracker tectonics during the Neoproterozoic assembly of Gondwana. *Precambrian Research*, 149, pp.42 – 63.

Amiri, M. et al., 2016. Geothermobarometry of amphiboles in intermediate to basic rocks from the Almogholagh pluton in western Iran. *Journal of Mineralogical and Petrological Sciences*, 111, pp.337-50.

Ashworth, L., 2014. Mineralised Pegmatites of the Damara Belt, Namibia: Fluid inclusion and geochemical characteristics with implications for post collisional mineralisation. Phd Thesis. Johannesburg: University of Witswatersrand. pp.210-219.

Badenhorst, F. & Drews, U., 1993. The Navachab Gold Mine in central Namibia. Windhoek: Abstracts CMIN 93: Conference on Mining Investment in Namibia. pp.33-34.

Bakker, R., 2003. Package FLUIDS1. Computer programs for analysis of fluid inclusion data and for modelling bulk fluid properties. *Chemical Geology*, pp.5-11.

Bamba, O. et al., 1996. Nouveau type de gisement aurifere dans les ceintures de roches vertes birimiennes du Burkina Faso: les albitites de Larafella. *Ouagadougou*, Burkina Faso: Departement de Geologic, Universite de Ouagadougou. pp.2-10.

Blumenthal, V., 2010. A Geochemical Study of the Mineralization at the Hopper Property, Yukon: A Case Study of an Atypical Copper Occurrence. MSc. thesis. Waterloo, Ontario: University of Waterloo. pp. 20-88.

Bodart, E., 1966. On The Paragenesis of Albitites. Frankfurt, Germany: Institut fiir Petrologie, Geochemie und Lagerstättenkunde. pp.2-8.

Bodnar, R., 1993. Revised equation and table for determining the freezing point depression of H_2O-NaCl solutions. *Geochimica et Cosmochimica Acta*, 57, pp.683-84.

Bodnar, R. & Vityk, M., 1994. Interpretation of microthermometric data for H_2O-NaCl fluid inclusions. *Fluid Inclusions in Minerals: Methods and Applications. Short Course IMA*, pp.117-30.

Bottinga, Y. & Javoy, M., 1973. Comments on oxygen isotope geothermometry. *Earth Planet*, 20, pp.250-56.

Burrus, R., 1981. Analysis of phase equilibrium in C-O-H-S fluid inclusions. *Mineralogical Association of Canada Short Course Handbook*. pp.40-73.

Cathelineau, M., 1988. Cation Site Occupancy in Chlorites and Illites as a Function of Temperature. *Clay Minerals*, 23, pp.471-85.

Chetty, D., 1998. Geochemical Fingerprinting of Carbonate Wall Rock Alteration at Major Base Metal Sulphide Deposits in the Otavi Mountain Land, Namibia. MSc. (Geology) Thesis. University of Cape Town. pp.23-90.

Creus, P., 2011. Geology and structural controls of lode-gold mineralization around the Navachab Gold Mine in the Pan-African Damara Belt of Namibia. MSc Thesis. University of Stellenbosch. pp.5-40.

Curtis, C., 2006. Stable Isotope evidence for the origin of the Otjikoto Gold Deposit. Honours Thesis. Cape Town: University of Cape Town. pp.2-37.

Dladla, Y., 2015. Namibia Productivity Baseline Statistics Report. Windhoek: Productivity Namibia Ministry of Labour, Industrial Relations and Employment Creation. pp.11-12.

De Caritat, P., Hutcheon, I. & Walshe, J., 1993. Chlorite Geochemometry: A review. *Clay and clay minerals*, 2, pp.219-39.

De Kock, G., 2001. A reappraisal of the NamibianDamara stratigraphy in part of the Southern Swakop Terrane and its implications to basin evolution. *South African Journal of Geology*, (104), pp.116-35.

Duncan, A., Erlank, J. & Betton, P., 1984. Analytical Techniques and database descriptions. *Special Publication Geological Society of South Africa*. pp.3-17.

Dziggel, A., Wulff, K., Kolb, J. & Meyer, F., 2009. Processes of high-T fluid-rock interaction during gold mineralization in carbonate-bearing metasediments: the Navachab gold deposit, Namibia. *Springer-Verlag*. pp.3-6.

Edwards, A., 1965. Textures of the Ore Minerals. Melbourne: The Australian Institute of Mining and Metallurgy. pp.13-160.

Finkelstein, J., 2010. The Petrogenesis of the Mesozoic Maningoza suite Igneous complexes, Central West Madagascar. MSc. Thesis. Cape Town: University of Cape Town. pp.20-100.

Fletcher, B.A., Mackinnon, H.F. & Lombard, A.P.J., 2013. Otjikoto gold deposit: Discovery and exploration of Namibia's second major gold mine. Geological Report. Windhoek: B2Gold Corp. pp.2-6.

Foster, D. & Goscombe, B., 2013. Continental Growth and Recycling in Convergent Orogens with Large Turbidite Fans on Oceanic Crust. *Geosciences*, 3(3), pp.355-87.

Frei, D. & Gerdes, A., 2009. Precise and accurate in situ U–Pb dating of zircon with high sample throughput by automated LA-SF-ICP-MS. *Chemical Geology*, 3, pp.261-70.

Frimmel, H., Basei, M. & Gaucher, C., 2011. Neoproterozoic geodynamic evolution of SW-Gondwana: a southern African perspective. *International Journal of Earth Sciences*, (100), pp.321-51.

Goldfarb, R., Groves, D. & Gardoll, S., 2000. Tectonic setting and temporal evolution of orogenic gold deposits. *31st Int. Geol. Congress, Aug. 2000,* Rio de Janeiro, Brazil, vol. de presentaciones, CD-ROM, doc. pp.4

Goldstein, R. & Reynolds, J., 1994. Systematics of Fluid Inclusions in Diagenetic Minerals. Tulsa: Society for Sedimentary Geology. pp.2-6.

Gray, D. et al., 2008. A Damara Orogen perspective on the assembly of southwestern Gondwana. *Geological Society of London Special Publication*, 294, pp.256-77.

Groves, D. et al., 1998. Orogenic gold deposits: A proposed classification in the context of their crustal distribution and relationship to other gold deposit types. *Ore Geol. Rev*. Special Issue, 13, 7-27.

Gubelin, E. & John, K., 1986. Photoatlas of inclusions in Gemstones. Zurich: ABC Edition. pp.501-535.

Harris, C. & Vogeli, J., 2010. Oxygen isotope composition of garnet in the Peninsula Granite, Cape Granite Suite, South Africa: constraints on melting and emplacement mechanisms. *South African Journal of Geology*, 113(4), pp.402-12.

Hawthorne, F. et al., 2012. Nomenclature of the amphibole supergroup. *American Mineralogist*, 97, pp.2033-40.

Hey, M., 1954. A new review of the chlorites. *Mineralogical Magazine*, 30, pp.279-90.

Hodgson, C.J., 1989. The structure of shear-related, vein-type gold deposits: a review. *Ore Geology Review*., 4, 231-273.

Hoefs, J., 1997. Stable Isotope Geochemistry. 4th ed. *Springer Berlin Heidelberg*. pp.402-412.

Hoffmann, K., 1987. Application of tectonostratigraphic terrane analysis in the Damara Province of central and northern Namibia. *Bulletin of the Precambrian research Unit*, pp.24-27.

Hoffmann, K., Condon, D., Bowring, S. & Crowley, J., 2004. U-Pb zircon date from the Neoproterozoic Ghaub Formation, Namibia: Constraints on Maronian glaciation. *Geology*, (32), pp.816-20.

Hoffmann, K. & Prave, R., 1996. A preliminary note on a revised subdivision and regional correlation of the Otavi Group based on glaciogenic diamictites and associated cap dolostones. *Communications of the Geological Society of Namibia*, (11), pp.77-82.

Holloway, J., 1977. Fugacity and activity of molecular species in supercritical fluids. *Thermodynamics in Geology*, pp.161 – 182.

Inoue, A., Kurokawa, K. & Hatta, T., 2010. Application of Chlorite Geothermometry to Hydrothermal Alteration in Toyoha Geothermal System, Southwestern Hokkaido, Japan. *Resource Geology*, 60, pp.52-70.

Javoy, M., 1977. Stable Isotopes and Geothermometry. *Journal of the Geological Society*, 133, pp.610-35.

Johnson, S. & MacLean, I., 2016. News Release: B2Gold Reports Third Quarter 2015 Results. [Online] Available at: HYPERLINK "http://www.b2gold.com/news/display/index.php?news=2002314" http://www.b2gold.com/news/display/index.php?news=2002314 [Accessed 17 April 2016].

Kaszuba, J. et al., 2006. Immiscible CO2-H2 fluids in the shallow crust. Published by AGU and the Geochemical Society. pp.2-10.

Killick, A.M., 2000. The Matchless Belt and associated sulphide mineral deposits, Damara Orogen, Namibia. Windhoek: Geological Survey of Namibia. pp.73-80.

Kisters, A., 2005. Controls of gold-quartz vein formation during regional folding in amphibolites-facies, marble-dominated metasediments of the Navachab Gold Mine in the Pan-African damara Belt, Namibia. *South African Journal of Geology*, 108, 283-303.

Kisters, A., 2008. Introduction to the Damara Orogen. In *Isotope Geology of Namibia*. Windhoek: Geological Survey of Namibia. pp.7-15.

Klein, J., 1980. The geology of area 2115A. Geological Survey of Namibia. pp.31-40.

Klein, E. & Fuzikawa, K., 2010. Origin of the CO2-only fluid inclusions in the Palaeoproterozoic Carará vein-quartz gold deposit, Ipitinga Auriferous District, SE-Guiana Shield, Brazil: Implications for orogenic gold mineralisation. *Ore Geology Reviews*, (37), pp.31-40.

Knupp, K., 2012. Interpretation of High Resolution Helicopter Airborne Magnetic and Radiometric Data. Geophysics Report. Earthmaps Consulting. pp.2-20.

Kranidiotis, P. & MacLean, W., 1987. Systematics of chlorite alteration at the Phelps Dodge massive sulphide deposit, Matagami, Quebec. *Economic Geology*, 82, pp.1898-911.

Leake, B. et al., 2003. Nomenclature of amphiboles: additions and and revisions to the International Mineralogical Association's amphibole nomenclature. *Canadian Mineralogist*, 41, pp.1357-68.

Lehmann, J. et al., 2015. Structural and geochronological constraints on the Pan-African tectonic evolution of the northern Damara Belt, Namibia. *Tectonics*. pp.101-134.

Longridge, L., 2012. Tectonothermal Evolution of the southwestern Central Zone, Damara Belt, Namibia. Unpublished Ph.D. thesis. Johannesburg: University of Witswatersrand. pp.30-180.

Lytle, B. et al., 2013. Otjikoto Gold Project Feasibility Study. NI 43-101 TECHNICAL REPORT. B2 Gold Namibia (Pty) Ltd. pp.15-69.

McCuaig, T.C. & Kerrich, R., 1998. P-T-t-deformation-fluid characteristics of lode gold deposits: evidence from alteration systematics. *Ore Geology Reviews* 12(6), pp.381-453.

McDonald, A. et al., 2011. Otjikoto Gold Project, North-Central Namibia. NI 43-101 Technical Report. B2Gold Corp. pp.10-70.

McDonough, W. & Sun, S., 1995. The composition of the Earth. *Chemical geology*, pp.225-50.

Miller, R., 1983. Evolution of the Damara Orogen of South West Africa/Namibia. 11th ed. *Geological Society of South Africa Special Publication*. pp.225-250.

Miller, R., 2008. The Geology of Namibia. 3rd ed. Windhoek: Ministry of Mines and Energy of Namibia, Geological Survey. pp.113-180.

Naden, J. & Shepherd, T., 1989. Role of methane and carbon dioxide in gold deposition. *Nature*, 342, pp.793-95.

Nörtemann, M., Mucke, A., Weber, K. & Meinert, L., 2000. Mineralogy of the Navachab skarn deposit, Namibia: an unusual Au-bearing skarn in high-grade metamorphic rocks. *Communications of the Geological Survey of Namibia*, 149-156.

Nthite, C., 2014. Anglogold Ashanti completes sale of Navachab mine. [Online] Available at: HYPERLINK "http://www.anglogoldashanti.com/en/Media/news/Pages/Anglogold-Ashanti-Completes-Sale-of-Navacheb-Mine.aspx" http://www.anglogoldashanti.com/en/Media/news/Pages/Anglogold-Ashanti-Completes-Sale-of-Navacheb-Mine.aspx [Accessed 24 February 2017].

Palomba, M., 2001. Geological, mineralogical, geochemical features and genesis of the albitite deposits of Central Sardinia (Italy). Cagliari, Italy: Rendiconti Seminario Facoltà Scienze Università Cagliari Supplemento Vol. 71 Fasc. 2. pp.1-5.

Passchier, C. & Trouw, R., 1996. Microtectonics. Berlin: *Springer-Verlag Berlin Heidelberg*. pp.163-180.

Petzel, V., 2010. The Geology of the Otjikoto Deposit and Surroundings. Auryx Gold. pp.3-41.

Ramboz, C., Pichavant, M. & Weisbrod, A., 1982. Fluid immiscibility in natural processes: Use and misuse of of fluid inclusion data in terms of immiscibility. *Chemical Geology*, (37), pp.30-45.

Rankin, W., 2015. Cross-Border correlation of the Damara Belt in Namibia and equivalent lithologies in Northwestern Botswana from potential field and magnetotelluric interpretations. MSc thesis. Johannesburg: university of Witswatersrand. pp.5-60.

Robert, F., 1996. Quartz-carbonate vein gold. *Geol. Surv. Can*., Geology of Canada, no. 8, pp.350-366.

Roedder, E., 1972. Composition of fluid inclusions. *US Geological Survey Professional Paper*, 440JJ, pp.163-64.

Scheepers, R., 2000. Report on the geology of boreholes OT1 and OT3. Avdale Internal Report. Windhoek: University of Stellenbosch. pp.3-70.

Shepherd, T.J., Rankin, A.H. & Alderton, D.H., 1985. A pratical guide to fluid inclusion studies. Blackie. Glasgow. pp.234-236.

Sibson, R.H. & Scott, J., 1998. Stress/fault controls on the containment and release of overpressured fluids: Examples from the gold-quartz vein systems in Juneau, Alaska; Victoria, Australia and Otago, New Zealand. *Ore Geol. Rev. Special Issue*, 13, 293-306.

Steven, N., 2001. Report on the Otjikoto Project, northeastern Namibia. Windhoek: Rockwater Consulting. pp.110-132.

Thiéry, R., Vidal, J. & Dubessy, J., 1994. Phase equilibria modelling applied to fluid inclusions: liquid–vapour equilibria and calculation of the molar volume in the CO2–CH4–N2 system. *Geochim*, 58, pp.1074-82.

Tomkinson, M., 1999. Observations on exploration projects in Namibia. Memorandum. Epi genesis Consulting Pty. Ltd. pp.3-50.

Van der Merwe, A.J. & Jones, C., 2005. Otavi Exploration Project, Namibia. Technical Report. RSG Global Consulting Pty (Ltd). pp.7-60.

Van Der Merwe, J. & Wanless, M., 2007. Otjikoto Gold Project, Otavi Region, Republic of Namibia. Independent Technical Report. SRK Consulting. pp.8-43.

Waldeck, H. & Terbrugge, P., 2008. Otjikoto Gold Project: Definitive Feasibility Level Mining Geotechnics Study. Johannesburg: SRK Consulting Engineers and Scientists AVDALE Namibia (Pty) Ltd. pp.30-120.

Wanless, M. & Crisp, S., 2009. Otjikoto Gold Project, Otavi Exploration Area, Republic of Namibia. Independent Technical Report. SRK Consulting. pp.10-53.

Wanless, M., Crisp, S. & Simposya, V., 2010. Mineral Resource Estimate - Otjikoto Gold Project. Independent Technical Report. Johannesburg: Auryx Gold Corporation SRK Consulting Engineers and Scientists. pp.5-55.

Weiss, F., 2013. Oxygen and Iron Isotope Systematics of the Grängesberg Mining District (GMD), Central Sweden. Göteborg: Tryckt hos Institutionen för geovetenskaper. pp.21-56.

Wilton, J., Lombard, P.J.A. & Philpot, H.G., 2002. Discovery of the Otjikoto gold deposit. Windhoek: Proceedings of the 11th Quadrennial IAGOD Symposium and Geocongress 2002 Anglovaal Namibia (Pty) Ltd. pp.2-5.

Wulff, K., 2008. Petrography, geochemistry and stable isotope characteristics of the Navachab gold deposit, Namibia. PhD Thesis. University of Aachen. pp.6-120.

Yao, Y., Murphy, P. & Robb, L., 2001. Fluid Characteristics of Granitoid-Hosted Gold Deposits in the Birimian Terrane of Ghana: A Fluid Inclusion Microthermometric and Raman Spectroscopic study. *Economic Geology*, (96), pp.1612-42.

Yardley, D., MacKenzie, S. & Guilford, C., 1990. Atlas of Metamorphic rocks and their textures. *Harlow: Longman Scientific & Technical*. pp.10-82.

9 Appendix A

Table 10 Summary table of the samples collected from the Otjikoto Gold Mine.

Sample ID	Block Number	X	Y	Z	Plane Type	Dip	Dip Direction	Strike	Rock Type
OT311	455_31_	720271	7789132	1469	Bedding	26	125	035	Biotite Schist
OT312	455_31	720274	7789133	1466	Bedding	23	132	042	Amphibole Hornfels
OT315	455_31	720275	7789128	1467	Bedding	40	142	052	Albitite
OTC323	455_33_C	720230	7789043	1459	Bedding	63	177	087	Amphibole Hornfels
OTB321	455_32_B	720284	7789126	1467	Bedding	28	128	038	Amphibole Hornfels
OT333	455_33	720267	7789039	1453	Bedding	54	174	084	Garnet Amphibole Hornfels
OTU322	455_32	720293	7789049	1455	Bedding	22	180	090	Albite Biotite Schist
OTC201	455_20_C	720348	7789036	1457	Bedding	72	164	074	Albitite
OTC204	455_20_C	720350	7789038	1457	Vein	70	150	060	Amphibole Hornfels (mineralised)
OTC202	455_20_C	720354	7789035	1457	Bedding	40	139	049	Biotite Schist
OTC321	455_32_C	720245	7789115	1459	Bedding	46	134	044	Amphibole Hornfels
OT321	455_32_	720241	7789106	1458	Bedding	46	164	074	Amphibole Hornfels
OTC322	455_32_C	720241	7789106	1459	Bedding	29	152	062	Garnet Amphibole Hornfels
OTC323-2	455_32_C	720241	7789106	1459	Bedding	28	140	050	Garnet Biotite Schist
OTC324	455_32_C	720242	7789095	1478	Bedding	26	132	042	Garnet Biotite Schist
OT322-2	455_32	720406	7789057	1462	Bedding	11	258	168	Biotite Schist
OT321-2	455_32	720413	7789083	1458	Bedding	36	153	063	Biotite Schist
OTA231	455_23_A	720463	7789220	1463	Bedding	20	149	059	Albitite
OTA232	455_23_A	720403	7789132	1463	Bedding	20	153	063	Amphibole Hornfels
OTA233	455_23_A	720403	7789132	1463	Bedding	20	153	063	Amphibole Hornfels

OTA234	455_23_A	720407	7789128	1466	Bedding	23	160	070	Albitite
OTB231-2	455_23_B	720369	7789135	1452	Bedding	61	165	075	Albitite
OTB232-2	455_23_B	720369	7789135	1452	Bedding	61	165	075	Albitite
OTB233-2	455_23_B	720354	7789130	1464	Bedding	9	173	083	Albitite (adjacent to fault)
OTB234-2	455_23_B				Bedding	30	163	073	Amphibole Hornfels
OTB232	455_23_B	720361	7789110	1450	Bedding	30	127	037	Amphibole Hornfels
OTB231	455_23_B	720363	7789108	1451	Bedding	14	205	115	Amphibole Hornfels
OTB233	455_23_B	720353	7789104	1451	Bedding	30	230	140	Amphibole Hornfels
OTB234	455_23_B	720347	7789091	1459	Bedding	17	358	268	Quartz Vein
OT291	455_29_	720378	7789208	1462	Bedding	26	175	085	Albitite
OT292	455_29	720376	7789206	1458	Bedding	54	240	150	Amphibole Hornfels
OT294	455_29	720378	7789196	1459	Bedding	34	160	070	Garnet Biotite Schist
OT293	455_29				Bedding				Biotite Schist
OTC231	455_23_C	720400	7789152	1461	Bedding				
OTC232	455_23_C	720399	7789150	1468	Bedding	86	6	276	Albitite
OTC233	455_23_C	720402	7789142	1496	Vein	66	327	237	Amphibole Hornfels (mineralized)
OTC234	455_23_C	720400	7789143	1473	Bedding	41	176	086	Amphibole Hornfels
OTC239	455_23_C	720401	7789142	1468	Vein				Quartz Vein
OT311-2	455_31_								Amphibole Hornfels
OT312-2	455_31								
OT313	455_31								
OT322-3	455_32					35	135	45	
OT323	455_32					24			
OTB232-3	455_23_B				Bedding	48	123	033	Amphibole Hornfels
OTB234-3	455_23_B				Bedding	34	162	072	Amphibole Hornfels

OTB322	455_32_B					30	133	043	
OTB323	455_32_B					21	139	049	
OTB324	455_32_B					30	183	093	
OTB325	455_32_B								Biotite Schist
OTC203	455_20C				Vein				Vein
OTC236	455_23_C								
OTC237	455_23_C								
OTC331	455_33_C					66	176	086	
OTC332	455_33_C					62	185	095	
OTC333	455_33_C					20	122	032	

Table 11 Table summarising the visually estimated mineral composition of the rock samples from Otjikoto

Sample Numbers	Rock Type	Minerals (%)								Sulphides (%)			Comments
		Albite	**Amphibole**	**Biotite**	**Muscovite**	**Dolomite**	**Garnet**	**Chlorite**	**Quartz**	**Pyrite**	**Magnetite**	**Pyrrhotite**	
OT-291	Albite Hornfels	60				15		10	10	5	5		Dendrites
OTB-322	Amphibole Hornfels	50	10	<1		5		5	20				
OT-321	Biotite Schist	50	10	20		5			5	<1	<1	<1	
OTC-323	Albite Biotite Schist	40	<1	40	<1	5	5		<1				
OTA-234	Albite Hornfels	60				15			10				Sieve Texture
OT-295	Albite Biotite Schist	40	<1	40	<1	5	5		<1				
OTA-232	Garnet Amphibole Hornfels	40	10	5		5	10		30	20	5	15	
OTC-322	Albite Biotite Schist	40	<1	40	<1	5	5		<1				
OT-233	Amphibole Hornfels	50	10			5		5	20				
OTB-231	Albite Hornfels	60				15		10	10				
OT-232	Amphibole Hornfels	50	10			5		5	20				

OT-294	Garnet Biotite Schist	50	5	20	<1	5	10		5	<1		<1	Retrograde Texture
OTU-231	Pyritic Quartz Vein	10	10	20		5		5	20	20		10	Retrograde Texture
OTA-231	Albitite	60				15		5	10				
OT-293	Amphibole Hornfels	50	10			5		5	20	10			Mineralised
OTC-238	Albite Hornfels	10	10			5	5	5	25	10	10	15	Pyrite-Magnetite Vein
OTC-239	Pyrite-Magnetite Vein	10	5			20			50	10	10		
OTU-322	Albite Biotite Schist	40				5		10	30	5	5		Quartz Vein
OTU-235	Pyrite-Magnetite Vein	10				10			10	30	30	10	
OTC-232	Albite Hornfels	35				20			5	10	10	10	Disseminated Vein
OTC-2310	Pyrite-Magnetite Vein	15				10				30	30	10	
OTA-238	Albite Hornfels	40				5		15	10	10	20		
OTC-233	Albite Hornfels	40				10				10	20	10	Disseminated Vein
OTC-236	Albite Hornfels	20				30			10	15	15	10	
OT-202	Albite Hornfels	40	10			5			5	15	20	5	
OTC-231	Amphibole Hornfels	30	10			10		5	5	15	10	10	
OUT-234	Pyrite-Magnetite Vein	5				10			10	30	40	5	

Table 12 Standards used in calibrating the electron microprobe

Element	Standard	Analysing Crystal	LLD	1σ
Si	K-H	TAP	0.055	0.2
Ti	Rut	PET	0.039	0.06
Al	K-H	TAP	0.044	0.11
Fe	K-H	LIF	0.077	0.19
Mn	Rhod	LIF	0.061	0.03
Mg	K-H	TAP	0.029	0.09
Ca	K-H	PET	0.027	0.1
Na	K-H	TAP	0.033	0.06
K	K-H	PET	0.019	0.02